Multiscale Modeling of Heat and Mass Transfer Phenomena in Nanofluids

Felipe Aristizábal

Doctoral Thesis

Department of Chemical Engineering

McGill University

Montréal,Québec

September 2014

Thesis submitted in partial fulfillment
of the requirements for the degree of
Doctor of Philosophy

DEDICATION

Para Catherine

ACKNOWLEDGEMENTS

I would like to express my most profound gratitude to Prof. Sylvain Coulombe, my supervisor, for his patience, guidance, enthusiastic encouragement and support during the course of this project. His confidence in me and great advice, personal and professional, have made of the time dedicated to this project an enriching experience for my professional career.

I would like to thank present and past members of the Plasma Processing Laboratory, namely Husam, Larissa, Leron, Jason, Jocelyn, Martin, Mark, Mathew and Nathan, for the enlightening discussions, camaraderie and moral support. The long lasting discussions and time in the lab with Jocelyn Veilleux shaped the research directions taken in this project.

The computational model developed in this project was possible thanks to Prof. Ulrich Rüde, chair for System Simulation at the Friedrich-Alexander-Universität Erlangen-Nürnberg (FAU). I would like to thank the entire System Simulation chair for helping me develop the computational skills required for making this project possible. I would like to thank Dr. Ing. Harald Köstler for helping with the implementation of the multi-grid solver, and Dr. Klaus Iglberger and Dominik Bartuschat for guiding me through the painful path of C++ programming. Finally and most importantly, I would like to convey my immense gratitude to Dr. Christian Feichtinger.

The long discussions and chat sessions over the last few years have made this project a reality.

This project was made possible thanks to the financial support from the Natural Science and Engineering Research Council of Canada (NSERC), the Fonds de recherche du Québec - Nature et technologies (FRQNT) and McGill University.

The access to high performance supercomputers provided by Compute Canada and participating consortia (Calcul Québec, ACEnet, HPCVL, SciNet, SHARCNET and WestGrid) is acknowledged.

ABSTRACT

Heat and mass transfer phenomena in nanofluids are studied using numerical experiments. The main focus of this study is to determine the contribution of nanoparticle Brownian motion-induced micro-convection currents on the effective thermal conductivity and effective mass diffusivity.

The mathematical model developed is based on the fluctuating lattice Boltzmann method (fLBM) to simulate nanoparticle Brownian motion, the multiple relaxation time lattice Boltzmann method (MRT-LBM) to provide a description of micro-convection currents, and the finite volume method (FVM) to calculate the evolution of a scalar field (mass or temperature) subject to the effect micro-convection currents. Finally, two averaging methods to calculate effective thermal conductivity and effective mass diffusion coefficient are presented and validated.

The results from numerical experiments on heat transfer show that nanoparticle Brownian motion-induced micro-convection currents are not significant enough to justify any notable enhancements in thermal conductivity above the values estimated using classical models for composite materials.

In the case of mass transfer, the numerical experiments show that nanoparticle Brownian motion-induced micro-convection currents cause significant enhancements of the effective mass diffusion coefficient. This result is in general agreement with the conclusion drawn by Veilleux and Coulombe (2010, J. Appl. Phys.) using scaling arguments based on the heat and mass transfer Péclet numbers, that Brownian motion has a much larger effect on the mass diffusivity than on the heat diffusivity.

The numerical experiments on mass transfer are summarized by a simplified model based on dispersion. The parameters considered in the numerical experiments are: particle size, particle density, fluid viscosity, fluid density and temperature. The simplified model adds two important terms to Maxwell's model: a new dimensionless number N_{BM} (defined as the ratio of the nanoparticles Brownian self-diffusion coefficient over the molecular diffusion coefficient) and a particle interaction term.

Although the simplified model fails to predict the order of magnitude increase in mass diffusivity for Rhodamine 6G in 10 nm $\mathrm{Al_2O_3}$-water nanofluids ($D_{\mathrm{eff}}/D_{\mathrm{m}} = 1.2$ compared to the experimental value of 10), the form of the simplified model is used to provide possible explanations for the effective mass diffusivity increase/decrease with nanoparticle volume fraction observed experimentally.

This thesis concludes by extending the current analysis to polydisperse nanoparticle suspensions. Numerical experiments on bidisperse suspensions highlight the importance of the interaction term in the simplified model.

ABRÉGÉ

Les phénomènes de transfert de chaleur et de masse dans les nanofluides sont étudiés à l'aide d'expérimentations numériques. L'intérêt principal de cette étude est de déterminer la contribution des courants de micro-convection induits par mouvement Brownien de nanoparticules sur la conductivité thermique et le coefficient de diffusion massique effectifs.

Le modèle mathématique développé est fondé sur la méthode de lattice Boltzmann fluctuante (fLBM) pour simuler le mouvement Brownien des nanoparticules, sur la méthode de lattice Boltzmann à temps de relaxation multiple (MRT-LBM) pour fournir une description des courants de micro-convection et sur la méthode de volume fini (FVM) pour calculer l'évolution d'un champ scalaire (masse ou température) sujet à l'effet des courants de micro-convection. Finalement, deux méthodes d'établissement de la moyenne pour calculer les coefficients de conductivité thermique et de diffusion massique effectifs sont présentés et validés.

Les résultats d'expérimentations numériques sur le transfert thermique démontrent que les courants de micro-convection induits par mouvement Brownien de nanoparticules ne sont pas suffisamment significatifs pour justifier l'amélioration de la conductivité thermique jusqu'à des valeurs dépassant celles obtenues avec les modèles classiques pour les matériaux composites.

Dans le cas du transfert de masse, les expérimentations numériques démontrent que les courants de micro-convection induits par mouvement Brownien de nanoparticules provoquent une amélioration du coefficient de diffusion massique effectif. Ce résultat concorde avec la conclusion obtenue par Veilleux et Coulombe (2010, J. Appl. Phys.) à partir d'analyse dimensionnelle basée sur le nombre de Péclet pour les transferts de masse et de chaleur ; le mouvement Brownien a un bien plus grand effet sur la diffusion massique que sur la conductivité thermique.

Les expérimentations numériques sur le transfert de masse sont synthétisées par un model simplifié basé sur la dispersion. Les paramètres considérés dans les expérimentations numériques sont : la taille des particules, la densité des particules, la viscosité du fluide, la densité du fluide et la température. Le modèle simplifié ajoute deux termes importants au modèle de Maxwell : un nouveau nombre sans dimension $\mathrm{N_{BM}}$ (défini comme étant le rapport du coefficient d'auto-diffusion Brownien des nanoparticules sur le coefficient de diffusion moléculaire) et le terme représentant l'interaction entre les particules.

Bien que le modèle simplifié échoue à prédire l'ordre de grandeur de l'augmentation du coefficient de diffusion massique pour la Rhodamine 6G dans un nanofluide comportant des nanoparticules de 10 nm de $\mathrm{Al_2O_3}$ en suspension dans l'eau ($D_{\mathrm{eff}}/D_{\mathrm{m}} = 1.2$, comparé à une valeur expérimentale de 10), il est utilisé pour fournir des explications possibles à l'augmentation et la baisse du coefficient de diffusion massique effectif par rapport à la fraction de particules.

Cette thèse se conclut avec l'approfondissement de l'analyse actuelle des suspensions polydispersées dans les nanofluides. Les expérimentations numériques portant sur des suspensions bidispersées soulignent l'importance du terme représentant l'interaction entre les particules dans le modèle simplifié.

Contents

List of Tables

List of Figures

Part I

Introduction

Chapter 1
Introduction

1.1 Background

Nanofluids are engineered colloidal suspensions composed of nanoparticles in a base fluid (Choi, 1995). The presence of nanoparticles in the base fluid imparts unique properties to these fluids, including enhanced energy, momentum and mass transfer rates, as well as reduced tendency for sedimentation and erosion of the containing surfaces (when compared to μm and mm size particles). These unique properties make nanofluids appealing new materials for applications such as heat management, solar power collection, drug delivery, cancer treatment, amongst others (Taylor et al., 2013). Despite the fact of being solid/liquid systems, traditional models for composites fail to explain the unique transport properties of nanofluids.

Regardless of the large efforts made during the last two decades, the common denominator in the study of nanofluids is the lack of phenomenological understanding of the atypical properties of these fluids. Several modeling approaches have been proposed with relative success at different scales. At the molecular scale, molecular dynamics has proven to accurately estimate interfacial resistance (nanoparticle-fluid interface). However, this approach is limited to very small scales and the interactions between nanoparticles are difficult to incorporate into this framework (Sarkar and

Selvam, 2007). At larger scales the fluid around the nanoparticles can be regarded as a continuum, and the standard equations for fluid mechanics can be applied. However, since these equations rely on transport coefficients, these studies are limited to order-of-magnitude estimates (Bhattacharya et al., 2004).

Nanoparticle Brownian motion-induced micro-convection currents have been proposed as a possible explanation for the enhancement of thermal conductivity and mass diffusion coefficient measured in nanofluids (Krishnamurthy et al., 2006; Michaelides, 2014). During the course of this thesis project a numerical model was developed to study the importance of particle Brownian motion on the effective thermal conductivity and mass diffusivity of nanofluids.

1.2 Objectives

The main objective of this thesis is to study the contribution of nanoparticles Brownian motion-induced micro-convection currents on the effective heat and mass diffusion coefficients in nanofluids. The following specific objective are addressed:

1. To develope and implement a mathematical model capable of describing the evolution of nanoparticle Brownian motion-induced micro-convection currents.
2. To develop an averaging procedure to estimate macroscopic or effective thermal conductivity and mass diffusivity from the scalar field solution at a microscopic scale.

3. To validate the proposed model by comparing the results with the known solutions for thermal conductivity and mass diffusivity for composite materials.
4. To study the effect of different parameters (temperature, nanoparticle size and density, fluid viscosity and fluid density) on the effective thermal conductivity and effective mass diffusivity for nanofluid systems.
5. To develop a simplified model to describe the relationship between the different parameters studied and the effective mass diffusivity of nanofluids.

1.3 Organization of the thesis

This thesis manuscript was divided in four parts: Introduction, Mathematical Model, Applications and Conclusion. Background information and the objectives of this thesis are stated in chapter 1. chapter 2 contains a brief review of the nanofluid literature with a focus on numerical studies performed on the subject of heat and mass transfer phenomena.

The second part of this manuscript covers the details of the numerical model developed. chapter 3 gives a general overview of the methodology chosen. The details of this methodology are discussed in the three subsequent chapters. chapter 4 describes the implementation of the fluctuating lattice Boltzmann method (fLBM) and the methods used for simulating particles under Brownian motion. The lattice Boltzmann method (LBM, without fluctuations) is then described. chapter 5 introduces the hybrid LBM-FVM used to calculate the time evolution of a scalar field.

The mathematical model description concludes in chapter 6, where the macroscopic averaging operators are introduced. These operators are used to transform the microscopic information obtained from the hybrid LBM-FVM into macroscopic effective transport coefficients, i.e. thermal conductivity or mass diffusion coefficient.

The third part starts with a validation of the numerical method proposed. This is done in chapter 7 where the heat transfer and mass transfer across composite materials are considered. In chapter 8 the model is applied to the study of heat transfer in nanofluids. The main application of the model proposed here is presented in chapter 9, where mass transfer in nanofluids is considered. In the same chapter a simplified mathematical model that summarizes the numerical results obtained is proposed. The chapter concludes with a preliminary study of bidisperse nanofluids.

The work presented in this manuscript is summarized in chapter 10, followed by original contribution and suggestions for future work.

Chapter 2
Literature Review

Colloidal suspensions of particles in the nanometer range are commonly known as "nanofluids". This name was introduced by Choi (1995) to refer specifically to suspensions of metallic nanoparticles in conventional heat transfer fluids (e.g. water, ethylene glycol). Over the years, the term "nanofluid" has been accepted by the scientific community (Das et al., 2006) to refer to a wider range of nanoparticle suspensions, including, not only metallic nanoparticles but also non-metallic particles, carbon nanotubes (CNT), etc. Thanks to their enhanced thermal conductivity at low particle concentrations, nanofluids have been the subject of intensive research during the last few years (Keblinski et al., 2005).

Although an innovative approach, the concept of using inclusions of metallic particles to modify bulk properties of materials has been used for over a century (Maxwell, 1892). However, technological limitations have restricted the analysis of these composite systems to inclusions down to the micrometer range. These types of particles sediment out of solution and cause high erosion rates in flowing systems, making them unattractive for practical applications.

The recent developments in nanotechnology have permitted the study of composite systems with inclusions in the nanometer range. At this scale, the increased importance of nanoparticle Brownian motion in the system reduces sedimentation rates; while erosion rates in flowing systems are reduced because of the smaller size of the inclusions and the lower particle load needed to achieve a significant increase in thermal conductivity (Heris et al., 2007).

The following sections briefly describe the most common methods of preparation of nanofluids, some of the experimental measurements reported in the literature, and the existing theoretical and numerical models developed to gain a better understanding of the unusual properties of nanofluids. The review presented below touches the subjects of nanofluid preparation and experimental measurements, however the main focus is numerical studies. For a through discussion on the subject of nanofluids see the recent work by Michaelides (2014).

2.1 Preparation of Nanofluids

Although nanofluids seam to be simple solid-liquid mixtures, the synthesis of these materials need to satisfy special requirements; for example stability. Despite the contribution of Brownian motion, nanoparticles suspensions may also agglomerate and sediment out of solution. Different factors such as agglomeration (Prasher et al., 2006a), pH, among others affect the stability of nanofluids. Proper preparation to ensure stability of the solid phase is a key element in any experimental study or in the production of nanofluids.

Nanofluids are commonly prepared by either single-step or two-step methods (Wang and Mujumdar, 2007). As its name indicates, single-step preparation methods only need one step to produce and suspend the particles in the base fluid. In this method the particles are normally produced by the contact of a hot vapor with the base fluid. Particles can also be produced by chemical reaction of selected reactants dissolved in the base fluid (Zhu et al., 2004). Two common single-steps methods are: a) VEROS (Vacuum Evaporation onto a Running Oil Substrate) (Akoh et al., 1978) and b) Vacuum-SANSS (Submerged Arc Nanoparticle Synthesis System) (Lo et al., 2005). The main advantage of single-step methods is that the particle agglomeration during synthesis is minimized, compared to other methods. However, one of the disadvantage is the restriction to low vapor pressure base fluids.

In two-step methods the nanoparticles are first produced and then dispersed into the based fluid. This method is extensively used because of the rather available commercial sources of nanopowders. However, the critical step in the preparation of nanofluids by two-step methods is the suspension of the nanoparticles. Typically, this is done by using ultrasound equipment, which not only helps to suspend the particles, but also to reduce agglomeration (Kwak and Kim, 2005). Other techniques include the use of surfactant agents (Mao et al., 2014) or particle coating (Coulombe and Tavares, 2007). The two-step method has been used for suspending different types of nanoparticles, including Al_2O_3, TiO_2, Au, Ag, CNTs, among others (Eastman et al., 1997; Wang et al., 1999; Chon et al., 2005; Lee et al., 2007)

More recently, Taylor et al. (2013) published a review on nanofluids. An entire section was dedicated to synthesis methods of nanofluids. This section includes synthesis of nanoparticles (physical and chemical methods), stabilization and direct nanofluid synthesis.

2.2 Experimental Measurements

2.2.1 Heat Transfer

Thermal conductivity is the nanofluid property most widely studied. The interest in this particular transport property arose from the early observations of thermal conductivity enhancement of nanofluids (Masuda et al., 1993) and their potential benefits to heat transfer applications. For example, pumping power in a heat exchanger necessary to satisfy heat transfer requirements could be reduced by increasing the thermal conductivity of the fluid using nanofluids (Choi, 1995).

The Transient Hot-Wire method (THW) (Healy et al., 1976; Haarman, 1971) is the experimental technique most extensively used for measuring the thermal conductivity in nanofluids. However, since nanofluids are in general electrically conductive materials a modified version of the THW method is often used (Nagasaka and Nagashima, 1981). Other techniques such as the steady-state parallel-plate (Wang et al., 1999), the temperature oscillation (Santucci and Verdini, 1986; Bhattacharya et al., 2006), and the optical beam-deflection technique (Rusconi et al., 2006) have also been employed to address some of the practical drawbacks related to THW measurements (e.g. convective effects, accumulation of conducting ions near the hot wire, among others).

The review by Wang and Mujumdar (2007) includes a concise summary of experimental measurements of thermal conductivity of nanofluids reported in the literature.

Although sometimes contradicting, in general this review shows the existence of experimental evidence that the thermal conductivity of nanofluids is higher than that of the base fluid. Few of these important results are discussed below.

In sum, the review from Wang and Mujumdar (2007) indicates that particle surface chemistry plays an important role in the thermal conductivity enhancement of nanofluids (Xie et al., 2002). Also, the thermal conductivity of the suspended particles does not necessarily have a direct relation with the effective enhancement of the nanofluid (Hong et al., 2005), as would have been expected from the relation proposed by Maxwell (1892). Furthermore, the dependence of the thermal conductivity enhancement on particle size (Jang and Choi, 2007) and temperature (Das et al., 2003b; Chon et al., 2005) indicates the possible influence of nanoparticle Brownian motion. Another important observation is the fact that certain nanofluids present significant enhancements at very low nanoparticle volume fractions (∼0.3%) (Eastman et al., 2001). Finally, the highest enhancement reported in the literature was achieved by suspending single wall carbon nanotubes in epoxy. A 300% enhancement was obtained with only 1% nanotube volume fraction (Choi et al., 2001).

Controversially, recent studies of commonly used nanofluid systems have reported no abnormal enhancement of the thermal conductivity (Rusconi et al., 2006; Venerus et al., 2006; Putnam et al., 2006; Zhang et al., 2007; Eapen et al., 2007) when compared with the thermal conductivity model for composite materials proposed by Hamilton and Crosser (1962). However, no clear explanation has been given for the discrepancy with the abnormal enhancement found in previous measurements.

Whether preparation, measurement, or interpretation of the results is the cause of these discrepancies, it is not known for the moment.

The potential improvement of nanofluid technology to heat transfer equipment has led to investigations of more realistic systems, where the principal mechanisms of heat transport are forced convection (Daungthongsuk and Wongwises, 2007), natural convection (Tzou, 2008) or pool boiling (Das et al., 2003a). Although, thermal conductivity plays an important role in these types of systems, other transport properties such as viscosity are also important. The real enhancement of heat transfer capability of nanofluids when used under convective condition is expected to be much higher than the enhancement on thermal conductivity alone, as observed for suspensions of micron-size particles (Ahuja, 1975, 1980; Sohn and Chen, 1981; Liu et al., 1988).

The work of Wang and Mujumdar (2007) also includes a good review on natural and convective heat transfer experiments using nanofluids. From the literature reviewed, the authors conclude that particle shape is a significant parameter that needs to be carefully examined to facilitate the proper understanding of the scattered experimental results. Furthermore, the heat transfer behavior of nanofluids is very complex and the influence of different parameters other than thermal conductivity alone should also be considered. Pool boiling was also covered in this review, leading to the conclusion that surface properties such as roughness, wettability and contamination should be considered in future studies.

Buongiorno et al. (2009) published the results from the International Nanofluid Property Benchmark Exercise (INPBE). Over 30 organizations worldwide contributed to this study using a variety of experimental approaches, including THW, steady-state methods, and optical methods. It was found that the thermal conductivity increases with particle concentration and aspect ratio. The increase observed can be described by the effective medium theory developed by Maxwell (1873) and recently generalized by Nan et al. (1997); all tests can be predicted with less than 17% error. No anomalous thermal conductivity enhancement was observed for the nanofluids tested in the INPBE. Therefore, Brownian motion, liquid layering and aggregation theories were not required to interpret the results from the INPBE.

Another interesting review paper was published by Ozerinc et al. (2010). This review is organized by the effect of different characteristics of the nanofluid in question: volume fraction, particle type, base fluid, particle size, particle shape, temperature, clustering and pH are discussed. The review concludes by indicating that significant discrepancies in the experimental data exist. Furthermore, from the experimental point of view, the average particle size is not sufficient to characterize a nanofluid, because non-linear relations exist between size and thermal transport. The authors also highlight the fact that additives, pH, and sonication techniques should be reported in the studies because these affect clustering and in turn, the effective particle size.

Branson et al. (2013) measured the thermal conductivity of nano-diamond based nanofluids using the short hot-wire probe method. The authors found a 2 to 4 fold enhancement with respect to Maxwell's theory (see Equation 2.1), with nanoparticle volume fractions as low as 1%. One interesting contribution in this publication is the use of particle size distributions in terms of volume percent instead of particle count. However, when considering the solid-fluid interface heat transfer mechanism for nanofluids, Myers et al. (2013) suggested that the THW technique could give misleading measurements of anomalous thermal conductivity enhancement if a static heat flow model applied over an infinite domain is used instead of applying a dynamic model over a finite domain.

Similar to the INPBE (Buongiorno et al., 2009), the work by Barbes et al. (2014) on CuO nanofluids (water and ethylene glycol) also indicates that classical models (Hamilton and Crosser, 1962), or their generilized version (Nan et al., 1997), give a good estimation of the effective thermal conductivity of nanofluids. In this study the heat capacity was also measured. The experimental apparatus used was a differential heat-flow microcalorimeter. Experiments were conducted with different nanoparticle volume fractions and different temperatures. Besides finding that thermal conductivity follows classical models, the authors also suggested the increase in the effective thermal conductivity with temperature is related to the thermal conductivity increase of the base fluid and not to the presence of the particles. One of the main arguments of Barbes et al. (2014) work is that the differential heat-flow microcalorimeter technique eliminates possible sources of error, because the measurements are made with very small temperature gradients and with practical absence of natural convection.

Despite the widely accepted conclusions from the INPBE, more recent publications continue to report anomalous enhancements of thermal conductivity in nanofluids. One example is the case of nanodiamonds in mineral oil (ND/MO) based nanofluids reported by Taha-Tijerina et al. (2014). In this study, nanoparticle volume fractions as low as 0.100 wt % registered an enhancement in thermal conductivity close 70% at 373 K. While the results at room temperature (296 K) from Taha-Tijerina et al. (2014) agree with the INPBE, at higher temperatures a significant deviation from the mean field theory was measured. This led the authors to suggest that Brownian motion may play an important role in abnormally enhancing the thermal conductivity of nanofluids.

2.2.2 Momentum Transfer

The study of fluid flow of nanoparticles suspensions is closely related to the potential applications of heat transfer enhancement nanofluids have to offer. Initially, the study of momentum transfer focused mainly on determining the effect of volume fraction on pumping power. Early measurements of viscosity indicate that the penalty in pressure drop for suspending the nanoparticles was very low compared with the gain in heat transfer enhancement (Masuda et al., 1993; Choi, 1995).

Li et al. (2002) measured the viscosity of CuO-water nanofluids at different temperatures. The measurements indicated a decrease in viscosity with temperature, with a less important dependency on nanoparticle volume fraction. Das et al. (2003a) measured the dynamic viscosity of Al_2O_3-water nanofluids. They found that this particular nanofluid shows an increase of viscosity with particle concentration but remains Newtonian in nature. Similar results were obtained by Prasher et al. (2006c) on Al_2O_3-PG (propylene glycol) nanofluids; however, the viscosity measured was much higher than the value predicted by Einstein's model, but this was likely due to aggregation of the nanoparticles as pointed out by the authors.

Kwak and Kim (2005) measured the zero shear and the shear-dependent viscosity for CuO-EG (ethylene glycol) nanofluids. The particles in this system were rod-like with an aspect ratio of 3. They found that at concentrations above the dilute limit ($\phi = 0.20\%$) the zero-shear viscosity increases drastically with nanoparticle volume fraction. The measurements of shear-dependent viscosity indicate a shear thinning behavior with a infinite shear viscosity similar to that of the base fluid. A similar shear thinning behavior was observed by Ding et al. (2006) in the study of CNT nanofluids. They also reported a viscosity increase with CNT concentration and a decrease with temperature.

Zhou et al. (2010) investigated experimentally shear rate and temperature dependencies of viscosity on alumina (nanospheres and nanorods) polyalphaolefin (PAO) nanofluids. Nanofluids with low particle concentration (1 and 3%) show Newtonian behavior and no temperature dependency, except for the case of nanorods at 3% volume fraction, which showed non-Newtonian features (shear thinning) and strong dependency on temperature.

Li et al. (2013) studied a viscoelastic fluid-based nanofluid (VFBN) composed of cetyltrimethyl ammonium chloride/sodium salicylate as base fluid and multi-walled carbon nanotubes (MWCNTs) as nanoparticles. Thermal conductivity and shear viscosity were studied experimentally. The VFBNs behaves similarly to the viscoelastic base fluid, as a shear-thinning non-Newtonian fluid. A significant increase in the shear viscosity at low shear rates was observed. Furthermore, the authors reported a significant increase in thermal conductivity with nanoparticle volume fraction.

More recently, Taha-Tijerina et al. (2014) investigated nanodiamond in mineral oil (ND/MO) based nanofluids for potential thermal management applications; in particular studying viscoelastic properties. It was determined that the ND/MO based nanofluids behave like Newtonian fluids at the concentrations studied (≤ 0.100 wt %). The temperature dependency of the dynamic viscosity revealed the importance of considering ND nanoparticle interactions in these studies.

2.2.3 Mass Transfer

Despite the promising results reported by Ahuja (1976) and Mehra (1988) for micro-meter size particle suspensions, the study of mass transfer in nanofluids have received significantly less attention than heat transfer has. However, over the past few years the attention is slowly being shifted towards the promising mass transport enhancement of nanofluids. Ali et al. (2004) investigated the heat and mass transfer between air and falling ultrafine Cu particle solution film in a cross flow configuration. This study indicated that the ultrafine particles enhance heat and mass transfer. Furthermore, increasing particle volume fraction increases dehumidification and cooling capabilities.

Wen et al. (2005) studied the gas holdup and the gas-liquid volumetric mass transfer coefficient in an airlift reactor with dispersed 12 nm TiO_2 nanoparticles. The authors found a decrease in the volumetric mass transfer coefficient with particle volume fraction. This decrease was attributed to the reduced interfacial area caused by the easy coalescence of bubbles in the presence of nanoparticles.

Olle et al. (2006) reported a 600% oxygen mass transfer enhancement using magnetite (Fe_3O_4) nanofluids. They showed that the mass-transfer coefficient and the interfacial area are enhanced in the presence of nanoparticles, with the interfacial enhancement being more important. Furthermore, the enhancement in the volumetric mass transfer coefficient showed a strong temperature dependence.

Krishnamurthy et al. (2006) visualized dye diffusion in a 20 nm Al_2O_3-water nanofluid. They observed that dye diffuses up to 14 times faster in the presence of nanoparticles, with a peak enhancement at $\phi = 0.5\%$. An important conclusion from this work is that "an order-of-magnitude analysis suggests that the Brownian motion of the nanoparticles is not directly responsible for the observed mass transport enhancement. Rather, it is the velocity disturbance field in the fluid, created by the motion of the nanoparticles, that could be responsible for such enhancement".

Fan et al. (2007) conducted experiments to study the effect of nanofluids on bubble behavior. They used hydrophilic nanoparticles with bubble flows in bubble columns and microchannels. The experimental measurements revealed a significant increase in the gas holdup in bubble columns. Also, the microchannel experiments showed a reduction of bubble size in the presence of the nanofluid, which would yield an entirely different flow regime map compared to the base fluid.

Fang et al. (2009) studied diffusion of Rhodamine B in Cu-water nanofluids using a method based on Taylor dispersion. They found a strong dependency of the effective mass diffusivity on nanoparticle volume fraction and temperature; 10.71 fold increase at 15°C and 26 times increase at 25°C. These results led them to conclude that Brownian motion induced micro-convection inside the suspension fluid remarkably enhances the mass transfer process.

The many-fold increase in mass diffusivity for nanofluids was put in question when measurements of self-diffusion on SiO_2-water nanofluid gave a decrease in the effective mass diffusivity with nanoparticle volume fraction (Turanov and Tolmachev, 2009). The measured decrease was faster than predicted by effective medium theory, and it was attributed to interaction of water with the silica particles and water retention by the nanoparticles. Similar results were also obtained for Al_2O_3-water nanofluids (Gerardi et al., 2009). In this case the authors concluded that two effects could be responsible for the observed decrease with nanoparticle volume fraction: tortuosity of the diffusion path, or the presence of an ordered layer on the surface of the particle with lower diffusion coefficient than the free molecules.

Ozturk et al. (2010) used a microfluidic approach to measure tracer diffusion of 20-nm Al_2O_3-water nanofluids, with experimental conditions similar to Krishnamurthy et al. (2006). The results from these experiments showed that the nanoparticles did not enhance dye diffusion and reported the presence of a zone of highly fluorescent dye-nanoparticle complexes at the interface between dye and nanofluid. Ozturk et al. (2010) also suggest that the anomalous threadlike spreading patterns reported by Krishnamurthy et al. (2006) primarily depict flow-induced deformation of the droplet front, which are effects introduced by physical phenomena and not by enhancements in molecular diffusion.

Veilleux (2010) measured the diffusion of Rhodamine 6G in Al_2O_3-water nanofluids using a new technique based on Total Internal Reflection Fluorescence (TIRF) microscopy (Veilleux and Coulombe, 2010a,b, 2011). The authors found a 10-fold maximum dye diffusivity at 2% volume fraction, compared to diffusivity in pure water. The significant increase in mass diffusivity was explained using a dispersion-based model. Temperature, particle density, particle size and nanoparticle volume fraction dependency of the effective mass diffusivity in terms of the dispersion model were discussed. The dispersion model proposed is based on the postulate that micro-convection takes place due to the nanoparticle Brownian motion, and suggests that mass diffusivity in nanofluids depends on the Péclet number. While the dispersion model predicts an observable increase in mass diffusivity with nanoparticle volume fraction, by extending the dispersion model to heat transfer, the authors concluded that the the enhancements in heat diffusivity are expected to be within measurement error.

Subba-Rao et al. (2011) studied dye diffusion of Alexa-488 in silica-water and Rhodamine 6G in alumna-water nanofluids, using Fluorescence Correlation Spectroscopy (FCS). The studies indicated no significant changes in mass diffusivity at the nanoparticle volume fractions studied (1% for alumina and 1.7% for silica).

Ashrafmansouri and Nasr Esfahany (2014) published a review on mass transfer in nanofluids. This review is not limited to studies in mass diffusivity as discussed above, but it also includes convective mass transfer with many types of equipment: agitated absorption reactor, falling film absorption system, amongst others. The authors also suggest particle Brownian motion and associated micro-convection as a possible mechanisms for mass diffusivity enhancement. This review also included publications where a decrease on mass diffusivity with nanoparticle volume fraction was observed. This reduction in mass diffusivity was explained by: aggregation/-clustering and increase in tortuosity in diffusion path in the presence of nanoparticles.

The important mass transfer enhancements reported by Olle et al. (2006) and Krishnamurthy et al. (2006) have opened a new door in nanofluids research. Potential applications of nanofluids in areas other than heat transfer are now being considered. Some examples include improving mass transfer limited systems such as bioreactors, reacting systems, microfluidics, amongst others. Fundamental understanding of this particular phenomena is currently an important area for research.

2.3 Theoretical Developments

This section presents relevant theoretical developments towards understanding heat and mass transfer phenomena in nanofluids. Although studies have been published in nanofluids momentum transfer, this section focuses on heat and mass transfer and in particular on thermal conductivity and mass diffusivity. First, models developed to estimate the thermal conductivity of composite materials are introduced. Then, recently suggested modifications of these models to account for the nanofluid's unique behavior are presented, followed by one of the few models proposed to explain mass diffusivity characteristics of nanofluids. Finally, the section concludes with some numerical studies performed to get a better understanding of the heat transfer mechanisms in nanofluids at different scales.

2.3.1 Composite Materials

Also known as "classical" models, these were developed to calculate the thermal (and electrical) conductivity of composite materials. They are often compared against experimental measurements on nanofluids. The discrepancy between experimental measurements and the estimation using these classical models is what is called "abnormal" or "anomalous" enhancement in the literature. Some of these classical models are presented next.

Maxwell (1873) presented a generalized theory for conduction through heterogeneous media. Although, it was presented mainly for electric conduction, the analogy to heat conduction is straightforward. Using this theory, the author developed a formula to calculate the effective resistance of an heterogeneous medium with non interacting spheres, i.e. the radius of the sphere is much smaller than the distance between them:

$$\frac{\lambda_{\mathrm{eff}}}{\lambda_{\mathrm{f}}} = \frac{\lambda_{\mathrm{p}} + 2\lambda_{\mathrm{f}} + 2(\lambda_{\mathrm{p}} - \lambda_{\mathrm{f}})\phi}{\lambda_{\mathrm{p}} + 2\lambda_{\mathrm{f}} - (\lambda_{\mathrm{p}} - \lambda_{\mathrm{f}})\phi} \tag{2.1}$$

Equation (2.1) has been rearranged from the original publication to represent the effective conductivity ratio ($\lambda_{\mathrm{eff}}/\lambda_{\mathrm{f}}$) for a solid-liquid composite, i.e. ratio between the effective conductivity λ_{eff} and the conductivity of the base fluid λ_{f}. Also, λ_{p} represents the particle conductivity and ϕ the volume fraction. This formula indicates that the effective conductivity of a medium composed of particles suspended in a liquid depends only on the conductivities of the fluid and particles, and the volume fraction occupied by the particles. Equation (2.1) is only valid for dilute systems; however, when particle interactions are important other terms enter into the equation. Note that Eq. (2.1) is indicated as Maxwell's equation through out this work.

The case of insulating spherical particles ($\lambda_{\mathrm{p}} = 0$) is of particular interest in the study of mass diffusion in composites with impermeable inclusions. The effective mass diffusion coefficient for a composite material can be obtained from Eq. (2.1) by replacing λ_{eff} with D_{eff}, the effective mass diffusivity, and λ_{f} with D_{m}, the molecular mass diffusivity of solute A in medium B (dilute binary diffusion). Using the assumption of a dilute suspension ($\phi < 1$ and $\phi^2 \approx 0$), Eq. (2.1) becomes:

$$\frac{D_{\mathrm{eff}}}{D_{\mathrm{f}}} = 1 - \frac{3}{2}\phi \tag{2.2}$$

Hamilton and Crosser (1962) extended the approach use by Maxwell (1892) to mixtures containing particles of arbitrary shapes; Eq. (2.3). In this equation, n is a shape constant that must be determined empirically. A mathematical expression for n for ellipsoidal particles had already been developed by Fricke (1924); however, close forms for other particle shapes were not feasible. Instead, the authors correlated the experimental data obtained for non spherical particles to Eq. (2.3) by setting $n = 3/\Psi$, where Ψ is the sphericity (ratio of the surface area of a sphere with a volume equal to that of the particle, to the surface area of the particle).

$$\frac{\lambda_{\mathrm{eff}}}{\lambda_{\mathrm{f}}} = \frac{\lambda_{\mathrm{p}} + (n-1)\lambda_{\mathrm{f}} - (n-1)(\lambda_{\mathrm{f}} - \lambda_{\mathrm{p}})\phi}{\lambda_{\mathrm{p}} + (n-1)\lambda_{\mathrm{f}} + (\lambda_{\mathrm{f}} - \lambda_{\mathrm{p}})\phi} \tag{2.3}$$

Besides being applicable only to dilute suspensions, Eq. (2.3) also assumes that all particles have similar shape and that they are randomly oriented. Furthermore, when studying more complex systems, the authors suggest to assume Eq. (2.3) to account for the conductive heat transfer of the heterogeneous array and then incorporate the contributions from other factors that may cause an abnormal behavior.

Jeffrey (1973) extended the work of Maxwell (1892) to calculate the heat flux exactly to order ϕ^2 by using the renormalization method described by Batchelor (1972). Using this approach, the problem can be reduced to the pair interactions of particles. The result obtained depends on the way pairs of spheres are distributed. Equation (2.4) presented below corresponds to the case of randomly distributed particles; with $\beta = (\alpha - 1)/(\alpha + 2)$ and $\alpha = \lambda_{\mathrm{p}}/\lambda_{\mathrm{f}}$.

$$\frac{\lambda_{\mathrm{eff}}}{\lambda_{\mathrm{f}}} = 1 + 3\beta\phi + \phi^2 \left(3\beta^2 + \frac{3\beta^3}{4} + \frac{9\beta^3}{16} \frac{\alpha + 2}{2\alpha + 3} + \frac{3\beta^4}{2^6} + ... \right) \tag{2.4}$$

Yamada and Ota (1980) developed a new model based one the work of Fricke (1924) and Hamilton and Crosser (1962) by representing each particle as a parallelepiped of dimensions a, b, c. The modifications introduced to these models account for other particle shapes and mutual interactions between neighboring particles. The form of the unit-cell model, as named by the authors, is the same as Eq. (2.3) with a different expression for n given by Eq. (2.5).

$$(n - 1) = M \left(\frac{a}{L} \right)^{n_1} \left(\frac{b}{L} \right)^{n_2} \left(\frac{c}{L} \right)^{n_3} \tag{2.5}$$

In Eq. (2.5), the term L is define as $L = (abc/\phi)^{1/3}$. The constants M, n_1, n_2, and n_3 in Eq. (2.5) are not easy to determine theoretically. Therefore, the authors proposed a method to find them from experimental data using linear regression. Furthermore, for particles with non-parallepiped shapes a method for calculating the equivalent parallelepiped dimensions was also proposed. The unit-cell model fitted well experimental data available in the literature; except for the cases of cylinders with large aspect ratios and some results with spherical particles.

Davis (1986) obtained an expression for the thermal conductivity of a composite material containing spherical inclusions, accurate to order ϕ^2. The expression obtained was similar to the one presented by Jeffrey (1973). However, this method has the particularity that a decaying temperature field is used. As a result, only convergent integrals are encountered, and the renormalization factor proposed by Batchelor (1972) is not needed.

Bonnecaze and Brady (1990) presented a general method to predict the effective conductivity of an infinite statistically homogeneous suspension of particles in an arbitrary (ordered or disordered) configuration. The method follows closely that of "stokesian dynamics" and captures both far-field and near-field particle interactions accurately with no convergence difficulties. This method was applied to random suspensions of spherical particles (Bonnecaze and Brady, 1991) with very good results when compared with experimental data.

2.3.2 Nanofluid Models: Thermal Conductivity

Modifications to the classical models have been proposed to account for the abnormal thermal conductivity reported in the literature. In general, these modifications intent to account for phenomena irrelevant at the micrometer range, but perhaps significant at the nanometer scale. Four mechanisms for this abnormal enhancement are often found in the literature (Keblinski et al., 2002): 1) Brownian motion of the nanoparticles, 2) molecular-level layering of the liquid at the liquid/particle interface, 3) the nature of heat transport in the nanoparticles, and 4) effects of nanoparticle clustering. Some of the models presented below include these mechanisms.

Particle Brownian motion originates form thermal energy fluctuations of the fluid molecules. Even though Brownian motion also affects micrometer size particles, as the size of the particle decreases the importance of these fluctuations on the random motion of the particle increases. The effective thermal conductivity dependance on particle size (Jang and Choi, 2007) and temperature (Das et al., 2003b; Chon et al., 2005) suggests that particle Brownian motion plays an important role in the heat transfer mechanism in nanofluids.

One of the first modifications to Maxwell model to include particle Brownian motion and particle aggreagtion was proposed by Xuan et al. (2003).

$$\frac{\lambda_{\mathrm{eff}}}{\lambda_{\mathrm{f}}} = \frac{\lambda_{\mathrm{p}} + 2\lambda_{\mathrm{f}} + 2(\lambda_{\mathrm{p}} - \lambda_{\mathrm{f}})\phi}{\lambda_{\mathrm{p}} + 2\lambda_{\mathrm{f}} - (\lambda_{\mathrm{p}} - \lambda_{\mathrm{f}})\phi} + \frac{\rho_{\mathrm{p}}\phi c_{\mathrm{p}}}{2\lambda_{\mathrm{f}}}\sqrt{\frac{\lambda_{\mathrm{B}} T}{2\pi a_{\mathrm{c}}\eta}} \tag{2.6}$$

where λ_{B} is the Boltzmann constant, a_{c} is the cluster apparent radius, ρ_{p} is the particle density, c_{p} is the particle specific heat capacity, and η is the fluid viscosity. Two important facts are captured by this model: a) the thermal conductivity of nanofluids increases with temperature, and b) the formation of aggregates reduces the efficiency of the energy transport enhancement of the suspended particles. However, the temperature dependence of this model ($T^{1/2}$) was not in agreement with the experimental data from Das et al. (2003b).

To account for the strong thermal conductivity dependence on temperature, Kumar et al. (2004) proposed a model based on the Stokes-Einstein formula, thus including the Brownian motion of the particles Eq. (2.7). The model also captures the dependance on particle size.

$$\frac{\lambda_{\mathrm{eff}}}{\lambda_{\mathrm{f}}} = 1 + c\frac{2\lambda_{\mathrm{B}} T}{\pi\eta d_{\mathrm{p}}^2}\frac{\phi d_{\mathrm{f}}}{\lambda_{\mathrm{f}}(1-\phi)d_{\mathrm{p}}} \tag{2.7}$$

where c is a constant found to be of the order of unity, η is the dynamic viscosity of the base fluid, d_p is the diameter of the particles, and d_f is the diameter of the base fluid molecules, assumed to be spheres. This model indicates that the effective thermal conductivity of nanofluids varies in proportion to T/η and $1/d_\mathrm{p}$. Even though a good agreement with experimental data was found, not enough information was given about c and d_f in the calculations presented, which might have been used as fitting parameters.

The model proposed by Koo and Kleinstreuer (2004) accounts for the static particles thermal conductivity enhancement using Maxwell's model, and for the dynamic contribution by considering the surrounding liquid traveling with Brownian moving nanoparticles Eq. (2.8).

$$\frac{\lambda_\mathrm{eff}}{\lambda_\mathrm{f}} = \frac{\lambda_\mathrm{p} + 2\lambda_\mathrm{f} + 2(\lambda_\mathrm{p} - \lambda_\mathrm{f})\phi}{\lambda_\mathrm{p} + 2\lambda_\mathrm{f} - (\lambda_\mathrm{p} - \lambda_\mathrm{f})\phi} + 5 \times 10^4 \gamma \phi \rho_\mathrm{p} c_\mathrm{p} \sqrt{\frac{\lambda_\mathrm{B} T}{\rho_\mathrm{p} d_\mathrm{p}}}\, f(T, \phi) \tag{2.8}$$

$$f(T, \phi) = (-6.04\phi + 0.4705)T + (1722.3\phi - 134.63) \tag{2.9}$$

where γ is related to particle motion and can be obtained by fitting experimental data obtained at constant temperature. This model was found to be in good agreement with experimental data. However, the use of the empirical functions γ and $f(T, \phi)$ restrict the extrapolation of the model to other systems.

Another interesting modification to Maxwell's model to include the effect of particle Brownian motion was proposed by Prasher et al. (2005); presented in Eq. (2.10). In this publication, Brownian motion was proposed as the primary mechanism responsible for the enhancement in the effective thermal conductivity. Maxwell's model was modified by introducing the convection of the liquid near the particles through a new correlation proposed by the authors:

$$\frac{\lambda_{\mathrm{eff}}}{\lambda_{\mathrm{f}}} = \left[\frac{\lambda_{\mathrm{p}} + 2\lambda_{\mathrm{f}} + 2(\lambda_{\mathrm{p}} - \lambda_{\mathrm{f}})\phi}{\lambda_{\mathrm{p}} + 2\lambda_{\mathrm{f}} - (\lambda_{\mathrm{p}} - \lambda_{\mathrm{f}})\phi}\right] \left(1 + A\,\mathrm{Re}^{m}\,\mathrm{Pr}^{0.333}\phi\right) \tag{2.10}$$

where A and m are fluid dependent constants, Pr is the Prandtl number ($\mathrm{Pr} = \eta/\alpha$, where α is the thermal diffusivity), and Re is the Reynolds number:

$$\mathrm{Re} = \frac{1}{\eta}\sqrt{\frac{18\lambda_{\mathrm{B}}T}{\pi\rho_{\mathrm{p}}d_{\mathrm{p}}}} \tag{2.11}$$

Models including molecular-level layering of the liquid at the liquid-particle interface have also been proposed in the literature. They exploit the increase in surface area with decrease in particle size to explain the size-dependent enhancement observed experimentally. The models developed using this approach are normally modifications to the Maxwell or Hamilton-Crosser models, where the particle conductivity is replaced by an effective particle conductivity representing the particle and the interfacial layer (Yu and Choi, 2003, 2004; Leong et al., 2006).

Despite the fact that experimental evidences have proven the existence of a liquid-particle interface layering (Yu et al., 1999), the values of the layer thickness needed to explain experimental data are much higher than the ones estimated using non-equilibrium molecular dynamics (Xue, 2003; Xue et al., 2004). This suggests that the abnormal nanofluid thermal conductivity enhancement cannot be explained by thermal transport in the liquid-solid interface layer.

The ballistic phonon transport proposed by Keblinski et al. (2002) could contribute to the abnormal thermal conductivity enhancement of nanofluids. Since the mean free path of a phonon is comparable to the nanoparticle diameter (∼35 nm), important enhancements in the conductivity are expected when particle are close, thus phonons can propagate directly from one particle to the other.

Aggregation kinetics was proposed by Prasher et al. (2006b) as a possible explanation for the observed anomalies reported in experimental work. They found that aggregation decreases the Brownian motion due to the increase in the mass of the aggregates, whereas it can increase the thermal conductivity due to percolation effects in the aggregates (enhanced heat transfer by touching particles in the aggregate). This study introduced other important parameters that had received little attention in the past studies of nanofluids. For example the Hamaker constant, the zeta potential, pH, and ion concentration. These parameters influence the formation of aggregates, thus the thermal conductivity of the nanofluid.

Two independent groups developed models to study heat transfer in nanofluids, and in particular to study the results from hot transient wire measurements. Myers et al. (2013) developed a time-dependent model to determine the thermal conductivity of a nanofluid. The model does not require contribution from Brownian motion or nanolayers to explain the abnormal enhancements measured. The proposed equation for the effective thermal conductivity considering transient terms is

$$\lambda_{\mathrm{eff}} = \frac{\lambda_{\mathrm{f}}}{(1-\phi^{1/3})^2}\left[(1-\phi)+\phi\frac{\rho_{\mathrm{p}}c_{P\mathrm{p}}}{\rho_{\mathrm{f}}c_{P\mathrm{f}}}\right]\frac{n-1}{2(n+1)}\left[\frac{1+\phi^{1/3}}{2}-\frac{1}{n+1}\right]^{-1} \tag{2.12}$$

where $n = 2.233$ is a fix value, because the formula is only valid for cases where the particle to base fluid conductivity ratio is much larger than one. For particle volume fractions higher than 1% this model shows a greater enhancement than Maxwell model.

Marín et al. (2014) constructed a model from experimental measurements of two immiscible fluids using THW. The experimental results were explained by an improved series model that takes into account the interfacial resistance. The proposed model relies on a single fitting parameter. In the case of nanofluids this parameter depends on particle size. Using the improved model the authors conclude that experimental measurements using THW techniques cannot be interpreted using classical models; instead the improved series model needs to be used.

An alternative interpretation of the results form Myers et al. (2013) and Marín et al. (2014) would be that the THW techniques for measuring thermal conductivity of nanofluids would lead to an overestimation of this property. The effective conductivity given by Eq. (2.12) would not be a property of the macroscopic fluid, but a characteristic of the system; closer to a heat transfer coefficient than a thermal conductivity.

2.3.3 Nanofluid Models: Mass Diffusivity

The study of mass transfer had a late start. One of the early models to explain the abnormal enhancement on mass diffusivity in nanolfuids was published by Veilleux and Coulombe (2010a). The main idea behind this model is that the enhancement is due to Brownian motion induced dispersion, similar to Taylor dispersion phenomena on straight tubes. The model was developed as an analogy with dispersion in diluted fixed beds, using Brinkman velocity profile. Particle velocities are obtained by sampling the Maxwell-Boltzmann distribution. The dispersion model obtained shows a strong dependence on the Péclet number, which explains why nanofluids exhibit larger enhancements on mass diffusivities compared to thermal diffusivity. If Brownian motion is responsible for enhancement, it would be too small to be detected in heat transfer situations. This in in agreement with the generally accepted view that there is no observable "abnormal" increase of the heat conductivity past the values predicted by classical "composite" models.

2.4 Numerical Investigations

Numerical experiments have become a popular tool to study phenomena that occurs at scales (i.e. time and length) where experimentation may be limited. For example, Molecular Dynamics (MD) simulations have been used in the study of nanofluids to estimate the importance of thermal resistance at the liquid-solid interface (Xue et al., 2003), to validate the existence of a liquid layering at the interface (Xue et al., 2004), and to study the importance of particle Brownian motion (Keblinski and Thomin, 2006; Sarkar and Selvam, 2007). However, MD simulations are limited to molecular scale interactions and particle interactions cannot be easily integrated into this framework.

Taking a different approach to overcome some of the limitations of MD simulations, Bhattacharya et al. (2004) used Brownian dynamics simulations to compute the effective thermal conductivity. The good agreement with the experimental data indicates that particle Brownian motion plays an important role in the thermal conductivity enhancement of nanofluids. However, two fitting parameters were needed for the model to be compared with the experimental data. Unfortunately, this publication only presented the results from the model fitting and no validation was performed to test if the model also accounts for temperature and particle size dependency.

Qiao and He (2007) used Dissipative Particle Dynamics (DPS) to study energy transfer in a nanocomposite. Even though, this method has only been used for nanocomposites where Brownian motion is not important, there is a clear potential to extend this approach to nanofluids. Similar to the Lattice Boltzman Method (Xuan and Yao, 2005), DPD uses the interaction of groups of molecules to model a system. This permits the modeling of different scales within the same framework, making these approach very attractive in the study of nanofluids. The study of nanoparticle suspensions was performed subsequently by the same group (He and Qiao, 2008). "Brownian motion of nanoparticles play a negligible role in determining the thermal conductivity" was the main conclusion from this study on nanofluids using DPD.

Many of the Lattice Boltzmann Method (LBM) based models for nanofluids have considered the entire fluid-particles as a continuum (Xuan and Yao, 2005; Wu and

Kumar, 2005). In these cases particle Brownian motion is introduced into the simulations as random noise, force term, in the LBM equations. In these cases the Nusselt number is the parameter of interest.

Khiabani et al. (2010) used the LBM to study heat transfer in microchannels with suspended particles. In this case the particles and the fluid are treated as separate entities. However, the particles are stationary or allowed to move with the fluid. Brownian motion is not included in the simulation and the system simulated is two dimensional, limiting the analysis to cylindrical particles. As for previous uses of the LBM to study nanofluids, the Nusselt number is the parameters of interest. The authors concluded that the presence of the particles increased the local Nusselt number, thus enhancing heat transfer to the microchannel.

Cui et al. (2012) used the LBM to estimate the effective diffusion coefficient of nanofluids. The method is divided in two parts; first particle and fluid are considered as separate entities and the root mean square velocity of the particle is calculated. The limitation of this first approach to only a few particles insitated the second approach. In the second part, particles are considered point sources, a similar approach to that of Wu and Kumar (2005), where the contribution of Brownian motion is included as a random force. The authors concluded that the micro-perturbation of nanoparticles greatly enhances mass transfer.

Zarghami et al. (2013) proposed a model based on LBM to simulate nanofluids in plane Poiseuille and backward-facing step flows. As indicated before, the main part of LBM applied to nanofluids has focused on a macroscopic view of the problem.

In this work the effective thermal conductivity is given by a complex equation that includes classical models for composite materials, Brownian motion, and effects of inter-particle potentials. Zarghami et al. (2013) focused the attention on calculating the Nusselt number. They found that low thermal conductivity particles lead to a more pronounced enhancement of the Nusselt number within the vortex zone, while high-conductivity particles are more effective outside the vortex zone.

In a more recent publication, Babaei et al. (2013) used equilibrium molecular dynamics to provide "proof" that the contribution form Brownian motion-induced micro-convection to the thermal conductivity enhancement on nanofluids is insignificant. The simulations were done with a single Cu sphere carved into a matrix of methane atoms, at a temperature around 100K. The authors also show that equilibrium molecular dynamics can lead to erroneous high estimation of the effective thermal conductivity: "while the individual terms in the heat current autocorrelation function associated with nanoparticle diffusion achieve significant values, these terms essentially cancel each other if correctly defined average enthalpy expressions are subtracted".

Part II

Mathematical Model

Chapter 3
Methodology

The general methodology implemented to estimate the effective thermal conductivity and mass diffusivity of nanofluids is summarized in this chapter. The different constituents of the methodology are presented in detail in the following chapters.

3.1 Method of Solution

This study begins with the postulate that the effective thermal (λ_{eff}) and mass (D_{eff}) diffusivities are affected by micro-convection currents generated by the particles under Brownian motion. This proposition sets the requirements for the mathematical model: 1) micro-convection currents due to Brownian motion need to be fully resolved, and 2) an average or effective coefficient, time and space independent, is to be calculated from the simulation results.

Figure 3–1 describes the main parts of the computational method selected. The first step of the process is to simulate Brownian motion. This is accomplished by the use of the fluctuating Lattice Boltzmann Method (fLBM), where the fluid molecular fluctuations are directly included in the simulation. These fluctuations interact with the particles making them move in a Brownian-like fashion. The final objective of

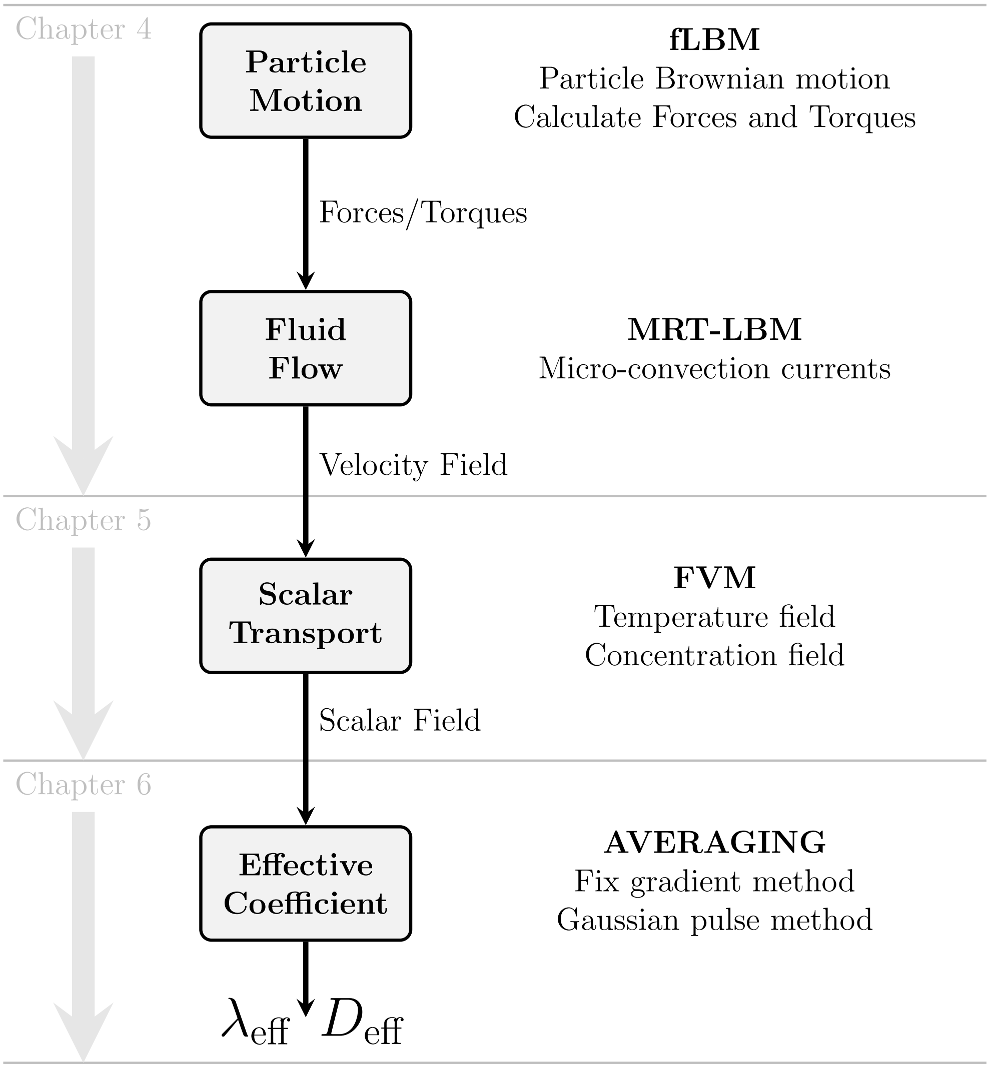

Figure 3–1: Schematic representation of numerical model proposed to calculate effective diffusion coefficients, λ_{eff} and D_{eff}.

this part of the simulation is to calculate the forces and torques that affect each particle at a given time step.

In the second part of the simulation the fluid flow field is calculated. This is accomplished by performing another Lattice Boltzmann step (MRT-LBM), this time without molecular fluctuations. In this case, the forces and torques calculated in the previous part are used to move the particles using Newton's second law of motion. The output of this step is a velocity field that does not contain molecular fluctuations. More details of the first and second steps are given in chapter 4 (Fluid Flow and Particle Motion).

The third step uses energy or species conservation equations to calculate temperature or concentration fields. The velocity field from the second step is used here to describe the convective part of the conservation law. The solution of the conservation equations gives a scalar field that describes temperature or concentration changes in time and space. The transport equations are solved using the Finite Volume Method (FVM). Details on the implementation and integration with the LBM are presented in chapter 5 (Scalar Transport).

The final step in the process is to calculate effective λ_{eff} and D_{eff} from the scalar field calculated in the previous step. This is accomplished by special averaging over time and space. For this purpose, two methods of estimating the effective diffusivities were developed: 1) the fixed gradient method, and 2) the Gaussian pulse method. Both of these methods are described in detail in chapter 6 (Estimation of Effective Diffusivities).

3.2 Computational Domain

The computational domain used for the simulations is a cubic volume filled with fluid and spherical particles. The size of the cubic volume and the number of particles used in the simulations depend on particle volume fraction, ϕ. Examples of different computational domains are shown in Figure 3–2. Two different particle arrangements were used in the simulations: primitive cubic and random. The primitive cubic arrangement is shown on the left side of Figure 3–2 for three different particle volume fractions. Random arrangements are shown on the right side of Figure 3–2 at the same particle volume fractions as the primitive cubic arrangements.

Particle size was controlled by changing the lattice size, therefore the same arrangements shown in Figure 3–2 would be used for the simulation with different particle sizes. The study of mono-disperse suspensions is not a restriction of the methodology, it was a choice made in this exploratory analysis. The case of bidisperse suspensions will be briefly discussed in chapter 9.

Particles were discretized using a staircase-like approximation. The domain is discretized into cubic cells; each cell can represent a volume of fluid or a volume of particle. This imposes the staircase-like representation of the particles, adding limitations to particle movement that will be briefly discussed in the next chapter.

The number of cells representing a particle is given by the diameter of the particle in lattice units (LU). There is a trade off-between discretization error and size of the computational domain. The larger the number of cells used to represent a particle

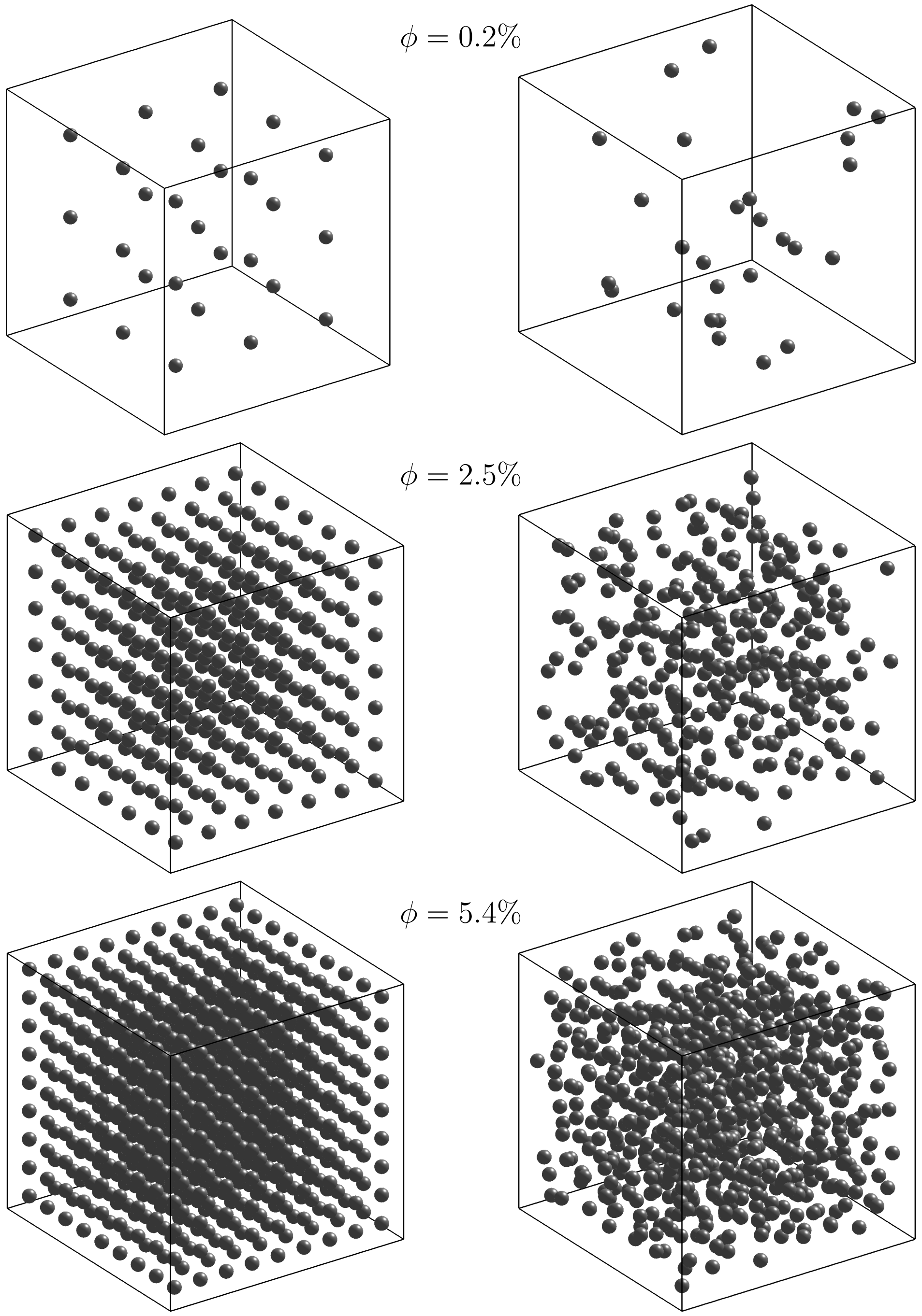

Figure 3–2: Representation of the computational domain for three different particle volume fractions. Particles in primitive cubic arrangement (left) and random arrangement (right).

the smaller the discretization error, thus better representing the geometry. However, this would also imply a larger domain would be needed to represent the same number of particles.

Tests were performed using different particle diameters. A particle diameter of 10 LU was found to be a good compromise between geometry discretization and the size of the domain needed for the particle volume fractions studied.

3.3 Boundary and Initial Conditions

In general, periodic boundary conditions were used in the simulations. There are few exceptions, but these will be indicated when needed. Periodic boundary conditions are used with the objective of approximating an infinite domain. However, periodic boundaries imply the repetition of the same domain in all directions. If only one particle were to be simulated, then the larger domain would be an array of particles, similar to the arrays in Figure 3–2 (left). When particle motion is added, the simulation would represent the motion of an array.

To reduce the impact of the symmetry introduced by the periodic boundaries on particle motion, the domain simulated needs to include many particles. In most simulations the random arrangement of particles is used for this purpose. Even if the particles were placed in an array arrangement, the simulation with moving particles would not behave as a single moving array.

Due to limitation of the LBM solver used (see next chapter), the particles are confined to the computational domain, because periodic boundaries for the particles have not been implemented. This means that particles cannot leave the domain through one side while another particle enters the opposite boundary. To avoid having particles crossing the boundaries, the initial position of the particles was set at least 2 cells from the boundary. Also, an artificial force was included to push the particles towards the interior if they get too close to the boundary. This issue only affects simulations with a random arrangement of particles. In simulations with array arrangements the particles are already far form the boundaries. Since both types of arrangements give similar results, the array arrangement is used mainly for validation.

3.4 General Assumptions

The main assumption made in developing the model presented in the following chapters is that macroscopic conservation laws for heat and mass transfer apply. This carries with it the assumption that the fluid phase can be considered a continuum. Furthermore, no slip between the particles and the fluid was also assumed. The validity and impact of this assumption on the results have not been studied. However, this assumption was made based on the work by Einstein (1905), where the mobility term is obtained by using Stoke's law.

From the thermodynamic point of view the entire domain is at the same temperature, thus all physical properties are constant (i.e. density, viscosity, conductivity, heat capacity), they only depend on the material, fluid or particle. This assumption has no impact in mass transfer simulations, but it would be inconsistent with heat transfer simulations. In the case of heat transfer, particle and fluid motions are calculated using this assumption. When solving the energy equation, the temperature changes are small enough that physical properties can be assumed constant.

Added to the assumption of constant properties, thermophoresis and diffusiophoresis are also ignored in the model. This is one interesting characteristic of numerical experiments, where the phenomenon of interest, Brownian motion in this case, can be isolated from other phenomena always present in physical experiments. Other phenomena that have been excluded from the simulations are: viscous dissipation, coagulation or agglomeration, and van der Waals forces.

The particles are assumed to be well dispersed and far from each other. This assumption constrains the applicability of the model to dilute dispersion. In this work the maximum particle volume fraction simulated is of the order of $\phi = 5\%$. Even at this low concentration the dilute system assumption does not hold, because particle approach each other to a distance smaller than 6 cells. When the distance between the particles is too small, the hydrodynamic forces are not well captured by the model. The lubrication approximation is commonly used to solve this issue (Dünweg and Ladd, 2009), however this has not been used in this work.

Chapter 4
Fluid Flow and Particle Motion

The procedure to calculate particle motion and fluid flow is described in this chapter. A brief introduction to the fLBM technique is presented here for completeness. Some of the details presented in this section will be used in the following chapters. For a complete description of the LBM see Succi (2001) and for fLBM see Ladd (1994a,b). Dünweg and Ladd (2009) is a good starting point when considering simulation of colloidal systems. This publication focuses on the LBM and the fluctuating LBM (fLBM), and includes a good summary of other available simulation techniques for colloidal systems.

The software implementation was obtained from waLBerla framework (widely applicable Lattice Boltzmann from Erlangen, Feichtinger (2012)). WaLBerla is a software framework suitable for multi-physics simulations centered around the lattice Boltzmann method. This framework has been designed to be extendable and scalable on massively parallel supercomputers. The waLBerla framework allows to include physical phenomena not available by default. One example is the FVM included as part of the solution steps (see chapter 5). This framework can also be used in many types of supercomputers available through Compute Canada. Since its design is centered on parallel execution, it is easily scalable to many processors in a wide range of hardware, including GPUs.

Although, the fLBM is the first step in the method of solution, the fLBM is a particular case of the LBM. Therefore, the LBM is introduced first, followed by the modifications on the LBM needed to obtain the fLBM. Only a brief description of these methods is presented here. The objective is to present the important parts for the development of the hybrid LBM-FVM presented in chapter 5.

4.1 Lattice Boltzmann Method (LBM)

An alternative to the macroscopic view given by the Navier-Stokes equation is the Boltzmann transport equation (BTE). The probability density or distribution function $f(\vec{x}, \vec{p}, t)$ describes the probable number of particles with momentum $\vec{p}$ near a small volume about the point $\vec{x}$ at time t. The differential equation describing the spatial and temporal evolution of f is the BTE Succi (2001). Practically, the BTE is composed of two parts, a streaming motion of molecules along trajectories associated with the force field around the volume in question, and a second part describing the two-body collisions taking molecules in and out of the streaming trajectories.

The lattice Boltzmann equation given by Eq. (4.1) is obtained after linearizing the collision term and discretizing the BTE. This is achieved by discretizing space into a cubic lattice with constant length Δx. The phase space $\vec{p}$ is discretized by allowing only few velocity/momentum directions. These directions are called the lattice velocity $\vec{c}_i$ and the distribution function associated with it is denoted by f_i. Finally, time is discretized by taking fixed time steps Δt. The lattice velocities are selected in a way that after a complete time step the distribution f_i moves to the neighbor cell pointed by the direction of $\vec{c}_i$.

$$f_i(\vec{x}+\vec{c}_i\Delta t, t+\Delta t) - f_i(\vec{x}, t) = \Delta_i(f - f^{eq}); \qquad i = 1, ..., N \tag{4.1}$$

The number of lattice velocities allowed, N, depens on the dimensionality of the problem and the physics involved. In this work only the classical D3Q19 is used. This indicates space discretization for a three dimensional case (D3), using nineteen lattice velocities (Q19). The directions of each $\vec{c}_i$ component are indicated graphically in Figure 4–1. The upper left box represents a single cubic cell of the lattice discretization. The arrows shown in the figure correspond to eighteen discretized velocities, plus $i = 0$ corresponding to the distributions not streamed after a time step is taken. The numbers in Figure 4–1 correspond to the index i of the velocities c_i or the distributions f_i.

The graphical representation of the discretized velocities in Figure 4–1 differs from the typical representations found in the literature, since a precise description of the velocities should go from one node to the next neighbor in the direction of the velocity in question. In this representation the velocities are shown to go only to the sides of the cell, in other words, the arrow in Figure 4–1 represents only half of the velocities $\vec{c}_i$. This representation will become handy when discussing the hybrid LBM-FVM.

The left-hand side of Eq. (4.1) is known as the stream operator because it represents the displacement of the distribution f_i to the next neighbor in the direction $\vec{c}_i$. A graphical representation of this operator for the D2Q9 case is presented in

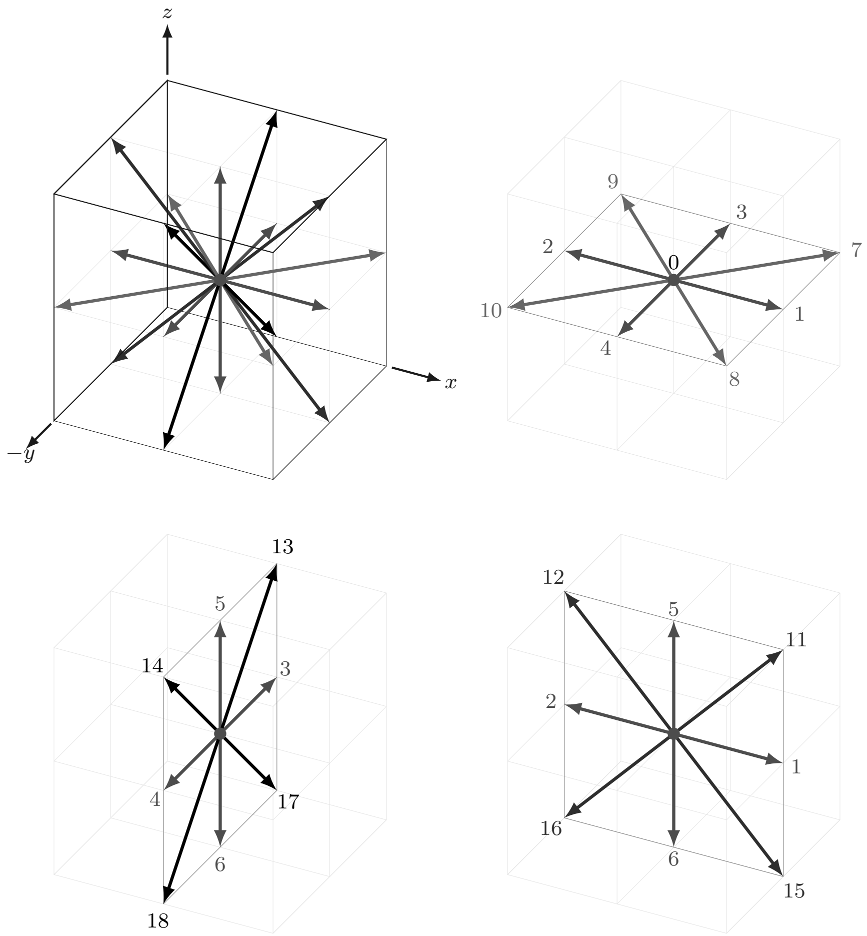

Figure 4–1: Graphical representation of discretized velocities for the LBM (D3Q19). All components in a single cell (top left), xy components (top right), yz components (bottom left), and xz components (bottom right).

Figure 4–2. In this figure the post-collision distributions are denoted by the $\hat{f}_i$ and the standard f_i indicate the pre-collision distributions. The center cell is indicated as the gray zone in the center of the grid. The nodes of the grid are indicated by the black circles in the center of the cells. It is also common to refer to the neighbor cells using cardinal directions, as shown in the figure.

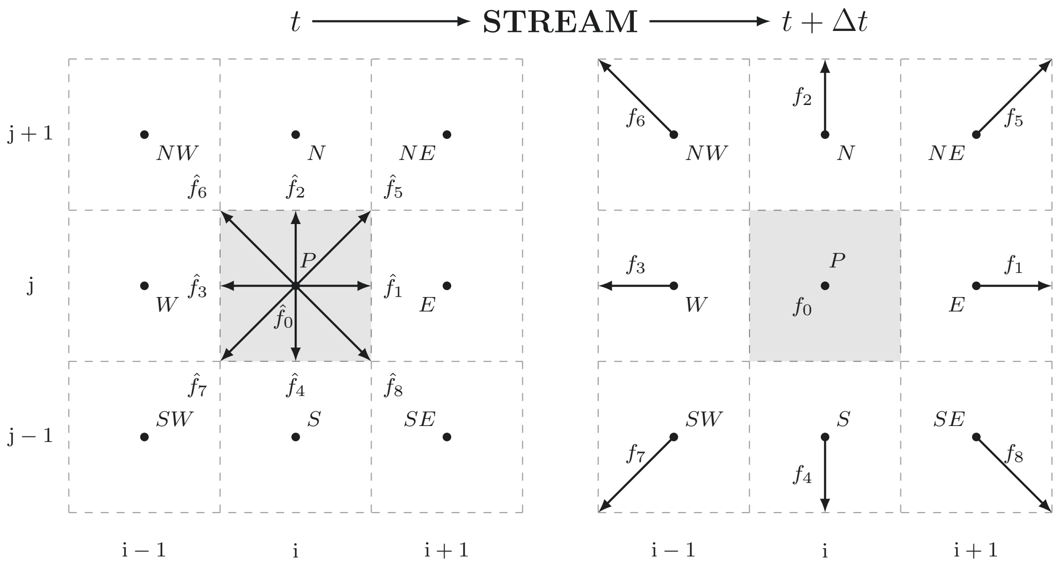

Figure 4–2: Graphical representation of the stream step for the LBM (D2Q9).

The arrows in Figure 4–2 are labeled with the corresponding distribution, however, the arrow corresponds to $\vec{c}_i$, indicating the streaming direction for a given distribution. Similar to Figure 4–1, these arrows only indicate half the distance streamed by $\vec{c}_i \Delta t$. One important characteristic of the stream operator is that all distribution functions, except f_0, cross the walls of the lattice cell. Also, the stream operator does not change f_0, thus, $f_0 = \hat{f}_0$.

The term Δ_i represents the discrete collision operator applied to $(f - f^{eq})$. This operator is defined depending on the type of simulation, however it must satisfy mass and momentum conservation in the hydrodynamic limit, i.e. macroscopic scale. In general, this operator should describe the tendency of f_i to go towards its equilibrium f_i^{eq}.

A graphical representation of the collision operator is shown in Figure 4–3. In this figure, only a single cell is shown with three different sets of distributions. The left most square represents the post-stream distributions. The equilibrium distributions are represented by the square in the middle, and finally the square on the right are the new distributions calculated from the post-stream and the equilibrium distributions. The arrows in Figure 4–3 indicate the direction of the lattice velocity, but in this case the length of the arrow indicates the magnitude of the corresponding distribution. This figure is a representation of distribution relaxation towards equilibrium.

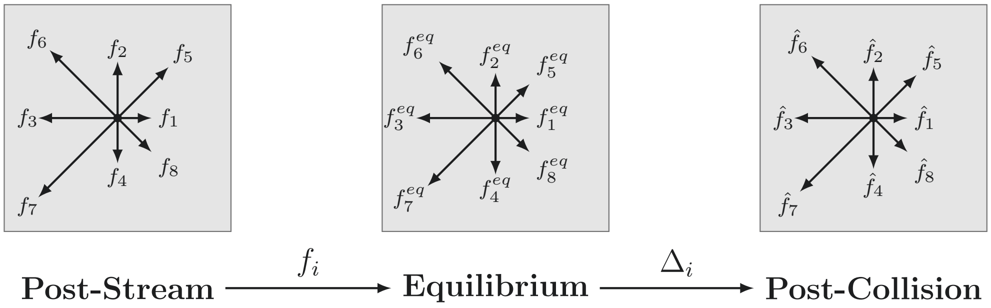

Figure 4–3: Graphical representation of the collide step for the LBM (D2Q9).

One of the most important characteristics of the collision operator is that none of the distributions crosses the cell boundaries during collision, therefore it is inherently mass conserving. Although not shown in Figure 4–3, the collision operator is the only one that can change the value of f_0.

The most common representation of the collision operator is the BGK model (Bhatnagar, Gross and Krook), which uses a single relaxation time to describe the evolution of f_i towards equilibrium. In this thesis, however, the MRT (Multiple Relaxation Time) model is used instead (d'Humieres et al., 2002). The MRT also relaxes f_i towards equilibrium, however, each mode (i.e. the moments describing mass, momentum and stresses) can be relaxed using different relaxation times. The MRT collision term is given by (MRT-LBM)

$$\Delta_i(f - f^{eq}) = E^\top D E(f_i - f_i^{eq}); \qquad i = 1, ..., N \tag{4.2}$$

where, D is a diagonal matrix composed of the relaxation times $(\lambda_1, ..., \lambda_N)$, and E is an orthogonal transformation matrix that transfers $f^{neq} = (f_i - f_i^{eq})$ from velocity space to moment space.

The equilibrium distribution f^{eq} can be derived from the Maxwell-Boltzmann distribution. For the LBM the equilibrium distribution is given by

$$f_i^{eq} = w_i \rho \left(1 + \frac{\vec{c}_i \cdot \vec{u}}{c_s^2} + \frac{(\vec{c}_i \cdot \vec{u})^2}{2c_s^4} - \frac{\vec{u}^2}{2c_s^2}\right) \tag{4.3}$$

where $c_s = \frac{1}{\sqrt{3}}\frac{\Delta x}{\Delta t}$ is the speed of sound on the lattice and w_i are model dependent weights (see Succi (2001) for details).

Since the local equilibrium distribution function in Eq. (4.3) depends on macroscopic variables, density $\rho(\vec{x}, t)$ and velocity $\vec{u}(\vec{x}, t)$, these are calculated from the moments of the distribution

$$\rho = \sum_{i=0}^{18} f_i \tag{4.4}$$

$$\rho\vec{u} = \sum_{i=0}^{18} \vec{c}_i f_i \tag{4.5}$$

In short, the LBM is composed of two operators, the stream operator and the collision operator. The collision operator requires the local equilibrium distribution to be known. At every time step the LBM performs a collision step followed by a stream step. The time evolution of the macroscopic variables, density and velocity is then obtained from the moments of the distribution, Eq. (4.4) and Eq. (4.5), respectively. These steps are repeated for every time step, thus obtaining the time evolution of the density and velocity fields. Some examples of these results are shown at the end of the chapter.

In contrast to Navier-Stokes equation solvers, boundary conditions for the LBM are imposed by setting the distribution functions. In this work only the bounce back type of boundary conditions are used at the particle surface (see section 4.4). All other boundaries are set to periodic, which implies copying the distributions to the proper neighbor cell. See Succi (2001) for details on other types of boundary conditions.

4.2 The Fluctuating Lattice Boltzmann Method (fLBM)

The fluctuating LBM was developed by Ladd (1993, 1994a,b). Over the last years the general methodology has changed very little. One of the important contributions to the subject was done by Dünweg et al. (2007), where the fluctuating LBM is presented from the statistical mechanics point of view.

The main objective of the fLBM is to incorporate thermal fluctuations into the LBM to simulate the continuous random motion of molecules. This is done by incorporating a stochastic collision operator into the LBM. The fluctuation-dissipation is satisfied by enforcing consistency with fluctuating hydrodynamics (Landau and Lifshitz, 1959). See Dünweg and Ladd (2009) for detail on the fLBM. The new form of the collision operator including the stochastic contribution, $\tilde{R}$ is

$$\Delta_i(f - f^{eq}) = E^{\top} D E (f_i - f_i^{eq}) + \tilde{R}; \qquad i = 1, ..., N \tag{4.6}$$

The new collision operator mush still conserve mass and momentum, and conform to some statistical properties such as vanishing mean and a covariance matrix giving the correct fluctuations at the hydrodynamic level. It is assumed to be local in space and time, no correlation with other cells or times. The variance of the fluctuations in the fLBM is given by

$$\mu = \frac{k_B T \Delta t^2}{c_s \Delta x^5}$$

A practical advantage of the fLBM is that the MRT-LBM is recovered if the stochastic collision is removed. Therefore, MRT-LBM or fLBM can be simulated with the same code; switching from fLBM to MRT-LBM can be done by simply removing the random noise. The details of the implementation within the waLBerla framework can be found in Neumann (2008).

Similar to the MRT-LBM, the fLBM can be used to calculate the time evolution of the velocity and density fields. However, the velocity field in the fLBM also includes the fluctuations from the molecules. This field cannot be used in the conservation equations of energy or species because of the fluctuations. For this reason a MRT-LBM is used after, this time without the stochastic collision term. The MRT-LBM provides an estimation of the average velocity, that without molecular fluctuations.

4.3 Dimensionless form of the LBM

Since the grid used is a regular lattice with a single dimension and a single time step, it is customary to normalize the equations in the MRT-LBM. A proper selection of length, time and mass scales will help eliminate many terms, thus simplifying the software implementation and the analysis. The scales selected depend on the computational domain at hand and not on the physical problem. This is different from the normalization usually done when solving transport equations.

The scales used in the normalization of Eq. (4.1) are: a) length scale Δx, b) time scale Δt, and c) mass scale ρ_0. Using these scales the following dimensionless quantities are obtained:

$$\Delta x^* = \frac{\Delta x}{\Delta x} = 1; \qquad \Delta t^* = \frac{\Delta t}{\Delta t} = 1 \qquad \rho_0^* = \frac{\rho_0}{\rho_0} = 1$$
$$\vec{u}^* = \vec{u}\frac{\Delta t}{\Delta x} \qquad \nu^* = \nu\frac{\Delta t}{(\Delta x)^2}$$

The quantities with full dimensions are used throughout this work, except on chapter 5, where the hybrid LBM-FVM is developed, and in some figure in the rest of this chapter. In chapter 5 the * notation which indicates dimensionless quantities is dropped to improve readability. Dimensionless quantities are indicated in figures and tables when using lattice units, [LU].

4.4 Particle Motion

Particle motion is obtained by calculating forces on the surface of the particle and integrating Newtons's second law of motion to obtain the velocity and displacement of each particle. Particle motion is handled by a different framework called the Physics Engine (PE) (Iglberger et al., 2008). This framework allows parallel simulation of a large number of particles. However, one of the main drawbacks with the version used in this work is the lack of periodic boundaries for the particles.

From the fluid point of view two calculations are required when dealing with particles. First, calculate the forces the fluid exerts on the surface of the particle, and second, apply boundary conditions to account for the moving particles.

The forces on the surface of the particles are summarized using a single force and torque at the center of mass, $\vec{R}$. The force and torque information is then used to move the particles using the PE.

Once the particles are moved, the next step is to recalculate the fluid field. At this point the boundary conditions at the surface of the particle are updated. The only requirements to calculate the distributions at the particle-fluid interfaces are the velocities of the particle, linear ($\vec{U}$) an angular ($\vec{\Omega}$). The implementation of the moving boundary condition is similar to the classical bounce back boundary conditions, but the motion of the particle is considered by modifying the mirroring distributions

$$f_i(\vec{x}, t + \Delta t) = f_i(\vec{x}, t) - \frac{2w_i \rho \vec{u}_b \cdot \vec{c}_i}{c_s^2}$$

The local velocity of the particle surface, $\vec{u}_b$, is given by

$$\vec{u}_b = \vec{U} + \vec{\Omega} \times (\vec{x}_b - \vec{R})$$

Brownian motion takes place in the simulation thanks to thermal fluctuations introduced during the fLBM step. Molecular fluctuations exert uneven forces on the surface of the particle. The forces and torques for each particle at each time step are then stored. In the second step, the MRT-LBM uses the forces and torques stored to move the particles, which in turn move the fluid, thus obtaining the micro-convection currents.

4.4.1 Force and Torque Characteristics

Forces and torques on the particles have very specific characteristics, an example is presented in this section. The particles under consideration are 2 nm in diameter, with specific gravity of 4.0 and particle volume fraction of 0.82%. To obtain the forces and torques only the fLBM part is required. The simulation was run for 30000 time steps and the position, velocity, angular velocity, force and torque values for the particle were stored.

The histogram of the force and torque data is shown in Figure 4–4. The thick line in the figure represents the continuous normal probability function calculated from the mean and standard deviation of the data. The objective of this line is to compare graphically the histogram to a normal distribution. As shown in Figure 4–4, forces and torques are both normally distributed with zero mean and their respective standard deviations, $\sigma_F = 0.3403$ for the force and $\sigma_\tau = 0.7723$ for the torque; both in dimensionless or lattice units.

Another important characteristic of forces and torques is given by their correlation functions. The auto-correlation function (ACF) and the cross-correlation function (XCF) for the force component are presented in Figure 4–5. The ACF corresponds to the x component and the XCF corresponds to the x/y pair. The curves shown in Figure 4–5 correspond to the average of 500 particles. Similar graphs where obtained for other components and combinations of them. This figure indicates that the random forces and torques acting on the particles are autocorrelated, but they are uncorrelated with the orthogonal components. Therefore, for the length and

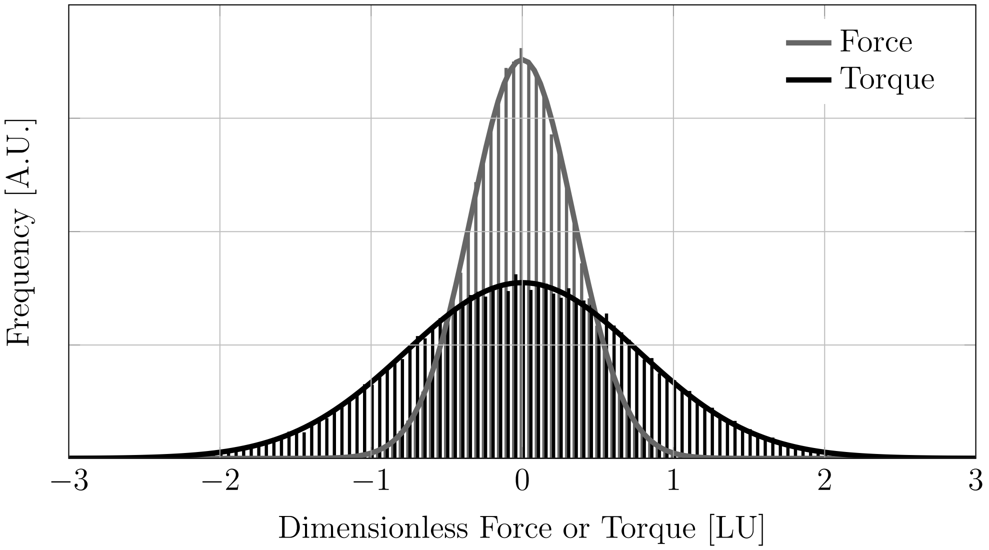

Figure 4–4: Forces and torques histogram from the fLBM simulation.

time scales used in the simulations the forces and torques cannot be prescribed by a simple Gaussian random number generator.

The negative values of the ACF shown in Figure 4–5 correspond to the fluid resistance to particle motion. At the same time that particles move due to the thermal fluctuations, the molecules around the particle oppose to this movement.

4.4.2 Particle Velocity and the Maxwell-Boltzmann Distribution

Similar to the analysis done for forces and torques, the linear and angular velocity histogram is shown in Figure 4–6. The linear velocity is normally distributed with zero mean and 7.53×10^{-4} standard deviation. The angular velocity is also normally distributed with zero mean and 3.10×10^{-4} standard deviation, both values dimensionless.

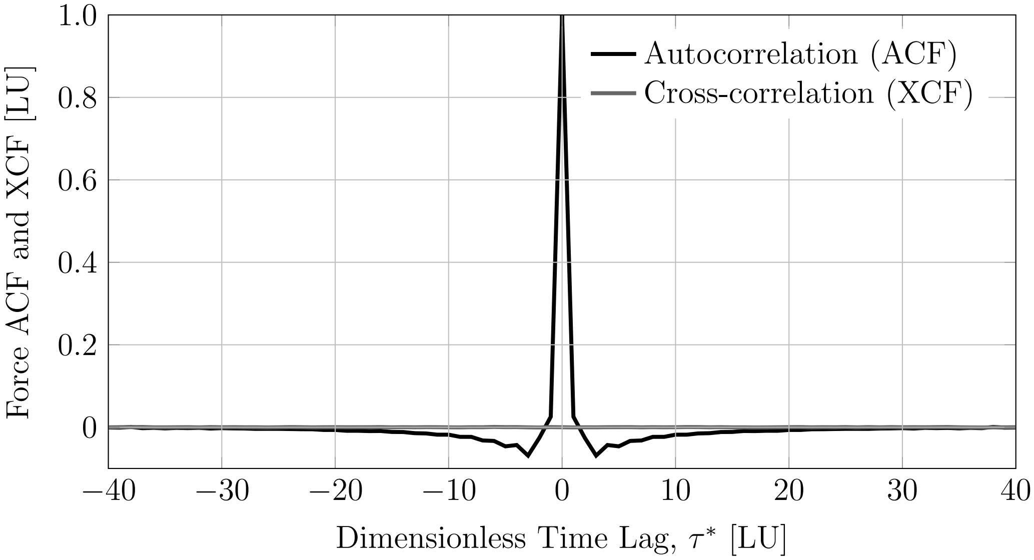

Figure 4–5: Force auto correlation function (ACF) and cross correlation function (XCF). Average of 500 particles.

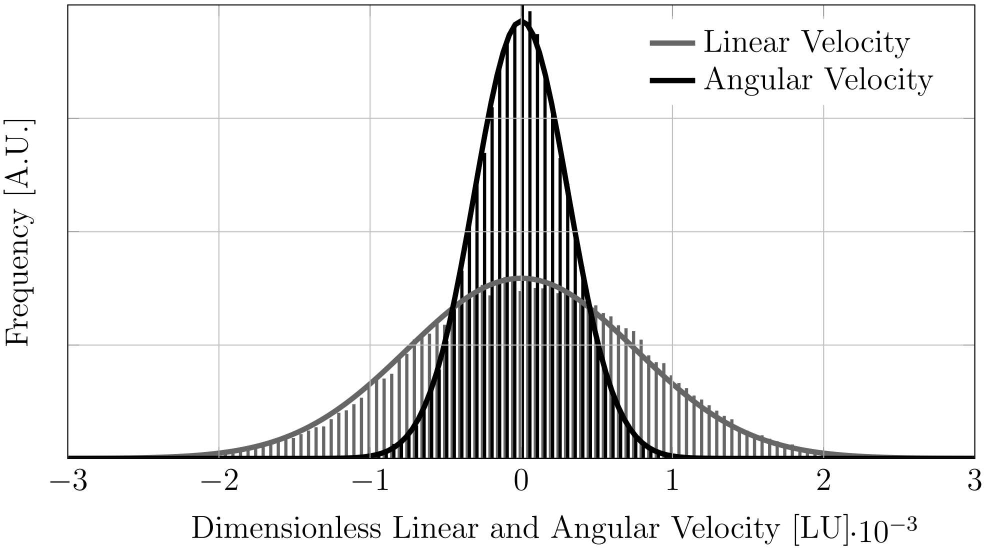

Figure 4–6: Linear and angular velocity histogram from the fLBM simulation.

The ACF for the linear and angular velocities are presented in Figure 4–7. This figure clearly indicates that the velocity vectors are auto-correlated. The linear velocity autocorrelation extends for a larger number of time lags compared to the angular velocity autocorrelation. This indicates that the particle velocity at a given time depends on previous values of the velocity. The cross-correlation (not shown in Figure 4–7) indicates that the velocity components are not correlated for either linear and angular velocity components.

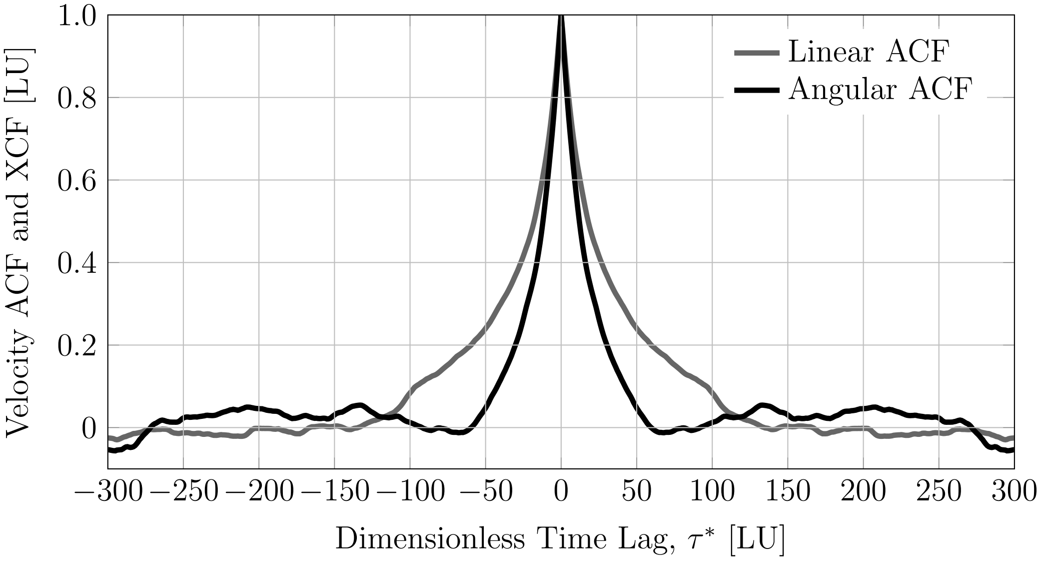

Figure 4–7: Linear and angular velocity auto-correlation function (ACF) and cross-correlation function (XCF). Single particle.

The auto-correlation obtained for the velocity vectors are expected results, since the velocity of the particle is determined by the second law of motion. The slow decay of the autocorrelation function can be used to calculate the particle diffusion coefficient. This is done in the next section.

4.4.3 Mean Square Displacement and Particle Self-Diffusion Coefficient

The particle self-diffusion coefficient is given by a well-known relation (Einstein, 1905)

$$D_s = \lim_{t\to\infty} \frac{\left\langle \left|\vec{r}_i(t) - \vec{r}_i(0)\right|^2 \right\rangle}{6t} = \frac{\langle \Delta R^2(t) \rangle}{6\,t} \tag{4.7}$$

where $\langle \Delta R^2(t) \rangle$ is the mean squared displacement (MSD). Although, it is possible to calculate the MSD from the position information of each particle, it is common to use the velocity autocorrelation function (VACF) instead (Ladd, 1994b). The MSD can be calculated using the VACF by using the following relationship (Lowe and Frenkel, 1996).

$$\frac{\langle \Delta R^2(t) \rangle}{6\,D_s\,t} = \frac{\left\langle \left|\vec{r}_i(t) - \vec{r}_i(0)\right|^2 \right\rangle}{6\,D_s\,t} = \frac{1}{D_s} \int_0^t \left(1 - \frac{s}{t}\right) Z(s)\,\mathrm{d}s \tag{4.8}$$

where the velocity autocorrelation function, $Z(t)$, is defined as

$$Z(t) = \frac{1}{3} \langle \vec{u}(t) \cdot \vec{u} \rangle = \langle u(t)_x \cdot u_x \rangle$$

See Hansen and McDonald (2006, sec. 7.2) for derivation details of Eq. (4.8). Note that Eq. (4.8) has been normalized by the MSD limiting value, $6\,D_s\,t$, thus giving a single curve between 0 and 1 when plotted against the reduced time t/τ. This scaling is commonly used when studying the evolution of the MSD at short-times (Dünweg and Ladd, 2009). Figure 4–8 shows the scaled MSD against the reduced time for a typical simulation. Besides highlighting the important relationship between the VACF and the MSD, the main objective of this analysis was to validate the proper simulation of particle Brownian motion by the waLBerla and PE frameworks. The results obtained agree with the ones presented by Dünweg and Ladd (2009).

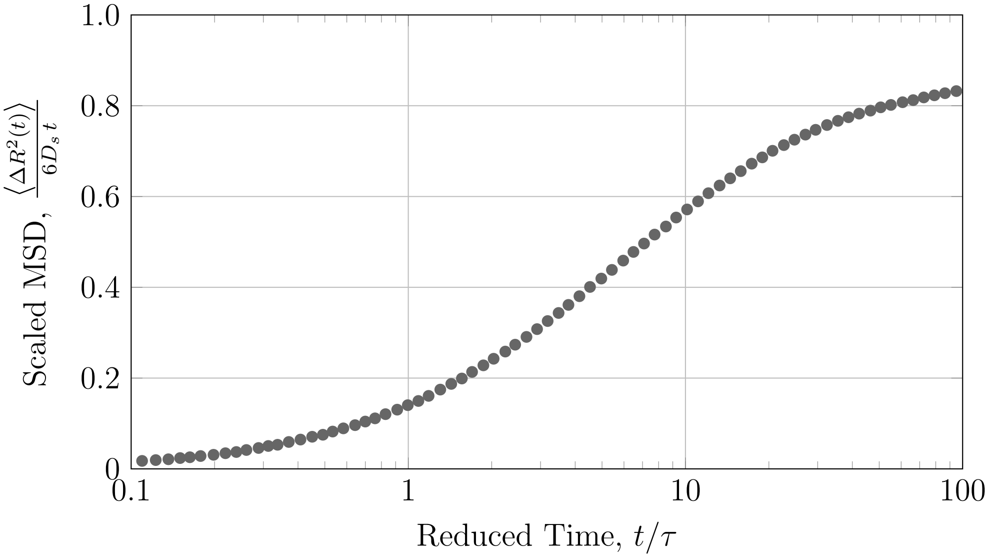

Figure 4–8: Normalized MSD vs. reduced time for 125 evenly placed particles at 1.0% volume fraction.

The results shown in Figure 4–8 follow closely those reported by Dünweg and Ladd (2009), thus the waLBerla and PE frameworks together can be used for simulating particle Brownian motion.

4.4.4 Particle Size and Velocity

Another interesting characteristic of the particle velocity is that the diameter of a Brownian particle can be calculated from the variance of the particle velocity. Based on the equipartition of energy theorem, each particle should have a component speed that is normally distributed with zero mean and a standard deviation given by

$$\sigma_{u_i} = \sqrt{\frac{k_B T}{m}}$$

Given the standard deviation of each component speed, the equivalent hydrodynamic particle diameter can be calculated from

$$d_p^H = \sqrt[3]{\frac{6 k_B T}{\rho \pi \sigma_{u_i}^2}}$$

This characteristic is used here as a validation test. Simulations with different particle diameters in lattice units and physical units were performed to determine if particles move in a Brownian-like fashion. The results from these simulations are presented in Table 4–1. This table compares the particle diameter, d_p, with the equivalent hydrodynamic particle diameter, d_p^H. In all cases the equivalent diameter ratio is larger than one, indicating the particles behave as if they were larger than intended. The difference between the diameter set and the hydrodynamic diameter can be attributed to discretization error of the geometry and the staircase approximation of the spherical particles.

In general, all simulations with a particle diameter of 5 LU give almost the same ratio. Also, increasing the particle size in lattice units shows no effect on the ratio for values above 10. Although, any particle size could be used in the simulations because of the small error introduced, the 10 LU diameter will be used for all simulations.

Table 4–1: Particle diameter (d_p) and hydrodynamic diameter (d_p^H) for different particle discretization settings.

ID	d_p^* [LU]	d_p [nm]	d_p^H [nm]	Ratio
1	5	5	5.4	1.087
2	10	10	10.4	1.041
3	15	15	15.4	1.028
4	20	20	20.7	1.033
5	25	25	26.4	1.055
6	5	10	10.9	1.087
7	5	15	16.3	1.087
8	5	20	21.7	1.086
9	5	25	27.2	1.086
10	5	100	108.7	1.087
11	5	1000	1087	1.087
12	10	5	5.2	1.038

4.5 Fluid Flow Field Around Brownian Particles

Typical velocity fields obtained from the fLBM and MRT-LBM are shown in Figure 4–9. This figure shows isosurfaces of the magnitude of the velocity. The darker the surface the higher the magnitude of the velocity. The particles are indicated by the solid spheres (no transparency).

Figure 4–9 is a representation of the Brownian motion-induced micro-convection currents calculated by the MRT-LBM. These currents extend from the particle and occupy the entire domain, even for particle volume fractions as low as 0.5% shown in this figure. The vast amount of information provided by these currents are not studied in detail in this project. The flow field is an intermediate result in the calculation of the scalar field evolution over time, discussed in the next chapter.

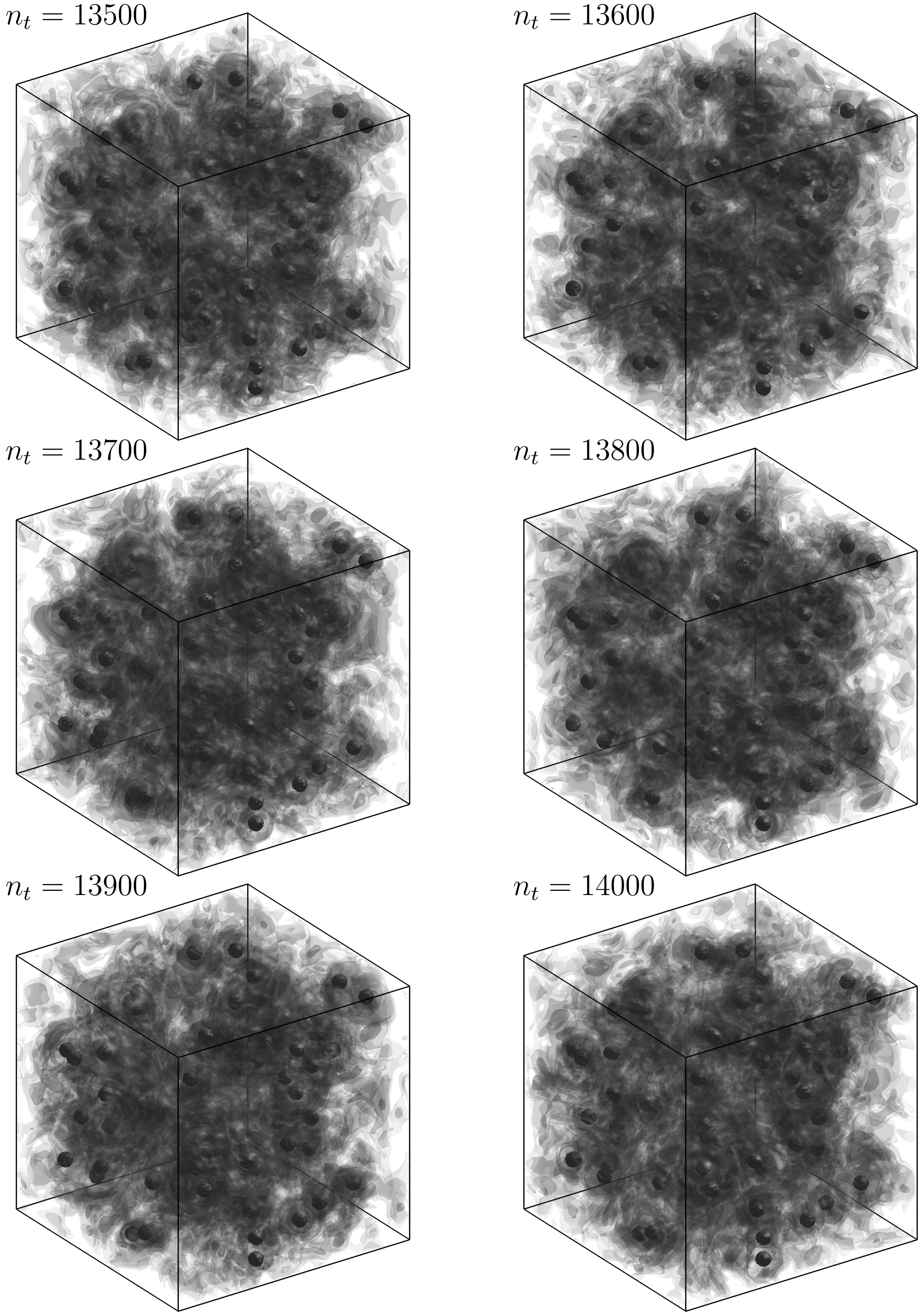

$n_t = 13500$

$n_t = 13600$

$n_t = 13700$

$n_t = 13800$

$n_t = 13900$

$n_t = 14000$

Figure 4–9: Evolution of micro-convection currents on a 0.5% volume fraction nanofluid. Isosurfaces for the velocity magnitude. Darker shade of gray indicates higher velocity magnitude.

Chapter 5
Scalar Transport

In the previous chapter the LBM was used to obtain the velocity field. In this chapter the conservation equations for heat and mass transport are discretized using the FVM. The FVM implementation is briefly discussed, however the most important contribution of this chapter is the introduction of a new approach to integrate the fluid field from the LBM (or MRT-LBM) into the FVM: the Hybrid LBM-FVM.

5.1 Finite Volume Method (FVM)

The FVM is a well-known discretization method used for solving conservation equations. The method used here is the one introduced by Patankar (1980). Another practical reference for the FVM is the book by Versteeg and Malalasekera (1995). The details of this method are not discussed here, only a few important concepts needed for the development of the hybrid LBM-FVM are presented. In general, the nomenclature used in this chapter follows that of Patankar (1980). Some alterations were made to avoid confusion with the LBM nomenclature.

The FVM uses the following general conservation equation for the dependent variable ψ, assuming the source term is negligible

$$\frac{\partial}{\partial t}(\rho\,\psi) + \nabla\cdot(\rho\,\vec{u}\,\psi) = \nabla\cdot(\Gamma\nabla\psi) \tag{5.1}$$

Placing the energy conservation equation is this form, one obtains:

$$\frac{\partial}{\partial t}(\rho c_P\, T) + \nabla \cdot (\rho c_P\, \vec{u}\, T) = \nabla \cdot (k \nabla T) \tag{5.2}$$

Similarly, for mass transfer the conservation of species can be written as

$$\frac{\partial}{\partial t}(\rho\, \omega_A) + \nabla \cdot (\rho\, \vec{u}\, \omega_A) = \nabla \cdot (\rho D_{\mathrm{m}} \nabla \omega_A) \tag{5.3}$$

The discretization of the general conservation equation also implies that the continuity equation is satisfied. For the general case the continuity equation is given by

$$\frac{\partial \rho}{\partial t} + \nabla \cdot (\rho \vec{u}) = 0 \tag{5.4}$$

The discretization of Eq. (5.1) gives a series of algebraic linear equations. The convection-diffusion terms were discretized using central-differences, while time derivatives were discretized using the Crank-Nicolson method. The resulting linear equations were solved using an iterative solver, a parallel geometric multi-grid solver with a Jacobi smoother (Köstler, 2011). Boundary and initial conditions are discussed in the next chapter.

5.2 The Velocity Field on Staggered Grids

On important characteristic of the FVM is the use of staggered grids for the velocity field. This is done to avoid pressure fields satisfying mass and momentum conservation but that are physically unreal. This is only required when solving the fluid field using the FVM. A typical 2D control volume is shown in Figure 5–1. The quantities F_e, F_w, F_n and F_s correspond to the integrated total mass flow over the control volume faces.

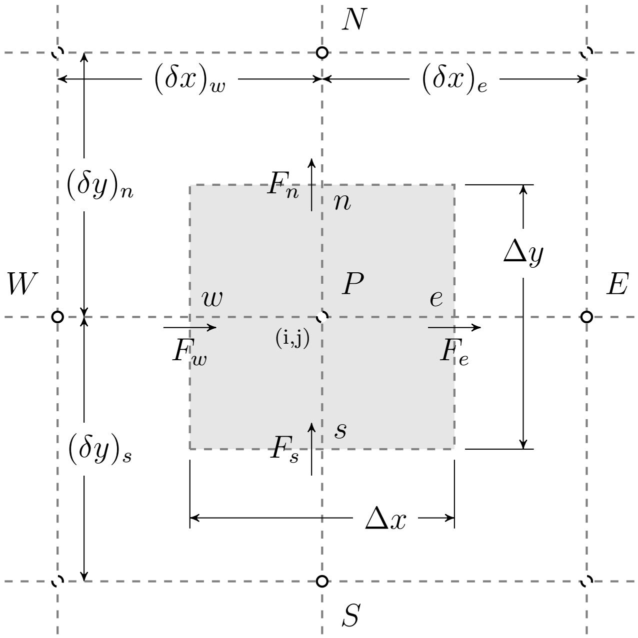

Figure 5–1: Representation of a 2D FVM grid and control volume.

The empty circles in Figure 5–1 indicate the gird points, where the dependent variable is calculated. These points are the same for the LBM solver, therefore the velocity values are also available at the grid points. The control volume for point P is represented as the gray square. The four faces (e, w, n and s) are represented by the dotted lines. The discretized continuity equation for the case shown in Figure 5–1 is given by

$$\frac{\rho^{k+1} - \rho^k}{\Delta t} \Delta x \Delta y = F_w + F_s - F_e - F_n$$

where F_e, F_w, F_n and F_s are the mass flow rates across the control volume faces and correspond to

$$F_e = (\rho u)_e \Delta y \qquad F_w = (\rho u)_w \Delta y$$

$$F_n = (\rho v)_n \Delta x \qquad F_s = (\rho v)_s \Delta x$$

5.3 Normalization

Since the grid used during the discretization is regular and the cells are cubic, it is customary to normalize the equations before discretization. The normalization is done in a similar way as it was done for the LBM. The characteristic length and time scale of the simulations are used. Choosing Δx as the characteristic length and Δt as the characteristic time gives $\Delta x = \Delta y = \Delta z = \Delta t = 1$. This approach simplifies the discretization significantly, for example the continuity equation is now written as

$$\rho^{k+1} - \rho^k = F_w + F_s - F_e - F_n$$

The notation used here is not strict, physical and dimensionless quantities are both expressed with the same symbol. This is done here to simplify the notation. From the rest of the chapter all quantities are dimensionless.

5.4 The Hybrid LBM-FVM

In this section, a new approach to integrate the LBM (MRT-LBM in chapter 4) and the FVM (section 5.1) is described. The hybrid LBM-FVM combines the LBM and the FVM into a single method to calculate the values of a scalar field subject to a time varying convection-diffusion conservation equation. The merge of these two methods is commonly referred in the literature as hybrid LBM methods, in this case the Hybrid LBM-FVM method. In the Hybrid LBM-FVM method discussed here the velocity field is calculated using the LBM, while the evolution of the scalar field is computed using the FVM method. The main properties of the method introduced here are: 1) satisfies continuity in the FVM grid, and 2) uses a single grid.

5.4.1 Problem Description

The FVM method requires the specification of diffusion and convection fluxes at the cell walls of the control volume. The diffusion fluxes are estimated using a geometric mean (see section 5.1), while the convection fluxes require the specification of the velocity and scalar fields at the interface. The value of the scalar field is determined by the convection-diffusion scheme selected, i.e. central differences in this case. In the classical FVM method (Patankar, 1980) the velocity field is calculated at the interface by using a staggered grid for the different velocity components. However, for the Hybrid LBM-FVM method the velocity field is calculated at the center of the control volume.

Figure 5–2 shows a 2D representation of the grids used in the LBM (left) and the FVM method (right). The LBM calculates the velocity field at the center of the control volume (u_P and v_P), while the FVM method requires the velocity field at the cell walls (u_e, u_w, v_n and v_s). Typically, grids for LBM and FVM are represented by connecting the grid points by lines. However, the explicit representation of the control volumes is preferred in this section; it will be useful in developing the Hybrid LBM-FVM method presented below.

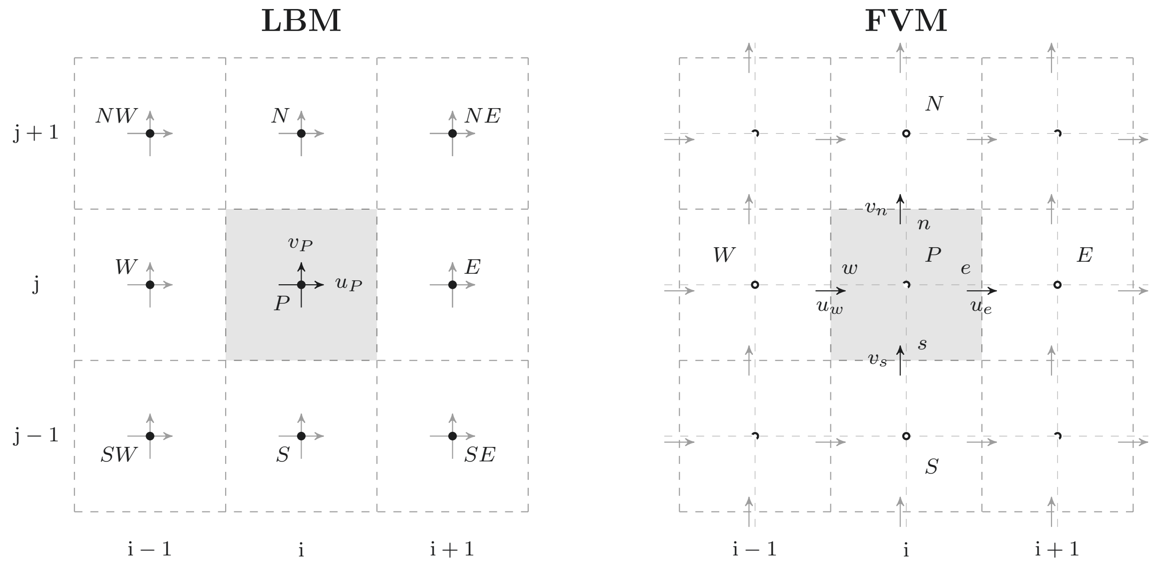

Figure 5–2: Comparison between 2D LBM and FVM velocity field locations.

A way to calculate the intercell velocities given the velocity field values at the center of the control volumes is needed. A detailed solution to this problem is presented in the remaining of this section.

5.4.2 Intercell Fluxes: Existing Approaches

The literature presented below can be divided in two subjects: a) the Finite Volume formulation of the LBM (FV-LBM) and b) the hybrid LBM. The references presented are not divided by subject because these two intersect in some cases; instead, the references are presented in non-strict chronological order.

Early developments on the Finite Volume formulation of the LBM (FV-LBM) were done by Benzi et al. (1992). The main objective of the FV-LBM is to extend the LBM to non-uniform grids. The problem with unstructured grids is that an inertial force term appears in the LB equation. This term reflects the change of direction of the particles during streaming. The first step in obtaining the FV-LBM is to use the Gauss theorem to express the LB equation in integral form over a control volume. The main problem with this formulation is that one depends on knowing the distributions at the volume surface. Therefore one would need to interpolate the node points to obtain these values. The interpolation method is not unique and controls the degree of accuracy of the method. However, the fact that the interpolation method is not unique is a concern.

The basic concepts of the volumetric formulation of the LBE are presented by Chen (1998). The approach is based on the work by Benzi et al. (1992), but it is introduced in a systematic way. Some difficulties with point-wise interpolation are discussed: a) detailed balance relations are lost and b) 3D interpolation is computationally intensive. In the FV-LBM formulation, instead of thinking that the distribution function belongs to a single mesh point, one can think of these distributions as averages over the entire cell.

Xi et al. (1999) presented the finite-volume formulation for the LBM (FV-LBM). Although different from the hybrid LBM family, some concepts are useful for the development of the hybrid approach. In particular, the authors present in detail an easy to implement FV-LBM. The method relies heavily on bilinear interpolation (in 2D) for estimating the distributions at the unknown locations.

A classical reference for LBM and Finite Difference (FD) method is the work of Lallemand and Luo (2003). The authors introduce the Hybrid Thermal Lattice Boltzmann Equation (HTLBE). Mass and momentum conservation equations are solved by using the MRT-LBM while the diffusion-convection equation for the temperature is solved separately using FD. One important argument presented is the need of a special stencil for the FD method when using the information from the LBM. The authors also highlight the fact that interpolations destroy local conservation laws and that they should be used with care.

Ubertini et al. (2003) present further developments on the FV-LBM formulation, referred to as Unstructured LBE technique. The authors show that ULBE tolerates significant stretching without introducing any appreciable numerical viscosity effect, which permits a time accurate description of transitional flows. The approach is similar to Peng et al. (1998), where the populations at the non-nodes are interpolated from the populations at the nodes.

Huang et al. (2007) use the FD-LBM for the study of axisymmetric flows. The hybrid approach presented in the study uses the 2D LBM to resolve the axial and radial velocities, while using FD for the azimuthal velocity and temperature.

Another use of the hybrid LBM-FVM-FDM was used by Mondal et al. (2008) to simulate a localized fire in a tunnel in 3D. In this work the fluid flow (density and velocity fields) is obtained form the LBM. The radiation term in the equation is solved using the FVM, while the temperature field (macroscopic energy equation) is calculated using the FDM (Finite Difference Method). The solution of the energy equation requires the information of the fluxes at the interfaces, thus the velocities. This problem is solved in their study by using the upwind scheme. Also, the control volume is staggered with respect to the LBM cell (Mondal and Mishra, 2009a,b)

Joshi et al. (2010) propose a hybrid FVM-LBM for compressible flows. In this method the inter-cell quantities are calculated using a LBM method for two different grids, one in each dimension, containing the inter-cell points. This approach is equivalent to the staggered grids in the classical FVM method. The main disadvantage of this approach becomes clear when dealing with 3D cases, because a second set of LBE need to be solved.

The use of Hybrid LBM has also been used for cases when the LBM and Finite Volumes (FV) are used on adjacent domains (Luan et al., 2012). In cases like this the coupling at the interfaces is very delicate, because the velocity distribution functions at the interfaces need to be obtained directly from the FV.

Although not presented as a hybrid approach, the FVM-LBM for irregular grids introduced by Zarghami et al. (2012) addresses the issue of calculating fluxes at the edges of a 2D control volume. The equations are presented for general irregular grids. Using these equations for regular fields reduces the algorithm to an average of neighbor distributions to obtain the distributions at the face. Velocities are then obtained from these distributions. The authors highlight stability issues with this approach and then correct the problem by using an upwind second order pressure biasing factors as flux correctors for the calculation of the inter-cell edges.

Huang et al. (2012) presented a hybrid LBM-FVM to simulate droplet motion under electrowetting control. The LBM is used to represent hydrodynamics, while the FVM is used for solving the evolution of the droplet interface. As most hybrid LBM methods, the fluxes at the boundaries are calculated as the averages of the values in two neighboring cells.

Recently, Li et al. (2014) presented a hybrid LBM-FVM applied to the study of natural convection. Two approaches are discussed for solving the problem with LBM velocities and the FVM faces being at different locations. The first approach is to interpolate the LBM velocities. The second approach is to use a coarser grid for the FVM. In this case the fluxes at the faces of the control volume are obtained directly from the LBM grid. Since the second approach is less computationally intensive, this method is preferred. However, the issue with mass conservation is not addressed in either approach.

In summary, the FV-LBM formulation provides methods to calculate fluxes at the interface. However, these methods do not satisfy conservation equations in the FVM grid. The case of hybrid LBM-FVM also addresses the issue of inter-cell fluxes, but the common approach is to use nearest neighbor interpolation. The details of mass conservation on the FVM grid and the problems with interpolation are discussed in detail in the next section.

5.4.3 Mass Balances for LBM and FVM

Simplified diagrams of the quantities used for mass balance calculations in the LBM and the FVM are presented in Figure 5–3. This figure introduces special indexation used in this section. The LBM distribution densities $\hat{f}_i$ indicate the post-collision distribution, while f_i represent pre-collision distributions, all for the grid point P (subscript omitted). Distributions on grid points other than P are indicated using a subscript, for example $f_{i,NE}$; these are not shown in Figure 5–3. Since the time step is taken during the streaming operation f_7^k corresponds to $\hat{f}_{7,NE}^{k+1}$, where k indicates the time step.

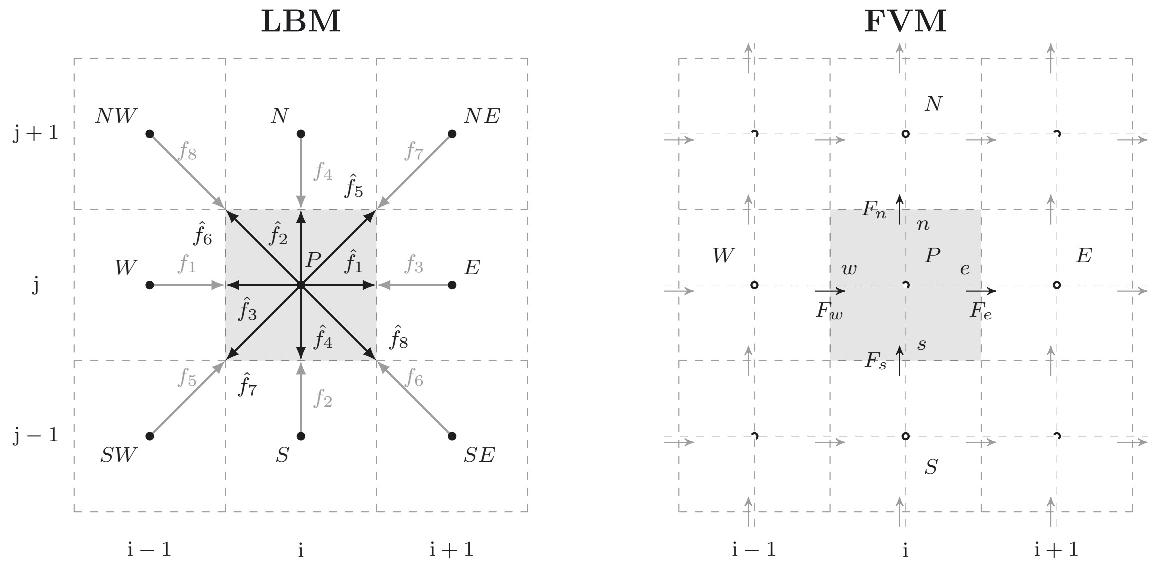

Figure 5–3: Quantities used in mass balance calculations for the LBM and FVM (2D).

In the case of the FVM the only information needed to calculate mass balances are the mass fluxes across the edges of the control volume (F_e, F_w, F_n, F_s) at time step

$k+1$ and the density for time steps k and $k+1$, ρ^k and ρ^{k+1}. To keep the notation compact, all geometric factors, Δx, Δy, and time step length, Δt, have been omitted in the derivations below. This is equivalent to starting the development from the normalized equations, where all these factors are equal to one.

Mass conservation is one of the main characteristic of the LBM. While oversimplifying, one could consider the streaming operation as the equivalent to the continuity equation, while momentum conservation is handled by the collision operator. Distribution functions only cross the control volume boundaries during streaming; while there is no material exchange between control volumes during collision.

LBM mass conservation characteristic is presented below as an exercise to help understand the need for a special procedure when developing the hybrid LBM-FVM. Starting from the integral form of the continuity equation

$$\frac{\partial}{\partial t}\int \rho \, dV + \oint \rho \vec{u} \cdot dS = 0 \tag{5.5}$$

the mass balances for the LBM can be described by

$$\rho^{k+1} - \hat{\rho}^k = \sum_{i=1} f_i^{k+1} - \sum_{i=1} \hat{f}_i^k$$

Using the definition of ρ (chapter 4) in terms of the distribution functions gives

$$\left(\sum_{i=1} f_i^{k+1} + f_0^{k+1}\right) - \left(\sum_{i=1} \hat{f}_i^k + \hat{f}_0^k\right) = \sum_{i=1} f_i^{k+1} - \sum_{i=1} \hat{f}_i^k \tag{5.6}$$

In Eq. (5.6), f_0^{k+1} and $\hat{f}_0^k$ are the same, because the streaming operator does not change the distributions. Therefore, the collision-streaming operations of the LBM satisfy the continuity equation.

In the case of the FVM expressing Eq. (5.5) in terms of the densities and velocities shown in Figure 5–3 gives:

$$\rho^{k+1} - \hat{\rho}^k = F_w + F_s - F_e - F_n \tag{5.7}$$

Expressing Eq. (5.7) in terms of the LBM distribution function requires defining the fluxes (F) at the inter-cell edges in terms of the distributions themselves. The typical approach taken in the literature is to interpolate the velocity field at the nearest neighbors.

$$F_e = \frac{\sum f_i^P c_i + \sum f_i^E c_i}{2} \tag{5.8}$$

Expanding the density variables in terms of distribution functions and replacing Eq. (5.8) into Eq. (5.7) gives

$$\sum_{i=5}^{8} f_i - \sum_{i=5}^{8} \hat{f}_i = \frac{\sum f_i^W c_i + \sum f_i^S c_i - \sum f_i^E c_i - \sum f_i^N c_i}{2} \tag{5.9}$$

The term $\sum_{i=5}^{8} \hat{f}_i$ corresponds to distribution functions streamed to the diagonal neighbors of the control volume P. These terms do not have a counterpart on the right-hand side of Eq. (5.9). Furthermore, some of the distributions on the right-hand side cannot be balanced by the remaining distribution on the left-hand side. Only in very specific situations the mass balance in Eq. (5.7) is satisfied. Therefore, the use of near-neighbor interpolation to determine the inter-cell flux gives values that do not satisfy mass balances in the FVM grid.

5.4.4 Inter-Cell Flux Calculation

The main objective of this section is to develop a systematic way of calculating inter-cell fluxes from LBM distribution functions, that satisfy continuity in the FVM grid Eq. (5.7).

One of the main problems identified in subsection 5.4.3 is the presence of diagonal distributions that cannot be cancelled out in the FVM continuity equation. This problem appears because the mass fluxes in the FVM only pass to adjacent cells and not to the diagonal ones. This development starts by proposing the interpretation of diagonal distribution functions shown in Figure 5–4.

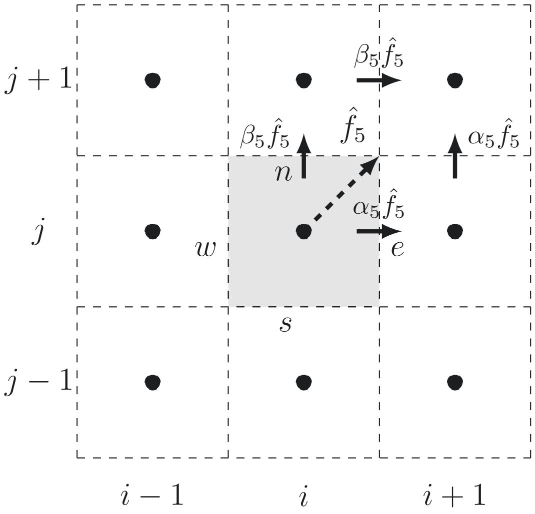

Figure 5–4: Decomposition of diagonal distributions. Example: D2Q9 component $\hat{f}_5$

This interpretation is compatible with FVM discretization of the continuity equation because the diagonal components are decomposed in two contributing mass fluxes that are aligned with the existing fluxes in the FVM. Only the case for $\hat{f}_5$ is presented, all other distributions follow the same approach.

The weights α and β have been added to indicate that diagonal component do not contribute mass to the direct neighbors, they only contribute to the diagonal neighbors. In the case of the north edge the contribution to N is subtracted as a contribution from N to NE. Furthermore, the constraint $\alpha + \beta = 1$ ensures that $\hat{f}_5$ is transferred completely from P to NE during streaming, in the FVM sense.

The values of α and β are selected based on the geometry. Since the grid is uniform, all diagonal components are assumed to contribute equally to the adjacent edges. Therefore the values of $\alpha = \beta = 1/2$ is used in the rest of the development.

The mass fluxes at each edge of the control volume are calculated as the sum of all distribution crossing the edge during streaming. The distributions used in the calculation of the east wall flux, F_e, are represented in Figure 5–5 (left). The indexes for all distributions have been left out to facilitate readability of the figure.

Ten distribution functions are needed in the calculation of F_e in the 2D case. The equation to calculate F_e for the 3D case, shown in Figure 5–5, is given by Eq. (5.10). However, for the rest of the F components the corresponding figures can be considered graphical equations. The flux can be calculated as the sum of

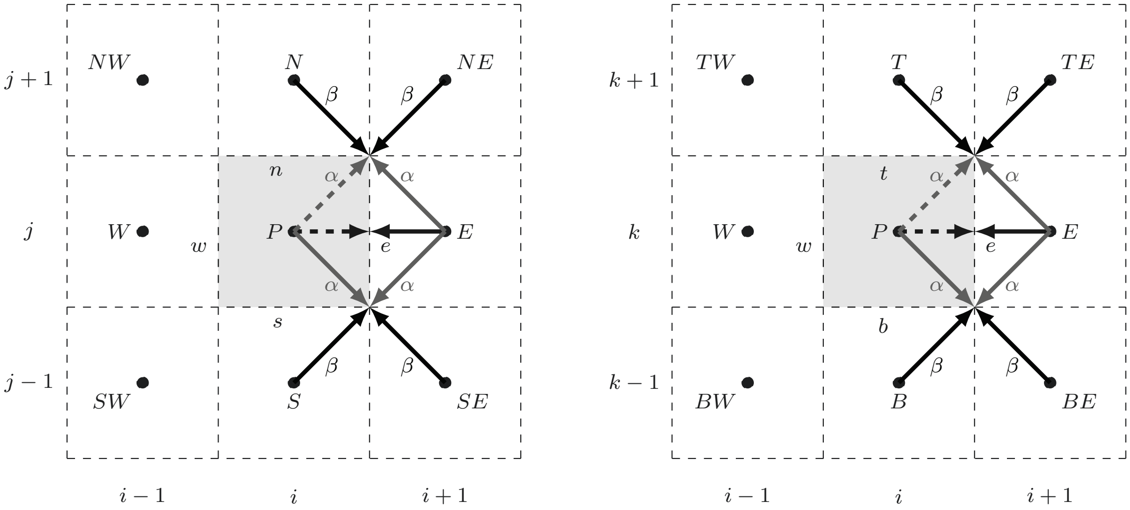

Figure 5–5: Distributions needed for calculating F_e for D3Q19.

all components in the figure, multiplied by the normal vector of the edge or face in question. For Figure 5–5 the equation is:

$$F_e = f_1 + \frac{f_5}{2} + \frac{f_8}{2} + \frac{f_{8,N}}{2} + \frac{f_{5,S}}{2} - f_{3,E} - \frac{f_{6,E}}{2} - \frac{f_{7,E}}{2} - \frac{f_{7,NE}}{2} - \frac{f_{6,SE}}{2} \tag{5.10}$$

This approach can be directly extended to the case of LBM D3Q19. The equations for fluxes on all faces are presented in Figures 5–5 to 5–7. Only the east, north and top components are shown. The other components are calculated as part of the adjacent control volumes.

This approach gives conservative mass fluxes at the control volume faces, which are required by the FVM, i.e. Eq. (5.7) is satisfied. If the velocities at the faces of the control volume are needed, an estimation of the density at the interface would be required.

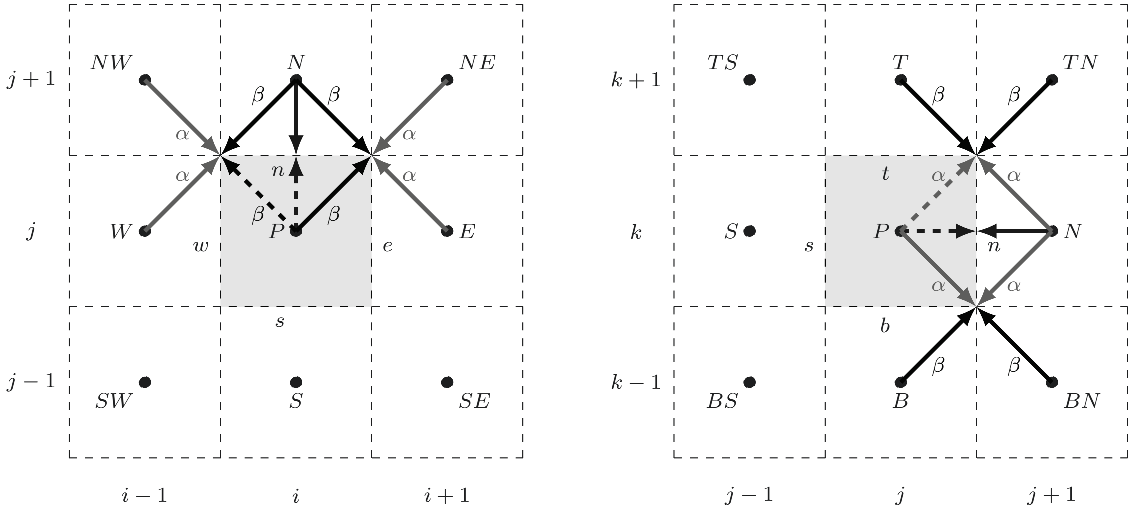

Figure 5–6: Distributions needed for calculating F_n for D3Q19.

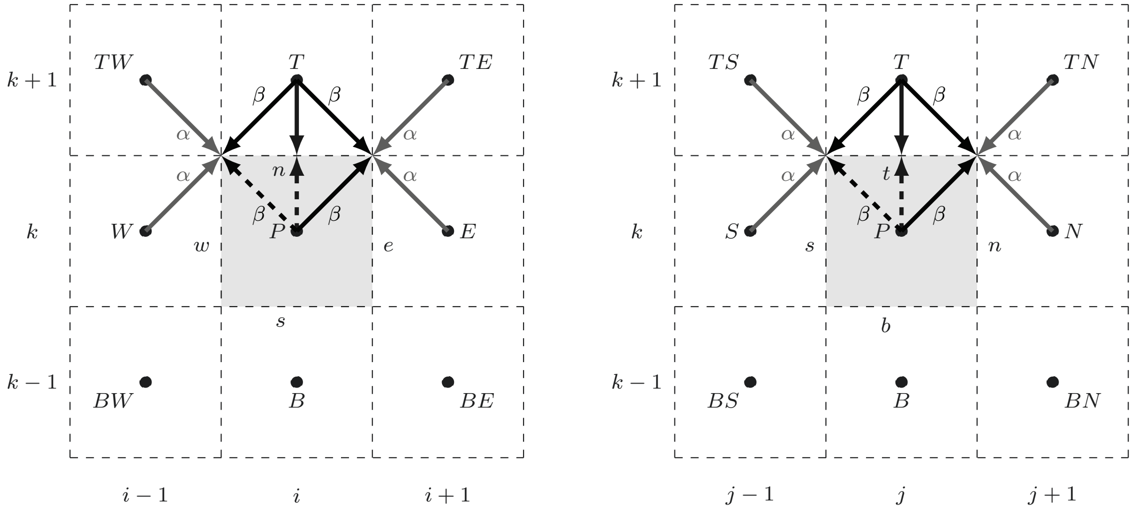

Figure 5–7: Distributions needed for calculating F_t for D3Q19.

Chapter 6
Estimation of Effective Diffusivities

Two methods for calculating effective diffusivities (effective thermal conductivity or effective mass diffusion coefficient) from their respective scalar fields (temperature and concentration) are presented in this chapter. The first step to calculate the effective diffusivity is to define a macroscopic view of the system. For the case of nanofluids the macroscopic view is an homogeneous fluid at rest. Initial and boundary conditions for the microscopic system are then set depending on the characteristics of the macroscopic model selected.

6.1 Fixed Gradient Method

6.1.1 Macroscopic Model

In this method it is assumed that the macroscopic system follows Fourier's law of heat conduction. The case of mass transfer will be discussed later. Furthermore, the dimensionality is decreased to a 1D system, thus giving the following form of Fourier's law:

$$\hat{q}_x = -\lambda_{\text{eff}}(\nabla_x T)$$

This macroscopic view of the system imposes the boundary conditions on the microscopic model. However, two options are available in this case: a) fixed gradient or b) fixed flux q_x. As indicated by the name of the model, the fixed gradient was chosen. In this case, the gradient in the x direction is set by fixing the temperatures on the west and east boundaries (Dirichlet type) and maintaining all other boundaries as periodic. Then, the only quantity needed to estimate the effective thermal conductivity is the effective flux across the domain.

$$\lambda_{\text{eff}} = -\frac{\hat{q}_x}{\nabla_x T} \tag{6.1}$$

The effective flux across the domain is calculated by averaging the conductive flux for the entire east and west boundaries over time. Although the instantaneous convective flux is not zero, the expected value of the average velocity is zero, thus giving a zero average convective flux. Therefore, the convective flux is not considered in the calculation of the effective thermal conductivity.

Figure 6–1 shows a simplified representation of the fixed gradient method for the case of heat transfer. The macroscopic view (left) is governed by heat conduction across an homogeneous substance. A fixed temperature gradient (dT/dx) is applied by setting the boundaries to prescribed temperatures, T_h and T_c. The temperature gradient is also represented by isotherms. The microscopic system (right) is simulated with the same temperature gradient. Then, the effective heat flux ($\hat{q}_x$) is calculated from the microscopic temperature field. The effective thermal conductivity is given by minus the ratio of the calculated effective flux and temperature gradient imposed Eq. (6.1). The presence of particles and variations in the flow field (micro-convection currents) would deform the isotherms at the microscopic level.

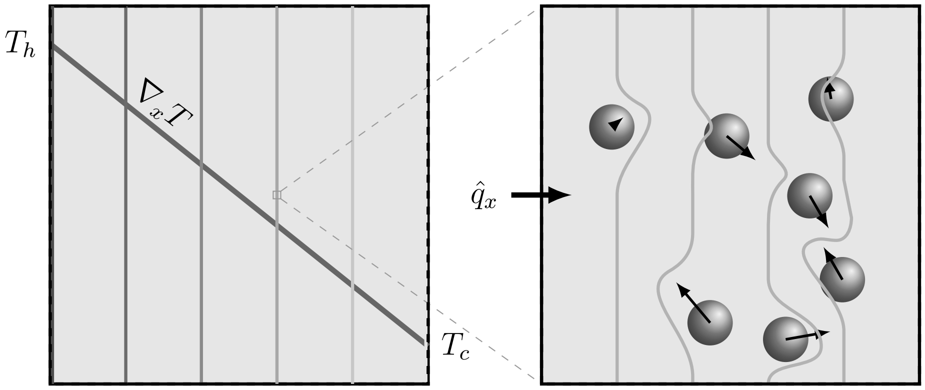

Figure 6–1: Representation of the macroscopic (left) and microscopic (right) views of the fixed gradient method.

6.1.2 Boundary and Initial Conditions

The macroscopic model imposes the boundary conditions, in this case the east and west boundary are Dirichlet type, where the temperatures are set to values to obtain the prescribed gradient. However, the macroscopic model does not impose any restriction on the initial conditions of the system, only that the averaging should only be done after all transients have died out.

Determining the time for the transients to die out is possible for the study of composite materials, were the temperature field achieves a final form and does not change over time. However, for the case of nanofluids the temperature field is continuously changing and a “steady state” is impossible to determine. An approximation is to use the solution when the average temperature of the system oscillates around a point.

The temperature field was initialized with the steady state solution with the particles at rest. This is the solution for the equivalent composite material case. This initial condition was selected because the transients are very long, and starting the system from a known solution decreases the time needed to achieve the equivalent "steady state".

Validation of this method was done by comparing with the theoretical equation by Maxwell (1892). The procedure is presented as one of the applications in Part III, chapter 7.

6.1.3 Extension to Mass Transfer

The fixed gradient method can also be used to study mass transfer in nanofluids. In this case the macroscopic equation is given by Fick's law. The macroscopic view assumes an homogeneous, single phase fluid with effective mass diffusivity D_{eff}, where diffusion across a fixed concentration gradient is governed by:

$$\hat{J}_x = -D_{\text{eff}} \nabla_x c_A \tag{6.2}$$

Once again, the average flux across the boundaries, $\hat{J}_x$, is calculated from the time average of the diffusive fluxes from the microscopic concentration field. Similar to the heat transfer case, the boundary conditions set for the microscopic model are Dirichlet type on the east and west walls, thus forcing a prescribed gradient, $\nabla_x c_A$.

6.1.4 Limitations of the Fixed Gradient Method

One of the main disadvantages of the fixed gradient method is that variations in the center of the domain have to propagate to the boundaries before changes in the effective diffusivities can be observed. The large thermal diffusivity for the systems studied make this method viable for heat transfer studies. However, in the case of mass transfer, the diffusivity is comparatively 100 to 10000 times smaller. The increase in computation time required for the mass transfer simulations is of the same order, thus making mass transfer simulations via fixed gradient method unattractive.

Another issue that affects both, heat and mass transfer simulations, is the loss of periodicity when applying the Dirichlet type boundary conditions. It is possible to recover the periodicity by placing an internal boundary condition (through the use of a sink), where the temperature decreases from the west wall to the center of the domain to follow a prescribed gradient (He and Qiao, 2008). The same is done for the east wall, thus recovering the periodicity of the system. In this case the east and west wall are at the same temperature, thus giving a periodic system. However, comparison of both types of boundary conditions show no significant difference in the study of heat transfer in nanofluids. Therefore, the boundary conditions described in subsection 6.1.2 were used. An alternative method inspired on conserving periodicity is presented in the next section.

6.2 Gaussian Pulse Method

Two of the main disadvantages of the fixed gradient method developed in the previous section are: a) the loss of periodicity with the imposed gradient, and b) the need for very long simulations in the case of mass transfer. The approach in this section is designed to overcome these two difficulties, thus providing a way to study mass diffusion in nanofluids.

6.2.1 Macroscopic Model

The 1D diffusion of a drop of dye would normally give a spreading Gaussian concentration profile over time. The diffusion coefficient is related to the mean square displacement of the solute molecules, which, for a Gaussian distribution can be obtained from the time evolution of the standard deviation (Culbertson et al., 2002; Krishnamurthy et al., 2006; Fang et al., 2009)

$$\langle (\Delta x)^2 \rangle = \sigma^2 = 2D_\mathrm{m} t \tag{6.3}$$

The 2D and 3D diffusion cases are similar but the coefficient of 2 in Eq. (6.3) depends on the dimensionality of the problem. The concentration profile for each case are:

$$\begin{aligned}
&\text{1D}: \quad c_A(x,t) = N\frac{1}{(4\pi D_\mathrm{m} t)^{1/2}} e^{-x^2/4D_\mathrm{m} t} \qquad \langle x^2 \rangle = \int_{-\infty}^{\infty} x^2\; c_A(x)\; dx = 2D_\mathrm{m} t \qquad (6.4)\\
&\text{2D}: \quad c_A(\rho,t) = N\frac{1}{(4\pi D_\mathrm{m} t)^{1}} e^{-\rho^2/2D_\mathrm{m} t} \qquad \langle \rho^2 \rangle = \int_{0}^{\infty} \rho^2\; c_A(\rho)\; d\rho = 4D_\mathrm{m} t\\
&\text{3D}: \quad c_A(r,t) = N\frac{1}{(4\pi D_\mathrm{m} t)^{3/2}} e^{-r^2/4D_\mathrm{m} t} \qquad \langle r^2 \rangle = \int_{0}^{\infty} r^2\; c_A(r)\; dr = 6D_\mathrm{m} t
\end{aligned}$$

This particular characteristic is used here to develop a procedure to estimate effective diffusion coefficients. Similar to the method employed to estimate Taylor diffusion in tubes (Taylor, 1953), the idea is to follow the evolution of a Gaussian concentration profile over time and use this information to estimate the effective mass diffusion coefficient.

The macroscopic system is represented by a purely diffusive process, where the convection fluid velocity is zero and the effective diffusion coefficient D_{eff} is constant. In the present case the macroscopic model is given by following conservation equation and boundary conditions:

$$\frac{\partial}{\partial t}c_A = D_{\text{eff}}\frac{\partial^2}{\partial x^2}c_A, \qquad c_A(x,0) = c_A^0 \text{ and } \ c_A(\pm\infty, t) = 0 \tag{6.5}$$

Where the boundary conditions enforce zero concentration at $\pm\infty$, a limitation for numerical implementation discussed below. The initial condition c_A^0 is given by Eq. (6.6). This choices helps to avoid initial transients associated to a square pulse initial conditions.

$$c_A^0(x) = \frac{1}{\sigma_0\sqrt{2\pi}}e^{-(x-x_0)^2/2\sigma_0^2} \tag{6.6}$$

where σ_0 is selected such that the pulse is contained within the computational domain. The pulse location, x_0, is placed in the center of the domain. This constraint on the pulse location is not necessary and will be discussed in the study of composite materials in subsection 6.2.5. A graphical representation of Eq. (6.6) for different values of the initial spread, σ_0, on a typical simulation domain is presented in Figure 6–2.

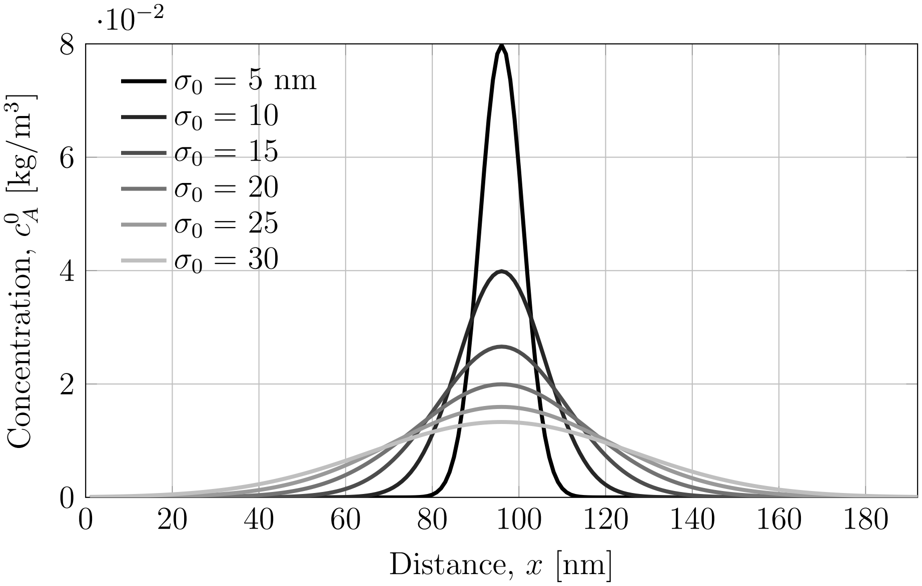

Figure 6–2: Concentration profiles for different initial standard deviations σ_0. Legend is the standard deviation σ_0 in nanometers.

As indicated before, one of the main limitations is the finite domain simulated. The initial concentration profile needs to decay quickly to zero, that way the presence of periodic boundary conditions will not affect the results. Figure 6–2 suggests a maximum initial standard deviation of 25 nm to avoid pulse interaction with the boundaries. This settings give concentration in the order of 1×10^{-5} at the boundaries.

The curves in Figure 6–2 can also be interpreted as the evolution of the concentration field over time. Note that Eq. (6.6) can be obtained from Eq. (6.4) by replacing σ_0^2 by $2D_\mathrm{m}t$ and setting $x_0 = 0$. Therefore, the curves in Figure 6–2 also represent solutions at $t = \sigma_0^2/2D_\mathrm{m}$.

6.2.2 Effective Diffusion Coefficient

The standard deviation of the Gaussian pulse can be calculated from the moments of the concentration profile. The n^{th} moment about a point x^* of a real value function $f(x)$ is given by:

$$M_n = \int_{-\infty}^{\infty} (x - x^*)^n \, f(x) dx$$

For a Gaussian distribution only the zeroth, first and second moments are relevant. In particular, the variance of the distribution is given by the second moment about the mean value or first moment.

$$\sigma^2 = M_2 = \int_{-\infty}^{\infty} (x - M_1)^2 \, f(x) \, dx$$

By defining the raw moments with primed letters, given by:

$$\begin{aligned} M_0' &= \int_{-\infty}^{\infty} c_A(x) \, dx \qquad (6.7) \\ M_1' &= \int_{-\infty}^{\infty} x \, c_A(x) \, dx \\ M_2' &= \int_{-\infty}^{\infty} x^2 \, c_A(x) \, dx \end{aligned}$$

then, the central moments for normalized concentration profile

$$f(x) = \frac{c_A(x)}{M_0'} = \frac{c_A(x)}{\int_{-\infty}^{\infty} c_A(x) \, dx}$$

are given by

$$M_0 = \frac{M_0'}{M_0'} = 1 \tag{6.8}$$

$$M_1 = \frac{M_1'}{M_0'} \tag{6.9}$$

$$M_2 = \frac{M_2'}{M_0'} - \left(\frac{M_1'}{M_0'}\right)^2 \tag{6.10}$$

The zeroth moment in Eq. (6.8) is of no importance because it is always one. However, the zeroth raw moment in Eq. (6.7) corresponds to the overall conservation of species, and it gives the total mass of component A inside the domain. This value should be constant over the length of the simulations.

The first moment as given by Eq. (6.9) is not strictly a central moment, instead it represents the position of the average value or center of the pulse. The time derivative of this moment would give the average velocity of the fluid. Since the overall fluid velocity is zero, this moment should be constant and equal to the center of the initial Gaussian pulse.

The second moment given by Eq. (6.10) represents the standard deviation of the pulse. The effective diffusion coefficient is calculated from the slope (m) of M_2 vs. t by:

$$D_{\text{eff}} = \frac{m}{2} \tag{6.11}$$

So far, the calculations have been done on the one dimensional concentration profiles. However, the field obtained from the calculations in chapter 5 varies in the three dimensions. The 1D concentration profiles $c_A(x)$ is obtained from the concentration field by averaging over the y and z directions:

$$c_A(x) = \frac{\int c_A(x,y,z)\,dy\,dz}{\int dy\,dz}$$

Typical curves for the evolution of the standard deviation over time are shown in Figure 6–3. This figure shows the evolution of the second moment for: a) homogeneous materials, b) composite materials and c) nanofluids. The cases presented here correspond to mass transfer simulations, where the mass diffusivity inside the particles was set to zero. The effective coefficient is estimated from the slope of the curve.

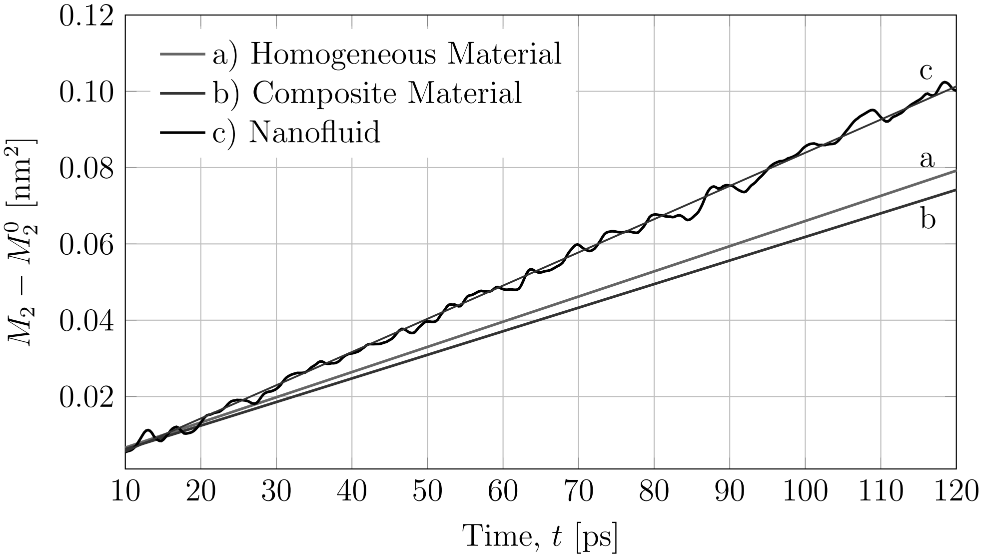

Figure 6–3: Typical evolution of the second moment over time for: a) homogeneous fluid, b) composite material and c) nanofluid (2nm Al_2O_3-Water at 295 K).

The slope of the curve is obtained by linear regression. Only the regression line for the nanofluids case is presented in Figure 6–3. The other two cases are indistinguishable from the regression lines. The characteristics of these lines will be discussed in more detail in chapter 7 and chapter 9.

6.2.3 Extension to Heat Transfer

This approach is also applicable to heat transfer. However, the macroscopic conservation of energy for a purely diffusive process is give by:

$$\frac{\partial T}{\partial t} = \frac{\lambda_{\text{eff}}}{(\rho\, c_P)_{\text{eff}}} \frac{\partial^2 T}{\partial x^2} = \alpha_{\text{eff}} \frac{\partial^2 T}{\partial x^2}$$

Here, the effective thermal diffusivity α_{eff} has been replaced by the effective thermal conductivity divided by the effective volumetric heat capacity.

Since we are interested in the thermal conductivity, the effective thermal conductivity can be calculated from the slope (m) of the M_2 vs. t curve:

$$\lambda_{\text{eff}} = \frac{m}{2} (\rho\, c_P)_{\text{eff}}$$

The extra term $(\rho\, c_P)_{\text{eff}}$ is then calculated as (Nomura and Chou, 1986):

$$(\rho\, c_P)_{\text{eff}} = \phi(\rho\, c_P)_{\text{p}} + (1 - \phi)(\rho\, c_P)_{\text{f}}$$

6.2.4 Taylor Dispersion: Parallel Plates

Validation of the Gaussian pulse method was done in two parts. First, the method was validated against composite materials, where the particle and fluid are static. This is discussed in details in chapter 7. The second validation introduces fluid motion. In this case the objective is to simulate diffusion of a solute in a normal fluid in the presence of a velocity gradient between two parallel plates. Two cases are considered: a) Couette flow and b) Plane Poiseuille flow. The effective diffusion coefficient for both cases are known results of the general Taylor dispersion theory (Mazo, 2002):

$$\frac{D_{\text{eff}}}{D_{\text{m}}} = 1 + \frac{Pe^2}{30} \qquad \text{Couette flow} \tag{6.12}$$

$$\frac{D_{\text{eff}}}{D_{\text{m}}} = 1 + \frac{Pe^2}{210} \qquad \text{Plane Poiseuille flow} \tag{6.13}$$

The results from the simulations are compared to the theoretical calculations using equations Eq. (6.12) and Eq. (6.13), and these are presented as a function of the Péclet number in Figure 6–4. In Figure 6–4 the simulation results are represented by the symbols, while the theoretical equations are shown as solid lines. It is clear that the simulations reproduce the theoretical behavior.

The central difference scheme used in the FVM is limited to small cell Péclet numbers (Patankar, 1980). In the particular case of Taylor dispersion for parallel plates simulated here, the constraint is translated into a small time step requirement. Other methods that can allow larger time steps exist (Boris, 2013), however, for the

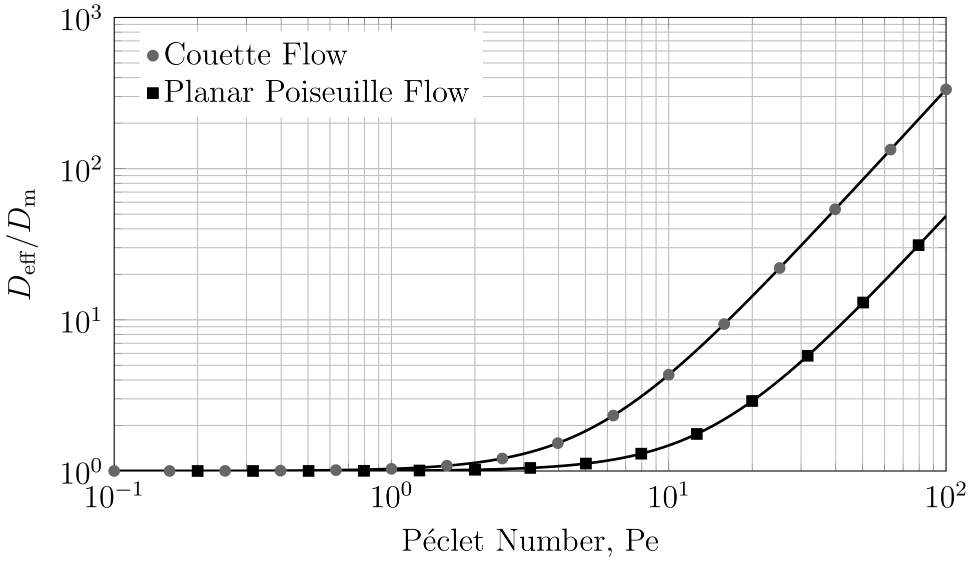

Figure 6–4: Normalized effective diffusion coefficient as a function of Péclet number for Couette and planar Poiseuille flows. Solid symbols indicate simulations results, and the solid lines represent theoretical calculations using Eq. (6.12) and Eq. (6.13).

case of nanofluids, the small time step constraint is already imposed by the fLBM step.

6.2.5 Heterogeneous Systems: Solid Particles

The method developed above can be used to estimate the effective diffusivities of homogeneous systems, as shown for the cases of Taylor dispersion for Couette and planar Poiseuille flows between parallel plates. However, when solid particles are included in the simulations additional factors need to be considered.

Figure 6–5 shows a typical computational domain along with an initial Gaussian pulse placed in the center of the domain (left). Even though, particles are evenly distributed across the entire domain, when the Gaussian pulse is placed in the center of the domain, it would only sample a portion of the domain. For example, in the extreme case where a single particle is placed near the east boundary, the center pulse would not sample the effect of this particle correctly, and the effective diffusivity would be close to the value of the fluid. If the particle is placed in the center of the domain, the calculated effective diffusivity would be closer to the theoretical value for composite materials.

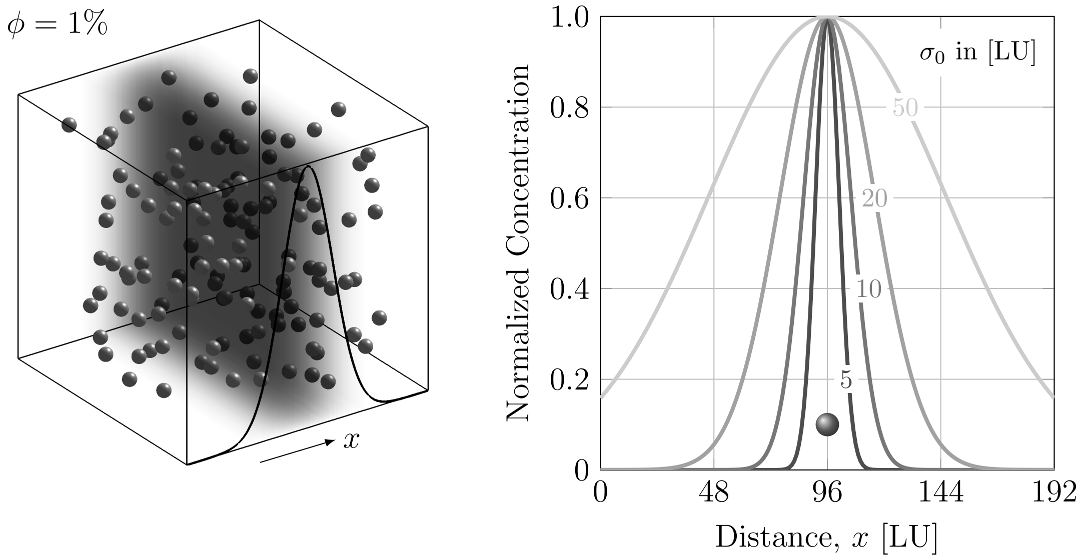

Figure 6–5: Left: computational domain and initial Gaussian pulse; darker indicates higher concentration. Right: comparison of particle size with initial Gaussian pulses with different σ_0 (legend).

Figure 6–5 also shows a comparison of possible initial Gaussian pulses with a typical particle placed in the center of the domain. An additional constraint when simulating domains with particles is that the size of the inclusion should be smaller than the size of the pulse used. If larger domains could be simulated this restriction would disappear. However, at the moment it is impractical to simulate much larger domains, therefore another solution is needed.

Tests were conducted with different pulse widths and particle sizes. The tests were performed on the simulation of composite materials, where a theoretical result is available for comparison. It was determined that the standard deviation of the initial Gaussian pulse should be at least the diameter of the particles for the results to be consistent with theory. More details on the simulation of composite materials are given in chapter 7.

Instead of simulating larger domains, the macroscopic or effective diffusivities are obtained by averaging samples from the entire domain. This is done by placing the Gaussian pulse at different initial locations, as depicted in Figure 6–6 (left). An infinite number of pulses would be ideal, however this approach would be impractical. Instead, for a typical domain of 192 lattice cells across, four pulses of $\sigma_0 = 20$ LU are used at four equidistant locations.

The evolution of the Gaussian pulse variance over time is shown in Figure 6–6 (right). The thin lines represent the results obtained for each of the pulses. The thick line is the average from all four pulses. The expected monotonic increase over time is observed for the average. This average line is then used for the calculation of the effective diffusivity for the domain.

Note that the initial pulse also respects the periodic boundary conditions imposed. In Figure 6–6 the pulses that cross one of the boundaries continue in the opposite

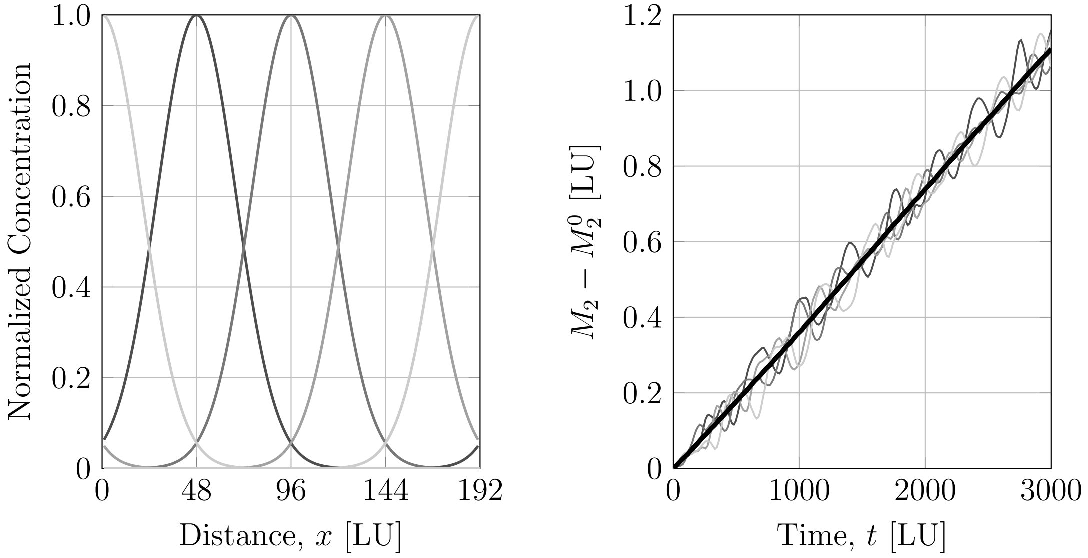

Figure 6–6: Left: representation of four pulses used in the simulations. Corresponding shades of gray indicate a single pulse. Right: time evolution of the second moment for each initial pulse (thin lines). The thick line represents the average of the four curves.

boundary. This is equivalent to having a train of pulses separated by a distance equal to the size of the domain. Each pulse is simulated individually, while assuming it does not interact with neighboring pulses. This assumption places a limit on the size of the pulse that can be used and on the maximum variance that can be simulated. A good value for the initial pulse width is to make σ_0 one tenth of the total domain.

The main disadvantage of this method compared to the fixed gradient method is that the macroscopic view is somehow lost, because the the Gaussian pulse width has to be smaller than the dimensions of the computational domain. Therefore, Gaussian pulse method requires larger domains than the fixed gradient method.

The modular characteristic of the mathematical model proposed facilitates the calculations of the four pulses for the same domain. In this case the particle motion is calculated for a set of initial particle positions (fLBM). Forces and torques are then stored in a file, which is used for the four Gaussian pulses simulated. This way, the motion of the particles is the same for all four simulations, plus, the simulations can be executed at the same time since they are independent from each other.

In summary, when studying systems with particles four independent pulses are simulated. The effective diffusion coefficient is calculated from the average evolution of the second moment over time. Validation of this approach is presented separately in chapter 7.

Part III

Applications

Chapter 7
Composite Materials

In this chapter, the fixed gradient method and the Gaussian pulse method introduced in the previous chapter are used to estimate the effective thermal conductivity and diffusion coefficient in composite materials. Although, the analysis is presented as an application, the main objective is to validate the methods.

One of the main particularities of composite materials, in terms of the simulation methods used here, is that the particles and fluid are static (i.e. velocity field). In this case the LBM is no longer needed and only the FVM is used to determine the effective heat and mass diffusivities.

The results from numerical experiments are compared to theoretical values for composite materials. The theoretical model used for comparison is Maxwell's equation for composite materials (Maxwell, 1892).

7.1 Fixed Gradient Method Application to Heat Conduction

The fixed gradient method has the particularity that, during the first time step of the simulation, the composite material case is solved. This is achieved by setting the velocity field to zero everywhere and solving the steady state heat conduction equation. Switching from transient to steady state solution can be done by setting the time step in the discretization to a very large value.

Simulations with different particle thermal conductivities, different particle volume fractions and with randomly placed spherical particles were conducted. The thermal conductivity of the host medium was $\lambda_\mathrm{f} = 0.58$ W/(m K). The results from these simulations are shown in Figure 7–1. The symbols in this figure represent the simulation results, while the lines represent Maxwell's equation at the corresponding particle thermal conductivity.

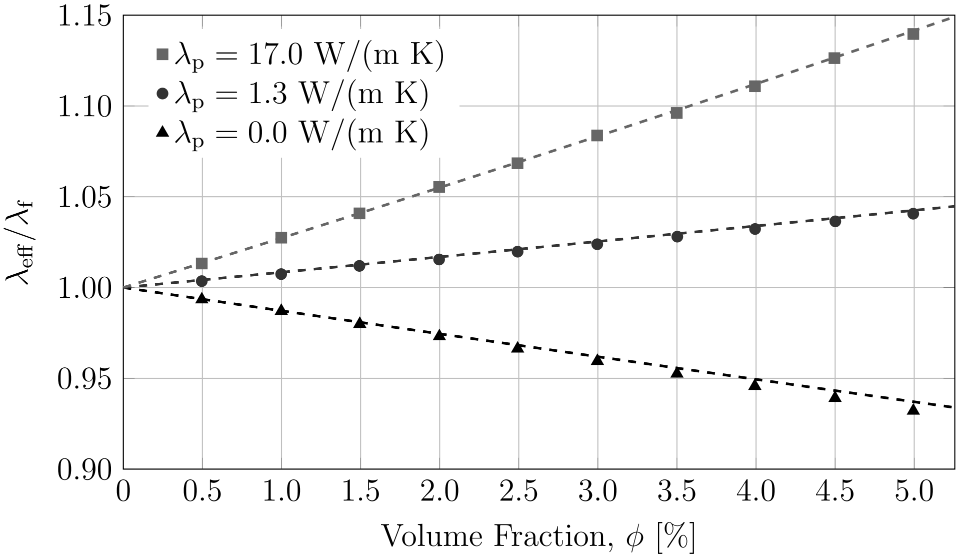

Figure 7–1: Normalized effective thermal conductivity vs. particle volume fraction for composite materials using the fixed gradient method. Numerical experiments represented by the symbols, and Maxwell's equation at corresponding λ_p indicated by dashed lines.

The case of zero particle thermal conductivity is an alternative representation for mass transfer studies. In the case of mass transfer, the particles are considered to be impermeable to the solute. In terms of heat transfer, impermeable particles correspond to perfect insulator particles, (i.e. no conductivity).

The simulation results showed in Figure 7–1 indicate the fixed gradient method can be used for estimation of effective heat and mass diffusivities in composite materials with spherical inclusions.

Cases with higher particle thermal conductivities were also considered. Values up to $\lambda_\mathrm{p} = 400$ W/(m K) were simulated (e.g. Cu particles). These are not included in the figure because they are very close to the value obtained for $\lambda_\mathrm{p} = 17$ W/(m K) (e.g. CuO particles). Additionally, not all simulations for higher thermal conductivity were completed. Problems with jumping coefficients in thermal conductivity, from the fluid phase to the particle phase, slow down the iterative solver in the FVM, making this approach unattractive for cases where the ratio of thermal conductivities, particle-to-fluid, is larger than 100.

Although, the fixed gradient method can be used to estimate the effective mass diffusion coefficient of composite materials, its extension to nanofluids is not practical because a large number of time steps are required (section 6.1). The case of composite materials is different because the system is solved at steady state. This implies that only a single cycle of the FVM is executed. Results from these simulations are equivalent to the zero thermal conductivity values shown in Figure 7–1.

7.2 Gaussian Pulse Method

7.2.1 Modifications for Composite Materials

The method to estimate effective coefficients for composite materials is more complicated than for homogeneous materials discussed in the previous chapter. For homogeneous materials the evolution of the second moment over time has a single slope; it only decreases when the Gaussian profile starts to interact with the periodic boundaries. The diffusion coefficient for the material in question can be calculated from the value of the slope. In the case of homogeneous materials this process does not give any extra information, because the diffusion coefficient is known and is part of the input parameters for the numerical experiments.

For composite materials the effective heat or mass diffusion coefficient is unknown. The objective is to calculate the coefficient from the evolution of the second moment over time, more precisely, from the slope. However, for composite materials the slope changes over time.

An example of these changes is shown in Figure 7–2. This particular case corresponds to particles with $\lambda_{\mathrm{p}} = 1.3$ W/(m K) in water with $\lambda_{\mathrm{f}} = 0.58$ W/(m K). The absolute size of the particles is irrelevant for composite materials, but the dimensionless size is important for the numerical simulations; Figure 7–2 shows the results for simulations with particles 5 LU in diameter and a particle volume fraction of 0.5%. The dark line in Figure 7–2 corresponds to the normalized effective thermal conductivity. This value is proportional to the slope of the second moment over time.

The light gray line in Figure 7–2 corresponds to the change in the slope over time. The line is presented in arbitrary units (A.U.) because the absolute value of this curve is irrelevant for the analysis. Similarly, the time axis is in lattice units or time steps.

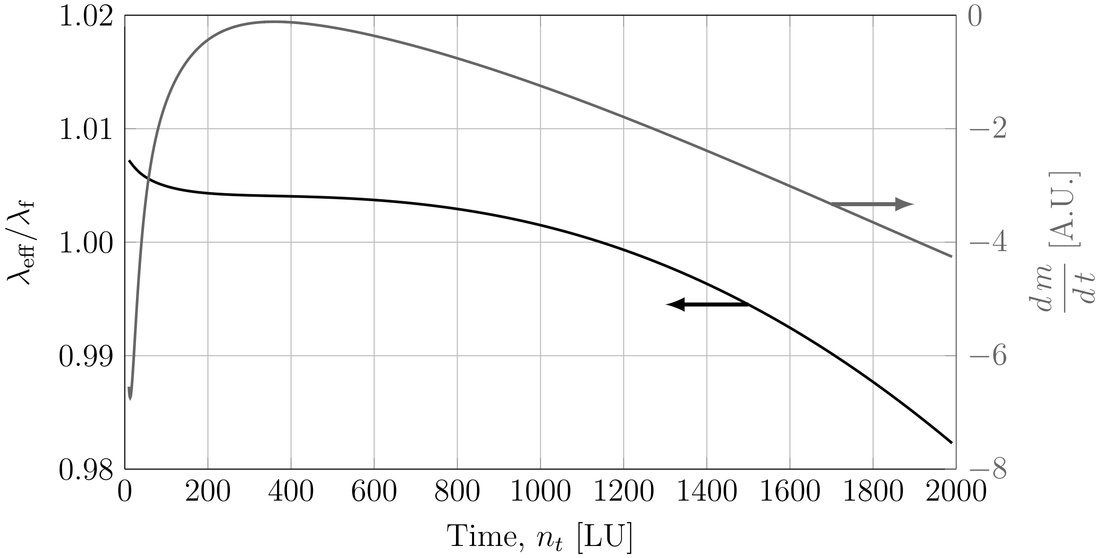

Figure 7–2: Time evolution of the normalized effective thermal conductivity and time derivative of the slope used in the calculation of the thermal conductivity for composite materials.

For composite materials the initial slope changes very quickly, then settles or plateas. Finally, this is followed by decreasing even further, as shown in Figure 7–2. This is characteristic of all simulations for composite materials performed. Three zones were identified and named as follows:

1. Transient to Pseudo-Gaussian: the decrease in slope happens because the diffusion of a composite material is not of Fourier type. The presence of the particles disrupt the imposed Gaussian profile. This could be considered as a transient to pseudo-Gaussian profile, one that accounts for the presence of the inclusions.
2. Plateau: once the pseudo-Gaussian profile is reached the slope stops changing. The evolution of this profile over time would behave as a macroscopic homogeneous material, thus giving the plateau region. The plateau region is characterized by a slow changing slope. Although this region is poorly represented in Figure 7–2, it is useful for estimating the effective thermal conductivity, as indicated below.
3. Pulse interaction: the final zone exists as part of the size of the domain. The further decrease in the slope is related to the interaction of pulses because of the periodic boundary conditions imposed. This also occurs for simulations with homogeneous materials.

The light gray line in Figure 7–2 indicates the presence of a maximum point. If the computational domain was infinite, pulses would not interact and the change in slope would reach the value of zero, the inflection point. However, since the Gaussian pulses always interact in a finite domain, the value used for estimating the effective thermal conductivity is when the change in the slope is at its maximum. Note that this corresponds to small slope changes, since the slope is always negative, the maximum corresponds to values close to zero change in the slope, the plateau region.

This analysis highlights one important limitation of the Gaussian pulse method. Simulations using the Gaussian pulse method have to be long (in time) enough to overcome the initial transient, but not too long that Gaussian pulse interaction would bias the results. The selection of the pulse width discussed in subsection 6.2.5 was done because of this constraint. Furthermore, it was observed that the pulse width (standard deviation of the Gaussian profile) should be at least the same size as the particle diameter in the simulations.

Another option considered was to compare the dynamic response at longer times, that is, including Gaussian pulse interactions. This would give a better estimate of the steady state value. However, since using the inflection point gives similar results, it does not justify the longer simulations.

7.2.2 Heat Transfer

The method described above was used to estimate the effective thermal conductivity of composite materials. Two different particle thermal conductivities were simulated, SiO_2 with $\lambda_p = 1.3$ W/(m K) and Cu with $\lambda_p = 400$ W/(m K). Particles were evenly distributed across the computational domain, simple or primitive cubic array. Five different particle volume fractions were considered. The results from these simulations are compared to Maxwell's equation in Figure 7–3. The solid circles correspond to results from particles with $\lambda_p = 1.3$ W/(m K) and the squares to $\lambda_p = 400$ W/(m K). The corresponding line were calculated using Maxwell's equation.

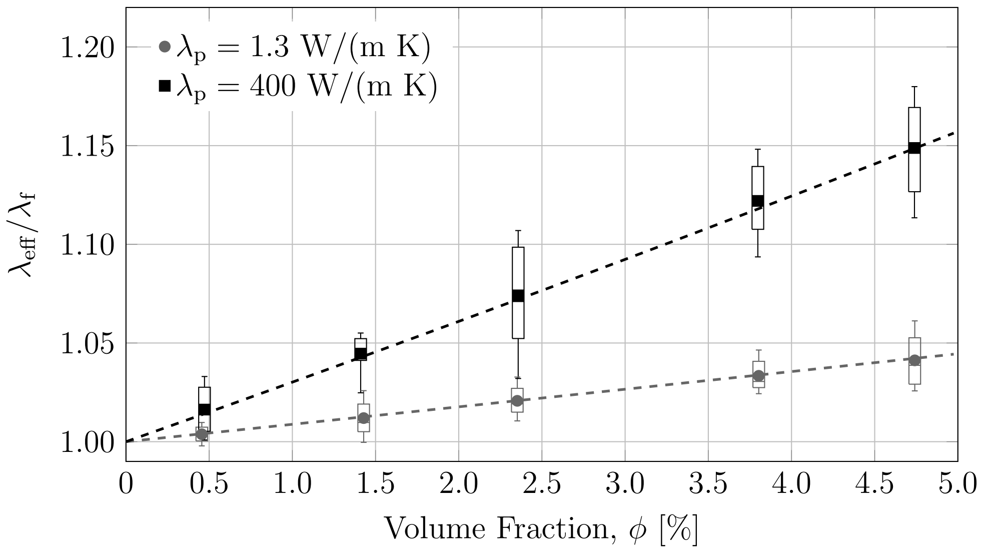

Figure 7–3: Normalize effective thermal conductivity vs. particle volume fraction for composite materials using the Gaussian pulse method. Numerical experiments represented by the symbols, and Maxwell's equation at corresponding λ_p indicated by lines. λ_p in W/(m K).

In this particular case the number of Gaussian pulses used were 48 in a 96 lattice domain. Each pulse was shifted 2 lattice units from the one before to cover the entire domain. Figure 7–3 also includes box plots for each set of simulations. These box plots give an indication of the spread in the estimation of a single average. The spread is related to local variations of the particle volume fraction due to the finite size of the pulse used. The estimation of the macroscopic thermal diffusivity is given by the average value; only this value is considered in the rest of this thesis.

Figure 7–3 can be considered as a validation that the Gaussian pulse method can be used to estimate the effective thermal conductivity of composite materials with spherical inclusions. This estimation requires careful selection of domain size and pulse width to ensure initial transients are completed during the simulation and that the results are not affected by pulse interactions due to the periodic boundary conditions imposed.

7.2.3 Mass Transfer

Applying the Gaussian pulse method to mass transfer simulations requires special attention as well. One of the main differences with heat transfer simulations is that mass transfer requires a larger number of time steps to reach the plateau region, in the order of 1000 times longer. Comparing to Figure 7–2 the number of time steps required would be in the order of 300k. Even though simulations with 300k time steps can be performed, this is not practical for an exploratory study, where the main objective is to study trends and the effect of different parameters, while the absolute value may not be of importance.

The number of time steps for mass transfer simulations was set to 3k. This was found to be a good compromise between simulation time and accuracy (compared to Maxwell's equation for composite materials). The results obtained for 3k and 30k time steps are compared in Figure 7–4. This figure shows the normalized effective mass diffusivity as a function of particle volume fraction. The squares correspond to short simulations with 3k time steps, while the circles correspond to longer simulations, 30k time steps. The box plot information in Figure 7–4 have been left out on purpose to improve legibility of the figure. The magnitude of the box plots are of the same size as in Figure 7–3.

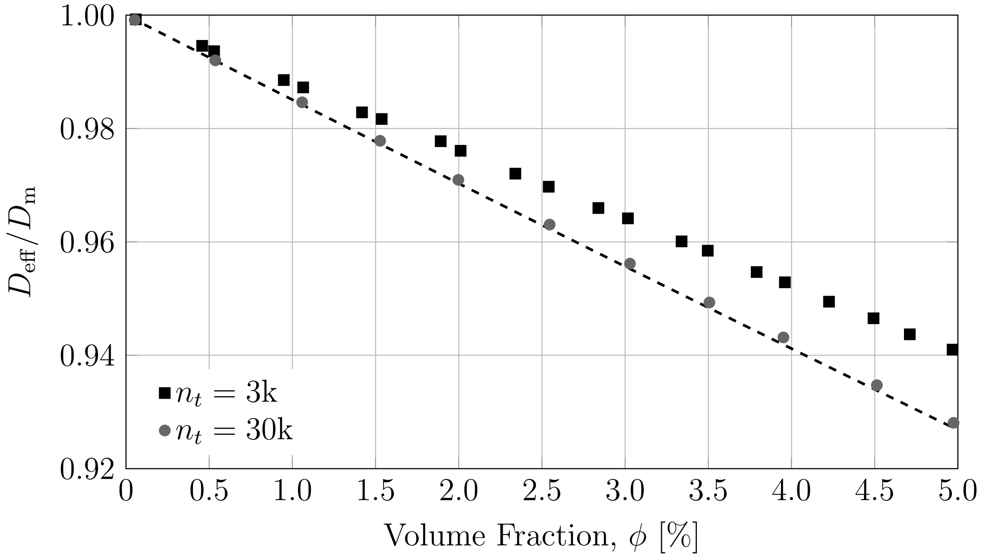

Figure 7–4: Normalized effective mass diffusion coefficient vs. volume fraction for composite material using the Gaussian pulse method. Results from short and long numerical experiments (symbols) and Maxwell's equation (dashed line).

Figure 7–4 clearly indicates a bias for the results from short simulations. However, short simulations can be obtained in one tenth the time long simulations would take. Note that the main feature for composite materials, a decrease of the effective mass diffusivity with particle volume fraction, is well captured by the short simulations.

The bias in the estimated effective coefficient is of the order of 0.5%. Although precise, this is not a fair estimation of the error introduced by the short simulations. Considering that the deviation from the molecular diffusivity is what is being estimated, the bias introduced by using short simulations in the order of 20%.

The difference between the estimation (squares) and Maxwell's equation (dashed line) is referred to as a bias because this difference is always in the same direction, underestimating the deviation from the molecular mass diffusivity. Mass transfer simulations are different from heat transfer in the sense that particles are insulators, i.e. zero mass diffusivity. Therefore, the initial evolution of the Gaussian peak would be prescribed by the molecular mass diffusivity and will evolve during the pseudo-transient towards the effective value of the effective coefficient. In contrast, heat transfer simulations with conductive particles would give an initial increase in the second moment that is affected by the thermal conductivity and the heat capacity of the inclusion. This initial increase in heat transfer simulations may be larger than the effective thermal conductivity.

Therefore, all results from short simulations are expected to be biased towards the value of molecular mass diffusivity. This corresponds to a bias towards one in the normalized effective mass diffusivity.

Despite the large bias in the estimation, all numerical experiments (composite materials or nanofluids in chapter 9) were done using short simulations. Since the main objective is to perform an exploratory analysis, the fact that the main features are captured by the numerical model justifies using short simulations. Therefore, the results from short simulations should be compared to the biased results and not to the theoretical model. For instance, Maxwell's equation for insulating inclusions reduces to:

$$\frac{D_{\mathrm{eff}}}{D_{\mathrm{m}}} = 1 + B_2\phi$$

Where $B_2 = -\frac{3}{2}$ for Maxwell's equation. This equation corresponds to the dashed line in Figure 7–4. A linear regression of the squares in Figure 7–4 (short simulations) gives a different coefficient of the particle volume fraction, $B_2 = -1.27$. These results will be further discussed in chapter 9.

Chapter 8
Heat Transfer in Nanofluids

Both methods introduced in chapter 6 were utilized to estimate the effective thermal conductivity of nanofluids. Furthermore, the temperature dependency of the effective thermal conductivity was also studied. The results from these simulations are discussed in the sections below.

8.1 Temperature Field

The evolution of the temperature field over time is represented in Figure 8–1. The results shown in this figure correspond to Gaussian pulse simulations. The intersecting plane shown in the figure is taken from the center of the pulse. For a homogeneous material the entire field should have the same temperature across, however, the presence of the particles modify the field and produce the variations shown in Figure 8–1.

The computational domain used in the simulations shown in Figure 8–1 correspond to a 0.5% nanofluid. The particles in front of the intersecting plane have been made semitransparent to improve readability. The gray scale in the figure corresponds to temperature, the darker the higher the temperature for a given cross section. Each domain in the figure has been normalized independently of the others, therefore, they cannot be compared with each other.

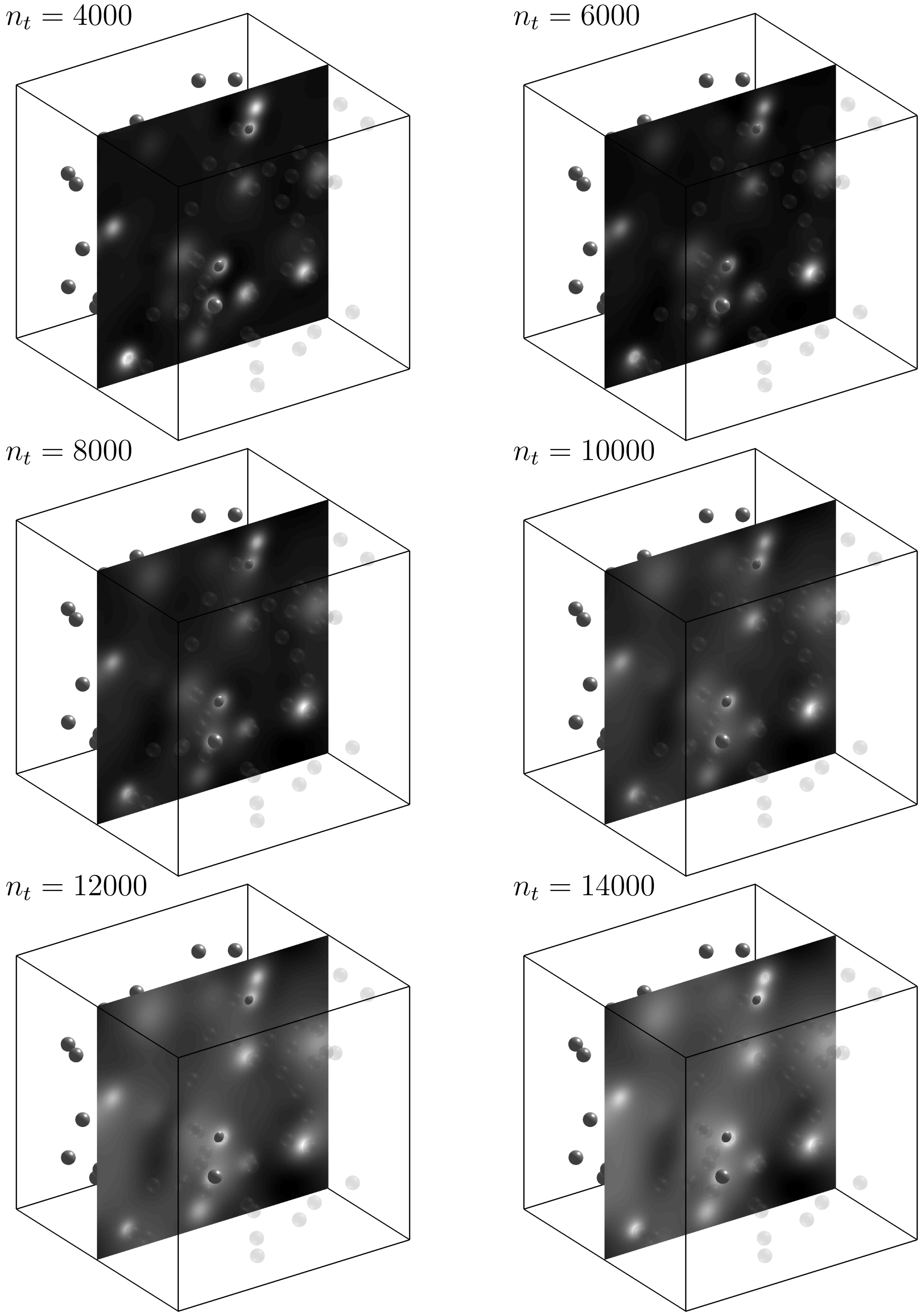

$n_t = 4000$

$n_t = 6000$

$n_t = 8000$

$n_t = 10000$

$n_t = 12000$

$n_t = 14000$

Figure 8–1: Evolution of the temperature field for a 0.5% volume fraction nanofluid. Simulation using the Gaussian pulse method. The intersecting plane is placed at the center of the pulse. Darker indicates higher temperature.

Very little information can be extracted from Figure 8–1. It is presented here as a visualization of the intermediate results obtained as part of the process of calculating the effective thermal conductivity. Although, only results from the Gaussian pulse method are shown, the results from the fixed gradient method are similar.

8.2 Using the Fixed Gradient Method

The fixed gradient method was used to estimate the effective thermal conductivity of two types of water-based nanofluids: CuO with $\lambda_{\mathrm{p}} = 17$ W/(m K) and SiO_2 with $\lambda_{\mathrm{p}} = 1.3$ W/(m K). The particle size for all simulations was set to 10 nm. The temperature was set to 295 K, which also sets the fluid properties used, see Appendix A. Particle densities and heat capacities were also constant, also indicated in Appendix A. The results from these simulations are shown in Figure 8–2.

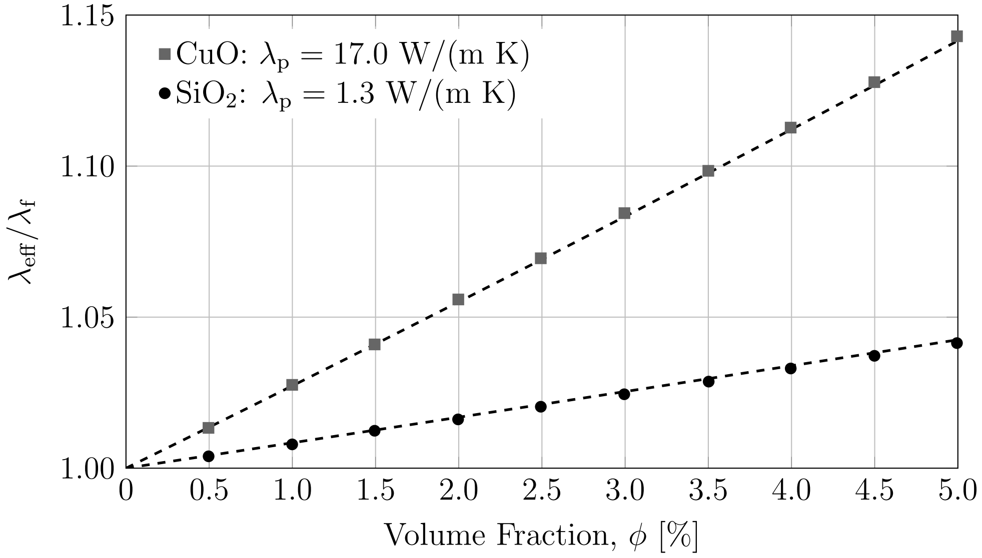

Figure 8–2: Normalized effective thermal conductivity vs. volume fraction for 10 nm CuO and 10 nm SiO_2 nanofluids. Estimation using the fixed gradient method.

The effective thermal conductivity for 10 nm CuO-Water (suquares) and 10 nm SiO_2-Water (circles) nanofluids are shown in Figure 8–2. The dashed lines in the figure correspond to Maxwell's equation for composite materials using the corresponding particle thermal conductivity for the inclusions.

Figure 8–2 is practically the same as Figure 7–1, but the results shown here correspond to the thermal conductivity calculated while particles move. This similarity, and the fact that both curves follow Maxwell's equation indicates that the effective thermal conductivity of nanofluids can be described using Maxwell's equation. In a more conservative way, this indicates that Brownian motion-induced microconvection currents cannot account for the high enhancements observed experimentally.

Although, only one particle size has been presented in Figure 8–2, the conclusions are the same for other particle sizes. This will be discussed in the next section.

8.3 Using the Gaussian Pulse Method

The Gaussian pulse method was also used to estimate the effective thermal conductivity of water-based nanofluids using CuO and SiO_2 nanoparticles. The fluid and particle physical properties are similar to the previous section. In these simulations the particle diameter was varied between 2 nm and 1000 nm. The results from these simulations are shown in Figure 8–3.

Similar to Figure 8–2, the symbols in Figure 8–3 indicate the results from numerical simulations while the dashed lines are calculated from Maxwell's equation at the

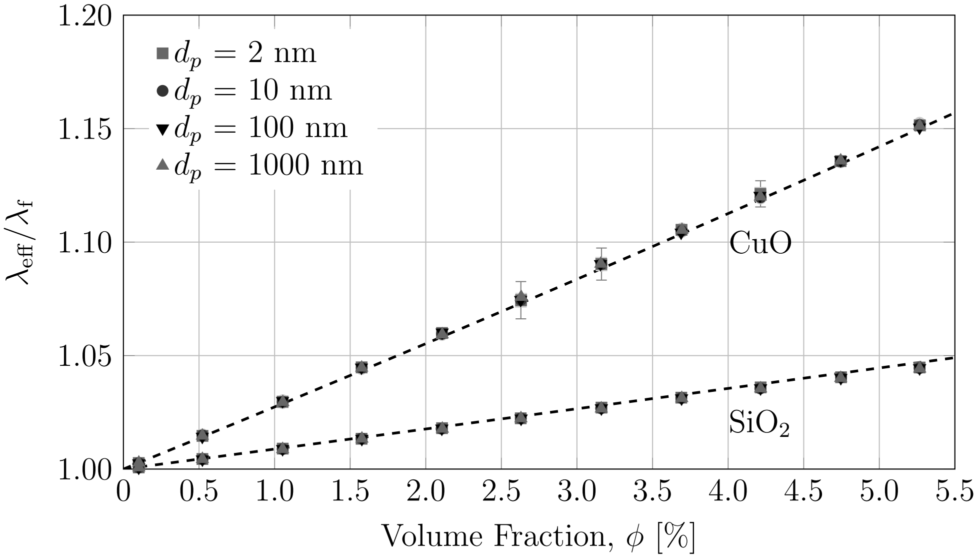

Figure 8–3: Normalized effective thermal conductivity vs. volume fraction for CuO and SiO_2 nanofluids. Particle size between 2 and 1000 nm. Estimation using the Gaussian pulse method (symbols). Maxwell's equation (lines)

corresponding particle thermal conductivity. Each symbol in the graph corresponds to the mean value of at least 6 repeats. The error bars indicate the 95% confidence interval on the mean. In most cases the error bars are not visible because the interval is too small for the scale used. Despite the random nature of the simulation the estimated values are very close to the line given by Maxwell's equation.

Figure 8–3 indicates that there is no particle size dependency on the effective thermal conductivity of nanofluids. Even the smaller particles simulated (2 nm) give the same enhancement as calculated from Maxwell's equation.

8.4 Temperature Dependency

A series of simulations at different temperatures was also conducted. The 275 to 365 K range was covered. The simulations were done with 10 nm SiO_2 particles and water properties at the temperature indicated (see Appendix A). The Gaussian pulse method was used to calculate the effective thermal conductivity. The results from these simulations are shown in Figure 8–4 (solid symbols). The dashed lines in this figure correspond to Maxwell's equation.

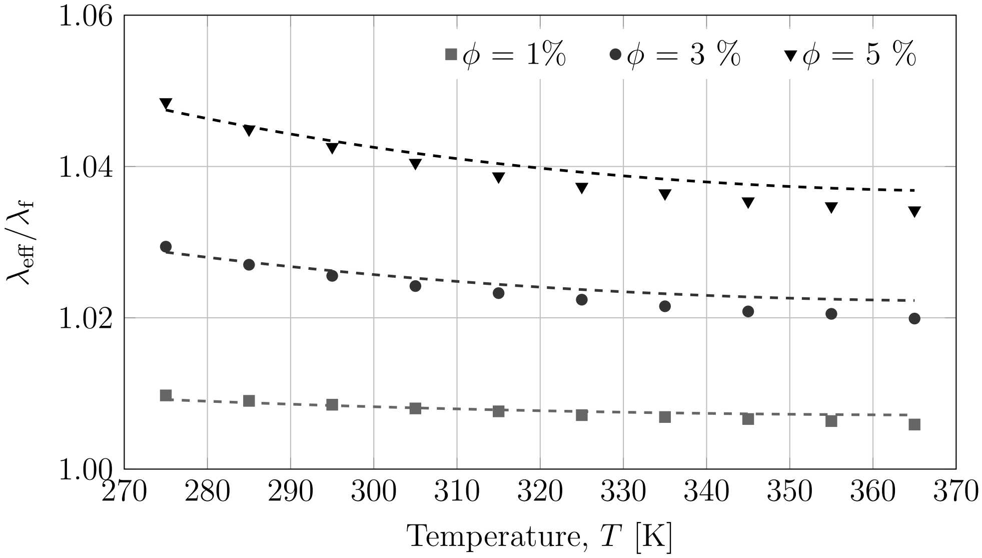

Figure 8–4: Normalized effective thermal conductivity vs. temperature for 10 nm SiO_2 nanofluid at three different particle volume fractions. Estimation using the Gaussian pulse method (symbols). Lines correspond to estimation using Maxwell's equation.

The slight decrease in the effective thermal conductivity with temperature is explained by the thermal conductivity increase of the fluid with temperature. For this particular case, where the particle's thermal conductivity is close to the fluid's thermal conductivity, Maxwell's equation inherits temperature dependency through the thermal conductivity of the fluid. The increase of λ_{f} with temperature gives a decrease in the ratio $\lambda_{\mathrm{eff}}/\lambda_{\mathrm{f}}$, thus explaining the small decrease observed in the simulations.

Despite the large changes in fluid viscosity with temperature (see chapter 9), the effective thermal conductivity of nanofluids, as estimated by the numerical experiments conducted, is well described by Maxwell's equation for composite materials.

The analysis done in this chapter sustains the hypothesis that Brownian motion-induced micro-convection currents cannot explain the high enhancement in thermal conductivity measured in nanofluids. This conclusion has also been reached by Babaei et al. (2013) using molecular dynamics, by He and Qiao (2008) using dissipative particle dynamics and by Buongiorno et al. (2009) through experimentation. The explanations given by Veilleux (2010) is that the Péclet number for heat transfer is smaller than 1, thus heat convection is too small compared to heat diffusion to induce dispersion. This dispersion perspective will be discussed in the next chapter, where mass transfer is considered.

Chapter 9
Mass Transfer in Nanofluids

9.1 Implementation

In this section, the Gaussian pulse method is used to study mass transfer in nanofluids. The computational domain, equations and boundary conditions have been described in Chapters 3 and 5. In particular, the size of domain is 192 cells in each direction while particles are 10 LU in diameter. The real size of the particles depends on the cell size Δx; for $d_p = 10$ nm a $\Delta x = 1$ nm is required. The initial Gaussian pulse standard deviation was set to $\sigma_0 = 20\Delta x$.

Two types of particle position distributions were considered. First, the particles were arranged as an array, where all particles are equidistant from each other. In the second approach, the particles are placed randomly in the domain. The restriction of having the particles 2 LU from the boundaries was used. Since the results from both types of simulations were similar, only the results for the random distribution are presented.

The simulations were done in two steps. First, the fLBM is used to calculate torque and forces for each particle. These values are stored in a file for use in the second step. For the second step, the hybrid LBM-FVM method is used to solve the concentration field with periodic boundaries and the initial conditions indicated below.

The second step consists of four pulses, each simulated independently of the others, but using the same forces and torques; this way all simulations follow the same particle trajectories. The evolution of the variance (Gaussian pulse) is then used to calculate the effective mass diffusivity D_{eff}. The results are presented as the ratio of the effective mass diffusion coefficient over the molecular diffusivity: $D_{\text{eff}}/D_{\text{m}}$.

A total of 6k time steps were simulated for each case. Longer simulations, 100k time steps, were also done for extreme cases where changes are significant. It was observed that the results were similar to those simulations with only 6k time steps.

The system used in this section is similar to the one studied experimentally by Veilleux and Coulombe (2010b): rhodamine 6G (R6G) in water-based alumina (Al_2O_3) nanofluid. The molecular diffusion coefficient for R6G used in the analyses below is $D_{\text{m}} = \ 3.3 \times 10^{-10}$ (Veilleux and Coulombe, 2010a). The dye diffusivity inside the nanoparticles is zero. Numerically, this was achieved by setting the diffusion coefficient inside the particle to a value close to zero ($1{\times}10^{-30}$).

9.2 Concentration Field and Evolution of M_2

A typical evolution of the concentration field over time is represented in Figure 9–1. The intersecting plane showed in the figure is taken from the center of the pulse. For a homogeneous material the entire field should have the same concentration across, however, the presence of the nanoparticles and Brownian motion-induced micro-convection currents modify the field and produce the variations shown in Figure 9–1.

The computational domain used in the simulations showed in Figure 9–1 correspond to a 5.0% nanofluid. The particles in front of the intersecting plane have been made semitransparent to improve readability. The gray scale in the figure corresponds to concentration, the darker the higher the concentration for a given intersecting plane. Each domain in the figure has been normalized independently of the others, therefore, they cannot be compared with each other.

Very little information can be extracted from Figure 9–1. It is presented here as a visualization of the intermediate results obtained as part of effective mass diffusion coefficient calculation process.

9.3 Effective Mass Diffusion Coefficient

The effective mass diffusion coefficient was calculated for different conditions. The effects of particle size, temperature, fluid viscosity and density, and particle density were studied. The results from these simulations are presented next. Due to the stochastic nature of the simulations each condition was simulated between 6 and 10 times. Only the mean value and its 95% confidence interval are presented in the figures below.

The base conditions for the simulations discussed below are:

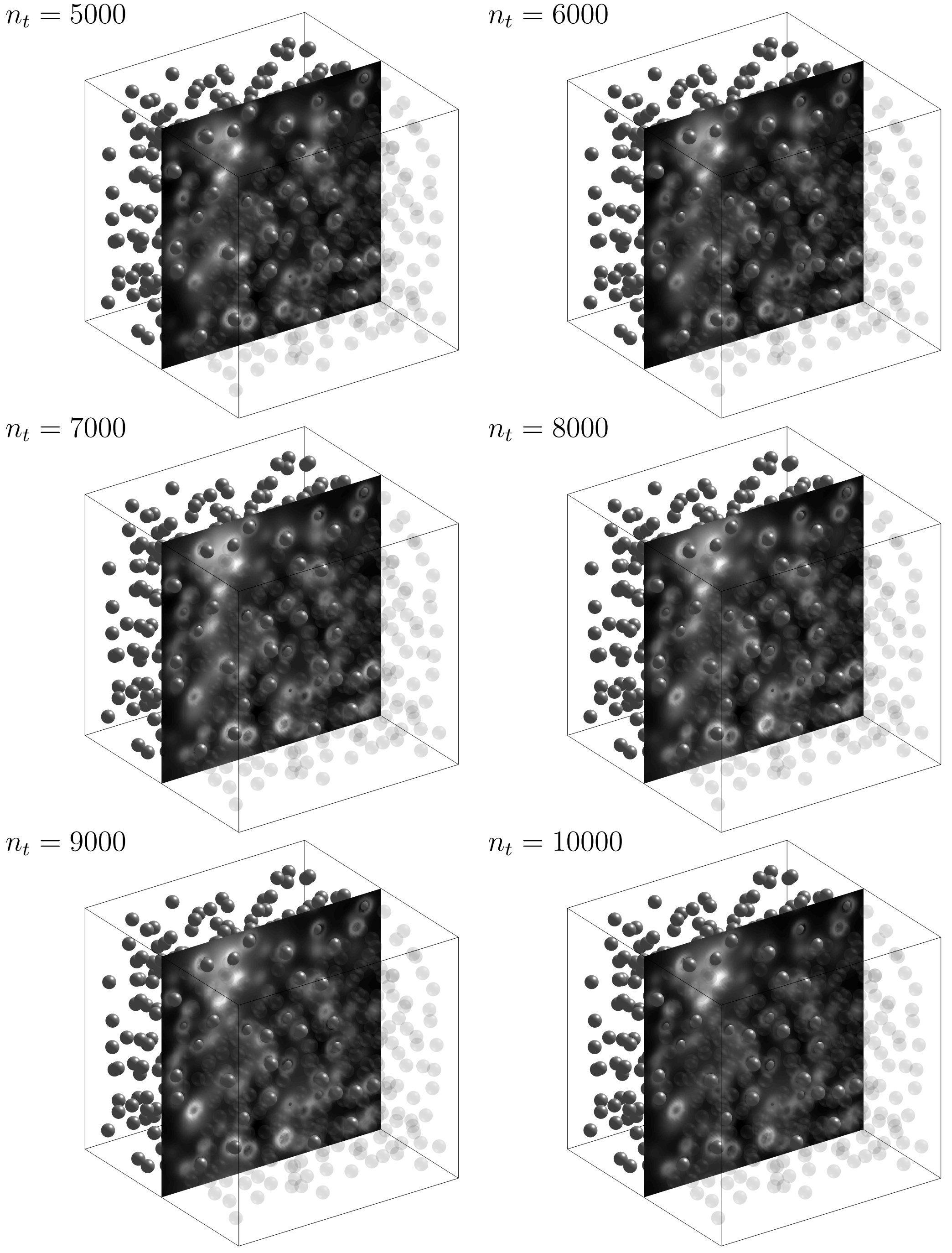

Figure 9–1: Evolution of the concentration field for a 5.0% volume fraction nanofluid. Simulation using the Gaussian pulse method. Concentration profile at the center of the pulse.

Table 9–1: Base conditions for parametric studies.

Parameter		**Value**	
Particle size	d_p	2	nm
Particle density (Al_2O_3)	ρ_p	4000	kg/m^3
Fluid density	ρ	1000	kg/m^3
Kinematic viscosity	ν	1.0×10^{-6}	m^2/s
Temperature	T	295	K

9.3.1 Particle Size

Particle diameter was varied from 2 to 100 nm. For each diameter a set of particle volume fractions in the range 0.1% to 5.0% was simulated. All simulations were done at a temperature $T = 295$ K. Figure 9–2 shows the normalized effective mass diffusion coefficient as a function of particle volume fraction for different particle diameters. The dashed line in Figure 9–2 corresponds to Maxwell's equation. Each point in the figure corresponds to the mean of 6 to 10 observations. Confidence intervals on the mean are also indicated in Figure 9–2. The solid lines correspond to a multilinear regression model, presented later on (see Eq. (9.5)).

Based on Maxwell's equation the effective mass diffusion coefficient is independent of particle size. Since the diffusion coefficient inside the particles is zero, a decrease in the effective mass diffusion coefficient with particle volume fraction would also be expected, as indicated by the dashed line in Figure 9–2.

A clear deviation from Maxwell's equation can be observed for particles smaller than 20 nm. The cases of 2 and 5 nm particles give values of the effective coefficient

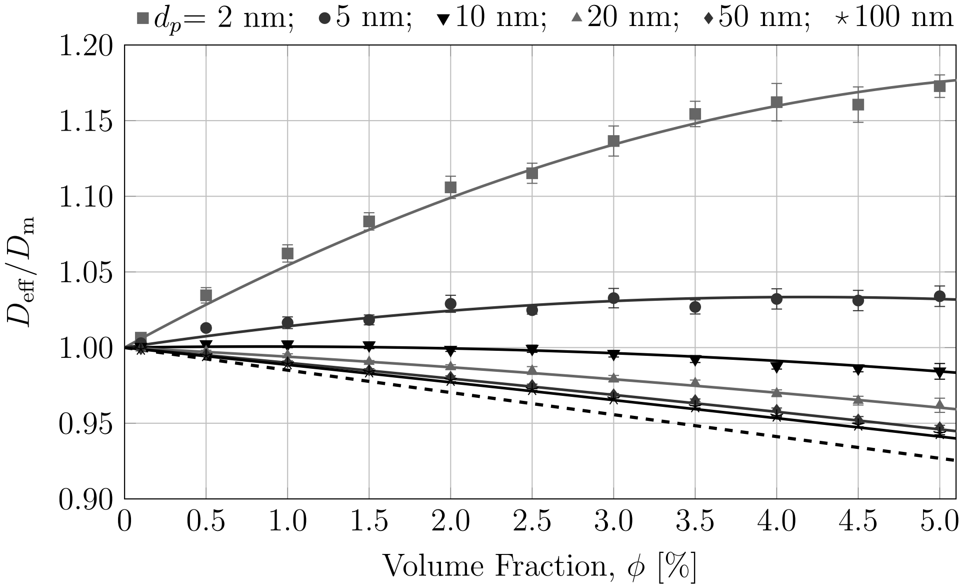

Figure 9–2: Normalized effective mass diffusion coefficient vs. volume fraction for nanofliuds with different particle size. Numerical simulations indicated by symbols and simplified model by thin lines, Eq. (9.5). The dashed line corresponds to Maxwell's equation, Eq. (2.2).

that are larger than the molecular diffusion. As particle size increases, the effective mass diffusion coefficient approaches Maxwell's equation.

The small differences between Maxwell's equation and the values for 100 nm particles are related to the short simulations used to estimate these values. This was discussed in chapter 7, where the solution to the discrepancy with Maxwell's equation was to perform longer simulations to determine the point where the Gaussian peak starts to interact significantly with the boundaries. In chapter 7 this was possible because the evolution of M_2 was smooth. For the case of nanofluids the evolution is no longer smooth and the estimation of the plateau region is impossible. However, the set for 100 nm particles in Figure 9–2 is similar to the results shown in Figure 7–4. Therefore, the enhancement for systems containing particles larger than 100 nm can be considered to be well represented by Maxwell's equation.

Another way to visualize the data presented in Figure 9–2 is to use the particle diameter in the abscissa. Figure 9–3 shows the normalized effective mass diffusion coefficient as a function of particle diameter for three values of the particle volume fraction. This figure shows that the effective mass diffusion coefficient decreases with particle size. The mass diffusivity decreases asymptotically towards the value given by Maxwell's equation at the corresponding particle volume fraction.

As indicated before, the lines in Figure 9–2 and Figure 9–3 correspond to a multi-linear regression model introduced later (see Eq. (9.5)). The objective of this model

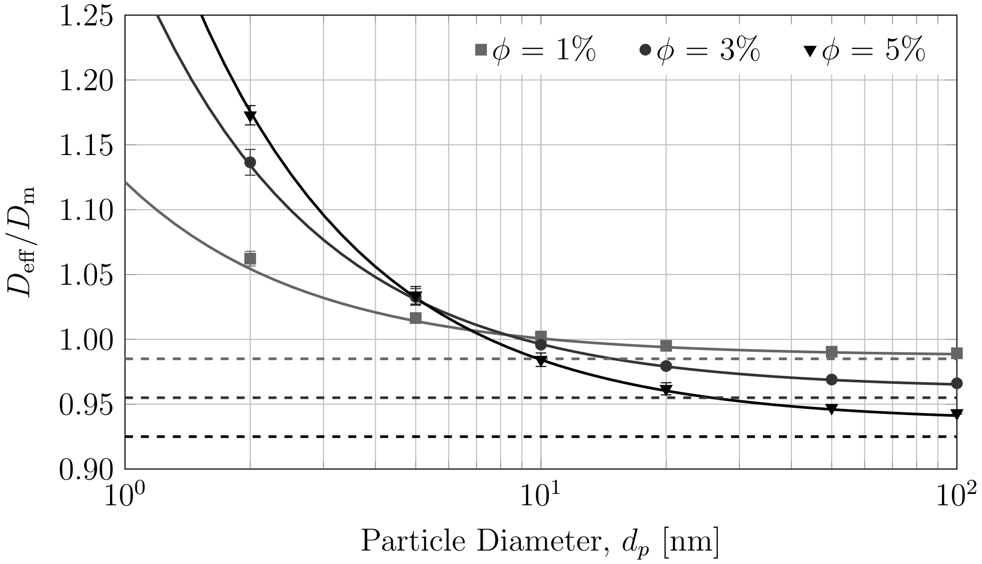

Figure 9–3: Normalized effective mass diffusion coefficient vs. particle diameter for nanofliuds at three particle volume fractions. Numerical simulations (symbols), simplified model (solid lines), and Maxwell's equation (dashed lines).

is to simplify the analysis. Assuming that Brownian motion is responsible for the enhancement and that the Stokes-Einstein diffusion coefficient (D_{BM}) for the nanoparticles appears in the equation, one would expect to see an inverse relationship between enhancement and particle diameter.

$$D_{\mathrm{BM}} = \frac{k_B T}{3\pi\eta d_p}$$

Furthermore, the enhancement should increase linearly with temperature and change inversely proportional to the dynamic viscosity. The results shown in Figure 9–2 and Figure 9–2 were obtained from simulations at different particle volume fractions and particle diameters, while maintaining all other parameters constant. Therefore, the following simplified model can be used to analyze the dependency on particle diameter and particle volume fraction.

$$\frac{D_{\text{eff}}}{D_{\text{m}}} = \frac{A(\phi)}{d_p} + B(\phi) \tag{9.1}$$

Initially, Eq. (9.1) was used to fit each set in Figure 9–3 and also the sets from Figure 9–2 not shown in Figure 9–3. It was noticed that $B(\phi)$ followed the expected Maxwell's equation for composite material, while $A(\phi)$ seems to follow a simple second order polynomial.

For the case of large particles, the model should give Maxwell's equation. When there is no diffusion inside the particles Maxwell's equation simplifies to $D_{\text{eff}}/D_{\text{m}} = 1 - \frac{3}{2}\phi$. This corresponds to $B(\phi)$ in Eq. (9.1). The form of the numerator $A(\phi)$ is unknown, however, one property is that it should give zero at $\phi = 0$. A second order function with zero intercept was arbitrarily selected to represent this term, $A(\phi) = A_1\phi + A_2\phi^2$. The multilinear model used is:

$$\frac{D_{\text{eff}}}{D_{\text{m}}} = A_1\,\phi\left(\frac{1}{d_p}\right) + A_2\,\phi^2\left(\frac{1}{d_p}\right) + B_1\,\phi + 1 \tag{9.2}$$

The independent variables, ϕ and $1/d_p$ are indicated in parentheses. Instead of using the simplified Maxwell equation, the coefficient B_1 was introduced to account for numerical discrepancies. An R^2 of 0.997 was obtained for the multilinear regression, indicating a good agreement between the numerical experiments and the simplified multilinear model. The expected value for B_1 is $-\frac{3}{2}$, while the fitted value gives $B_1 = -1.26$. Furthermore, this analysis indicates that the enhancement is inversely proportional to particle diameter.

Equation (9.2) can be rearrange in the following form

$$\frac{D_{\mathrm{eff}}}{D_{\mathrm{m}}} = 1 + \left[B_1 + \frac{A_1}{d_p}\left(1 + A_3\phi\right)\right]\phi \tag{9.3}$$

Where $A_3 = A_2/A_1$. The A coefficients for the multilinear model are: $A_1 = 15.01$, $A_2 = -112.5$ and $A_3 = -7.50$. The form presented in Eq. (9.3) (second term inside the square brackets) can be compared with the self-diffusion coefficient of interacting Brownian particles (Batchelor, 1976; Veilleux and Coulombe, 2011)

$$\frac{A_3}{d_p}\left(1 + A_5\phi\right) \rightsquigarrow D_{\mathrm{BM}}\left(1 - 1.83\phi\right) \tag{9.4}$$

Although $A_3 = -7.50$ differs from -1.83, the value given by Batchelor (1976), the negative sign of A_3 suggests that the slope decrease of the effective mass diffusion coefficient with particle volume fraction is related to particle interactions. The term $A_3\phi$ is related to the rate of change of mean-squared displacement of one particle due to the presence of similar particles (Batchelor, 1976).

Besides indicating that the A_3 term is related to particle interactions, Eq. (9.4) also suggests that A_1/d_p should be related to the self-diffusion coefficient of a Brownian particle, D_{BM}. Incorporating this information into the model gives:

$$\frac{D_{\mathrm{eff}}}{D_{\mathrm{m}}} = 1 + \left[B_2 + C_1\mathrm{N}_{\mathrm{BM}}\left(1 + \mathrm{C}_2\phi\right)\right]\phi \tag{9.5}$$

Where $\mathrm{N_{BM}}$ is a dimensionless quantity defined as the ratio of the diffusion transport rate by Brownian motion over the diffusion transport rate by molecular diffusion. Equation (9.5) is referred as the simplified model through out this work. In the case of mass transport $\mathrm{N_{BM}}$ is given by:

$$\mathrm{N_{BM}} = \frac{\mathrm{D_{BM}}}{\mathrm{D_m}} = \frac{\mathrm{k_B T}}{3\pi\nu\rho \mathrm{d_p}} \frac{1}{\mathrm{D_m}} \tag{9.6}$$

So far, only the inverse relationship with particle diameter has been identified. The other relationships, temperature, viscosity and fluid/particle density, are discussed below. The model presented in Eq. (9.5) was used to produce the solid lines in Figure 9–2 and other figures in this chapter. The values for the coefficients in Eq. (9.5) are: $B_2 = -1.27$, $C_1 = 10.5$, and $C_2 = -6.68$. These were obtained from multilinear-regression of all the points in Figure 9–2 through Figure 9–8 and Eq. (9.5) as the model ($R^2 = 0.995$).

9.3.2 Temperature

Based on Eq. (9.5) the effective mass diffusion coefficient should increase linearly with temperature. Simulations were performed for different temperatures and three different particle volume fractions. The other parameters were kept at the base settings indicated in Table 9–1. The results from these simulations are shown in Figure 9–4.

In Figure 9–4 the simulated data (symbols) indicate an increase of the effective mass diffusion coefficient with temperature. When considering the model prediction

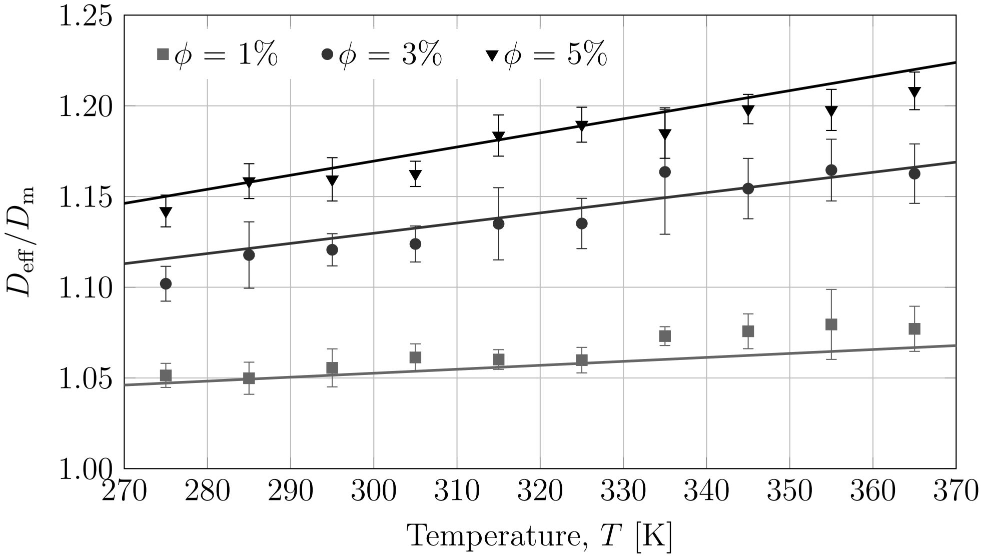

Figure 9–4: Normalized effective mass diffusion coefficient vs. temperature for nanofluids at three particle volume fractions. Numerical simulations (symbols), simplified model (lines).

the imposed linear increase accurately describes the simulated data. Increasing the temperature of the system increases the velocity of the particles, therefore increasing the effective mass diffusion coefficient.

9.3.3 Viscosity

The effective mass diffusion coefficient is expected to have an inverse relationship with fluid viscosity. In this case the kinematic viscosity, ν, is considered because this is the natural input parameter for the fLBM simulations. Simulations with different viscosities and three different particle volume fractions were performed; all other parameters were kept at the base settings (Table 9–1).

Similar to the previous figures, in Figure 9–5 the mean from the simulations are indicated with symbols, while the model predictions are shown as solid lines. For a given particle volume fraction the effective mass diffusion coefficient decreases as the fluid viscosity increases. The fluid viscosity represents the resistance to motion, the lower the viscosity the faster the average velocity of the particle would be, therefore the higher the effective mass diffusion coefficient.

For very high viscosities the particles move very little and the effective mass diffusion coefficient should follow Maxwell's equation for composite materials. This phenomenon can be observed in Figure 9–5, where the high viscosity values all follow Maxwell's equation.

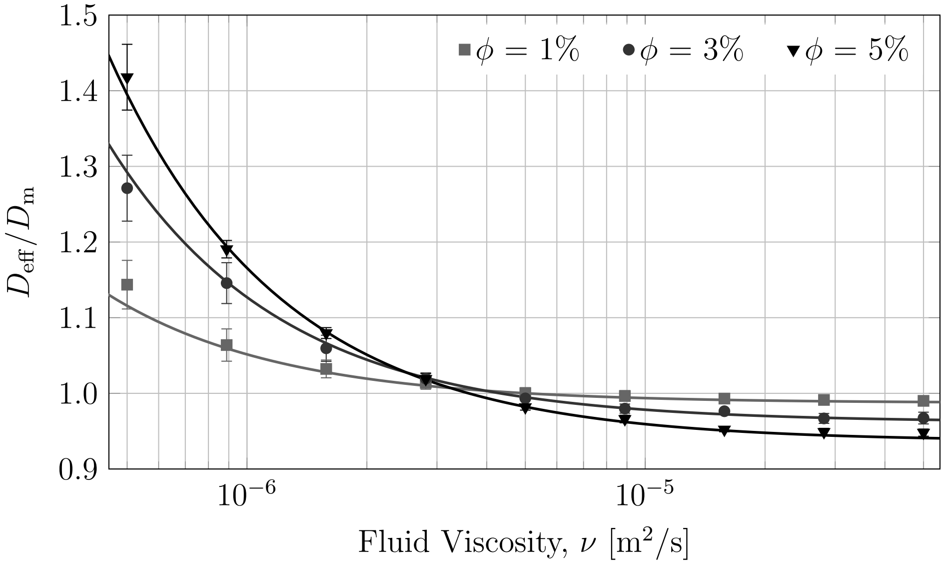

Figure 9–5: Normalized effective mass diffusion coefficient vs. fluid viscosity for nanofliuds at three particle volume fractions. Numerical simulations (symbols), simplified model (lines).

The model lines shown in Figure 9–5 accurately describes the simulated results, thus indicating that the effective mass diffusion coefficient for nanofluids increases with the inverse of the fluid viscosity.

9.3.4 Fluid Density

The effective mass diffusion coefficient is expected to depend on the inverse of the fluid density (constant kinematic viscosity, ν). Simulations with different fluid densities were performed, the results are shown in Figure 9–6.

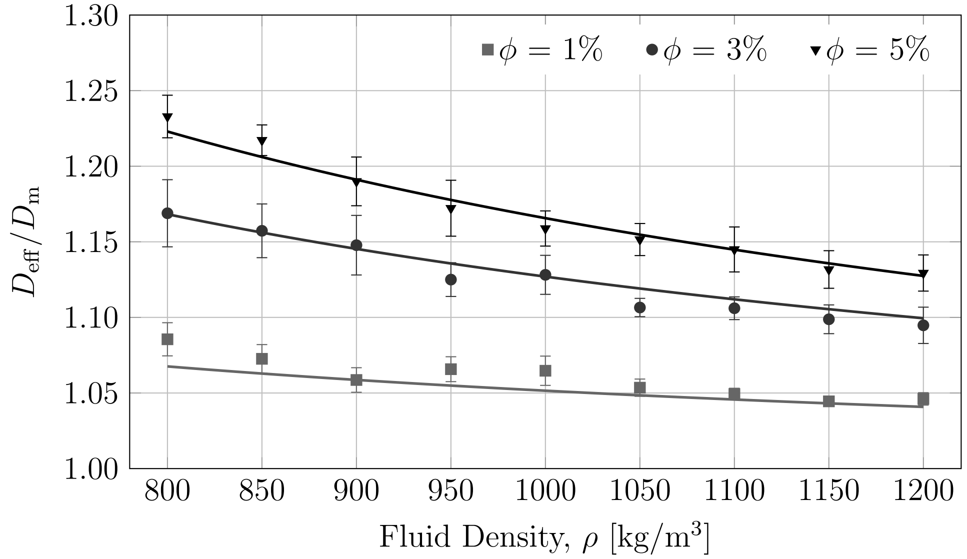

Figure 9–6: Normalized effective mass diffusion coefficient vs. fluid density for nanofliuds at three particle volume fractions. Numerical simulations (symbols), simplified model (lines).

Similar to the analysis for viscosity, Figure 9–6 indicates that the inverse relationship imposed by Eq. (9.5) accurately describes the data from the numerical experiments.

9.3.5 Particle Density

Numerical experiments with different particle densities were also conducted. The results from these simulations are presented in Figure 9–7. Similar to previous figures, Figure 9–7 shows the mean value along with the 95% confidence intervals. Only one line corresponding to Eq. (9.5) is shown in the figure. The lines for the other densities overlap the line shown. The particle densities chosen for these simulations correspond to typical nanofluids.

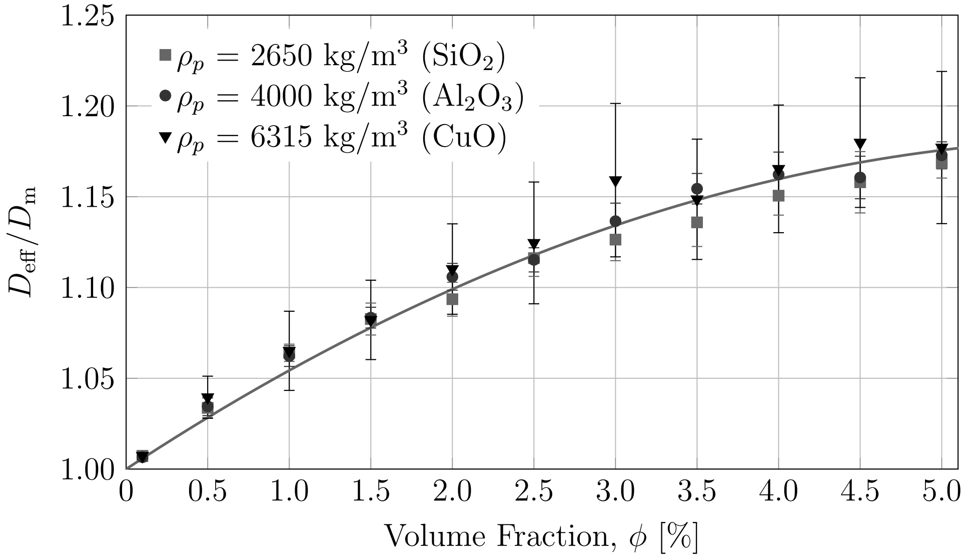

Figure 9–7: Normalized effective mass diffusion coefficient vs. volume fraction. Three types of nanofliuds with different particle densities (SiO_2, Al_2O_3 and CuO). Numerical simulations (symbols), simplified model (line).

Assuming that the only influence on the effective mass diffusion coefficient is Brownian motion of the particles, the effective mass diffusion coefficient is expected to be independent of particle density, as indicated by Figure 9–7. This is clear for SiO_2 and Al_2O_3 particles. The mean effective mass diffusion coefficient for CuO particles is slightly higher compared to the other two data sets. However, the large variance in the results prevents from drawing a final conclusion for the dependency of the effective mass diffusion coefficient on particle density.

Throughout the simulations, it was observed that the current model gives very high variances when simulating particles with high density and at high temperatures. In situations where both cases are encountered the resulting concentration field shows oscillations, a common behavior when the central-difference scheme is used beyond its limits.

The simulation issues with particle density can be better observed in Figure 9–8. In this figure the results from numerical experiments with different particle densities are shown. The normalized effective mass diffusion coefficient is shown as a function of particle specific gravity. The cases of particles of lower and higher density than the fluid are shown in this figure. Note the large confidence intervals on the mean for the high density cases. These large variances are due to problems with the numerical simulations and the limits of the central-difference scheme discussed above.

Although, small variations can be observed, in general Figure 9–7 and Figure 9–8 suggest that the effective mass diffusion coefficient is independent of particle density. This results contradicts the model by Veilleux and Coulombe (2011), were it was proposed that particle density would have a significant effect on the effective mass diffusion coefficient.

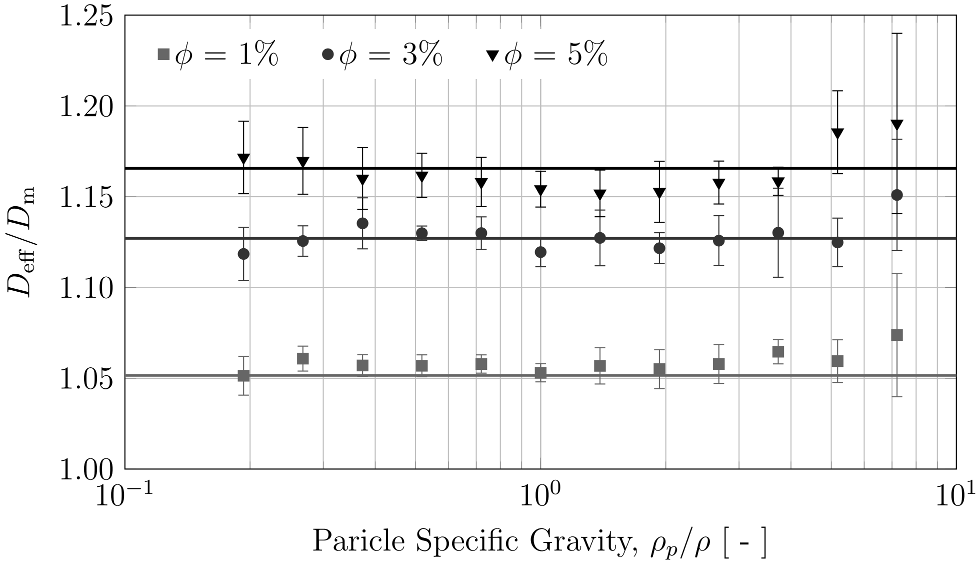

Figure 9–8: Normalized effective mass diffusion coefficient vs. particle density for nanofliuds at three particle volume fractions. Numerical simulations (symbols), simplified model (lines).

9.3.6 Summary: Parametric Analysis

In summary, the effective mass diffusion coefficient for nanofluids is affected by three principal components. First, the contribution from the composite material given by Maxwell's equation and represented by the coefficient B_2 in Eq. (9.5). This term ensures that, when particles are not moving the default behavior is Maxwell's equation. Although, B_2 was found to be -1.27, the theoretical value of $-\frac{3}{2}$ should be used instead.

The second contribution to the effective mass diffusion coefficient comes from Brownian diffusion, term $C_1\mathrm{N}_{\mathrm{BM}}$ in Eq. (9.5). This term increases the effective mass diffusion coefficient depending on the relative strength of the Brownian diffusion to the molecular diffusion.

The third contribution accounts for particle interactions, term $(1 + C_2\phi)$. This term reduces the effect of Brownian diffusion when particles interact with each other (Batchelor, 1976). This term is only valid for dilute suspensions, thus highlighting one of the main limitation of the simplified model in Eq. (9.5). For high particle volume fractions Eq. (9.5) would estimate effective mass diffusion coefficients lower than Maxwell's equation, because the Brownian diffusion with interaction gives a negative number, which is not physically possible.

Finally, one important finding from the previous exercise is that the effective mass diffusion coefficient for nanofluids is independent of particle density.

9.4 Diffusion of Rhodamine 6G on Al_2O_3-Water Nanofluid

In the previous section, Equation (9.5) was proposed as a simplified model to summarize all numerical experiments performed while changing a single parameter at the time. In this section a more realistic situation is explored, where an increase in temperature is also accompanied by changes in fluid density and viscosity. The system being simulated is the diffusion of R6G in Al_2O_3-Water nanofluid, in particular the effect of temperature is explored in this section.

Numerical experiments were conducted at different temperatures and particle volume fractions. The fluid properties dependencies on temperature are indicated in

Appendix A. The results from these simulations are shown in Figure 9–9 and Figure 9–10.

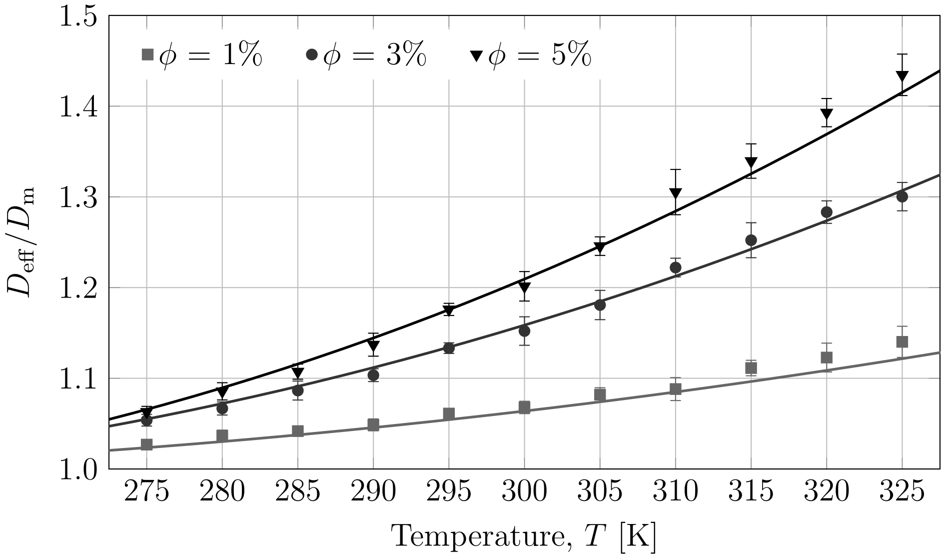

Figure 9–9: Normalized effective mass diffusion coefficient vs. temperature for nanofluids at three particle volume fractions. Numerical simulations (symbols), simplified model (lines). Fluid properties from Appendix A.

The normalized effective mass diffusion coefficient as a function of temperature is presented in Figure 9–9, where each curve corresponds to a different particle volume fraction. The symbols indicate the mean value for the numerical experiments along with the 95% confidence interval on the mean. The solid lines correspond to Eq. (9.5). Only the temperature between 275 and 325 K are shown. Simulations at higher temperature are outside of the range of the LBM-FVM model. For the case of water, the FVM solver gives oscillatory concentration fields at temperatures above 325 K.

The temperature dependency of the effective mass diffusion coefficient follows Eq. (9.5). If only the direct temperature effect is considered, a linear increase with temperature would be expected. Furthermore, comparing with Figure 9–4 the expected increase due to temperature change should not be larger than 0.05 in $D_{\text{eff}}/D_{\text{m}}$ for $\phi = 5\%$. However, the observed change is in the order 0.45 units in $D_{\text{eff}}/D_{\text{m}}$ for the same particle volume fraction. The increase in the effective mass diffusion coefficient with temperature is mainly related to the decrease of the fluid viscosity with temperature.

The viscosity changes from $\nu = 1.6 \times 10^{-6}$ m^2/s at 275 K to $\nu = 5.3 \times 10^{-7}$ m^2/s at 325 K. Comparing this change with the results presented in Figure 9–5 indicates that the large changes with temperature are related to the indirect change in fluid viscosity.

A different view of the effect of temperature on the effective mass diffusion coefficient is presented in Figure 9–10. In this figure, the normalized effective coefficient is presented as a function of particle volume fraction with the temperature as the fixed parameter for each curve shown. The typical second order in particle volume fraction shape is maintained for the three temperatures presented.

The comparison presented for Figures 9–9 and 9–10 can be considered as the validation of Eq. (9.5). The simulation results in these figures have not been used in the estimation of the coefficients of Eq. (9.5). Although, the entire ranges of temperature, viscosity, particle size, density and particle volume fraction have not

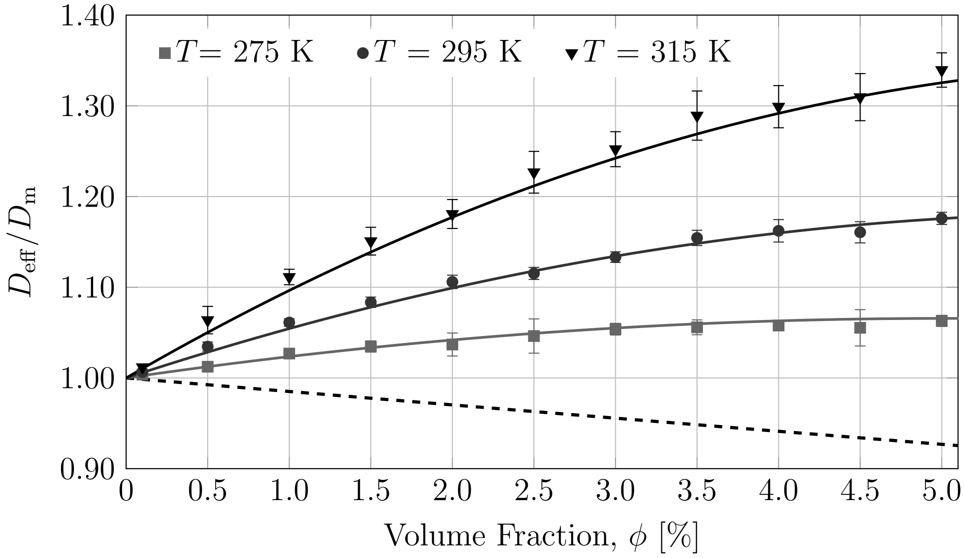

Figure 9–10: Normalized effective mass diffusion coefficient vs. volume fraction for nanofliuds at three temperatures. Numerical simulations (symbols), simplified model (lines), and Maxwell's equation (dashed line). Fluid properties from Appendix A.

been explored, the simplified model depicted by Eq. (9.5) accurately predicts the results from numerical simulations.

One important outcome of this analysis is that, for the case of water based nanofluids, the decrease in water viscosity with increasing temperature represents the main contribution to the effective mass diffusivity increase with temperature. This indicates that experiments with different temperatures are not expected to show a linear increase with temperature. Instead, the increase will be mainly dictated by the relationship of temperature and viscosity for the fluid in question. In other words, fluid viscosity must be considered when studying temperature dependency of mass transfer in nanofluids.

9.5 Comparison with Experimental Data

In this section, the simplified model in Eq. (9.5) is compared to experimental measurements from Veilleux and Coulombe (2010b) and the model proposed by Veilleux and Coulombe (2011). The main objective is to try to provide an explanation to the experimental measurements using the result discussed above.

The experimental measurements by Veilleux and Coulombe (2010b) indicate up to a 10 fold increase in the effective mass diffusion coefficient for the R6G, 10 nm Al_2O_3-water nanofluid. These measurements also indicate a maximum enhancement at around 2% particle volume fraction.

The numerical simulations and the simplified model proposed cannot account for the 10 fold increase in the effective mass diffusion coefficient. The maximum normalized effective mass diffusion coefficient calculated using Eq. (9.5) and the condition for the experimental measurements by Veilleux and Coulombe (2010b) is $D_{\mathrm{eff}}/D_{\mathrm{m}} = 1.17$. The large discrepancy cannot be explained at the moment. One possible explanation is that the simulations do not capture correctly the fluid field used in the LBM-FVM step. When simulating particle motion using MRT-LBM, the integration of the hydrodynamic force over a time step may produce artificial dissipation (Dünweg and Ladd, 2009). This could translate in a smaller magnitude of the velocity field, thus numerical experiments would estimate smaller enhancement compared to experiments.

Despite not estimating the proper order for the enhancement, Eq. (9.5) estimates the existence of a maximum enhancement with particle volume fraction. As the particle volume fraction increases, the interaction term decreases the contribution from Brownian motion, to the point that, mathematically, the contribution of Brownian motion can be completely cancelled by particle interactions. Beyond this point, the mathematical estimation is unrealistic, i.e. values below Maxwell's equation.

In the following analysis it is assumed that the main phenomena responsible for the enhancement measured by Veilleux and Coulombe (2010b) is Brownian motion. The enhancement is then governed by a function similar to Eq. (9.5) but the coefficients are allowed to change to accommodate possible modeling errors. Coefficient B_2 is set to its theoretical value of $-\frac{3}{2}$, while C_1 and C_2 will be estimated by fitting Eq. (9.5) to experimental data.

The experimental measurements from Veilleux and Coulombe (2010b) are shown in Figure 9–11 (symbols). The curves in this figure are discussed later. The data shows two different behaviors, below a particle volume fraction of 2% the effective mass diffusion increase seems to follow the second order curve predicted by Eq. (9.5). For particle volume fractions above 2% the behavior does not follow the decrease given by Eq. (9.5), which should be a mirror (approximately) to the first part ($\phi < 2\%$). Two possible explanations for this behavior are discussed: a) particle agglomeration and b) particle interaction/hindering.

9.5.1 Particle Agglomeration

At higher volume fractions particles are closer from each other and the probability of particle colliding and forming agglomerates increases. If it is assumed that the agglomeration onset takes place near 2%, the measurement above this point can be explained by the same model but with a larger effective particle diameter.

The coefficients for Eq. (9.5) were estimated from measurements below a volume fraction of 2% (Table 9–2). The fitted model corresponds to the $d_p = 10$ nm curve shown in Figure 9–11. The other curves in the figure were obtained by selecting the particle diameter that would cross the points volume fractions larger than 2%. One interesting fact is that the size of the agglomerates needed to explain the decrease are within the experimentally observed sizes (Veilleux, 2010). The nanofluid used in these experiments showed a bimodal distribution with one mode near 9 nm and the second mode near 30 nm. These modes are only visible in the size distribution function when presented as percent volume and not for particle count. These results are only available in Veilleux (2010).

Table 9–2: Agglomeration hypothesis. Fitted values for simplified model coefficients.

Parameter	**Value**	**95% CI**
C_1	790.4	638.9, 941.9
C_2	-21.55	-28.72, -14.38

The coefficients presented in Table 9–2 do not agree with the ones obtained from the simulations. The larger value for both coefficients may be related to simulation errors when calculating the velocity field. A possible explanation is the artifical dissipation discussed at the beginning of this section (section 9.5). The larger C_1

indicates that the Brownian motion of the particles has a larger influence in the enhancement than estimated by the numerical experiments. If the velocity field around the particle extends for larger distances than estimated by the MRT-LBM model, the value of C_1 would be larger. Similarly, particle interactions or hindering would be more important, thus giving also a larger C_2, in magnitude.

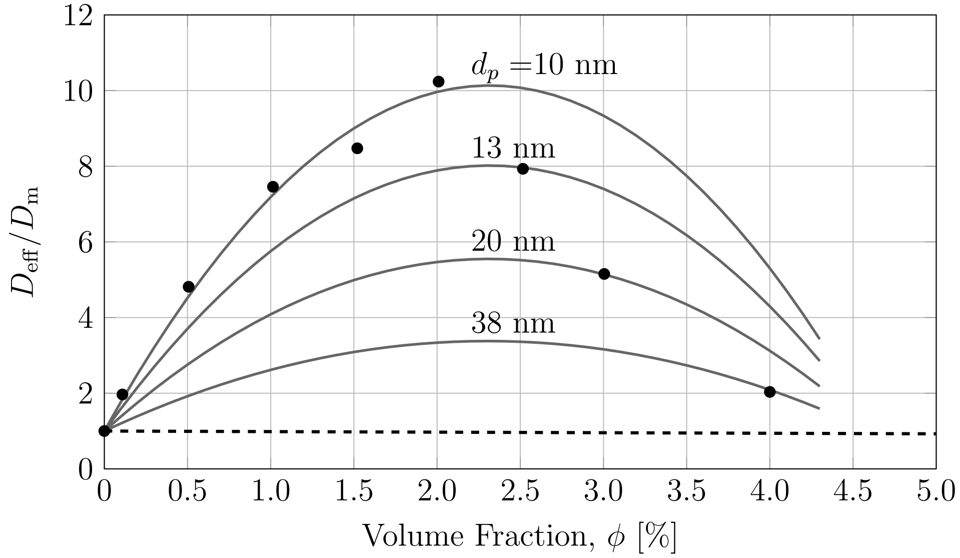

Figure 9–11: Agglomeration hypothesis. Comparison of experimental results from Veilleux and Coulombe (2010b) (symbols) and the simplified model (lines). Particle diameter selected to match experimental data above 2%.

Practically, any point below the maximum can be estimated by the model assuming that agglomeration takes place. The good fit of the model without agglomeration for volume fractions below 2% suggests that the model proposed by Eq. (9.5) could explain these results. Further studies are required to validate this hypothesis. These studies would require changing particle size and measuring particle size distributions for each point sampled to determine if agglomeration has taken place.

9.5.2 Particle Interaction/Hindering

The second possible explanation for the unusual decrease above 2% volume fraction is particle interaction or particle hindering. For the measurements by Veilleux and Coulombe (2010b) this is very important since the enhancement was measured near the wall; particle-particle and particle-wall interactions affect the Brownian diffusion coefficient.

The model proposed by Eq. (9.5) only accounts for particle-particle interactions. One of the main limitations of this model is that it is only valid for dilute suspensions. Particle-wall interaction further decreases Brownian diffusion (Banerjee and Kihm, 2005), depending on the distance to the wall. Although it is possible to incorporate particle-wall interactions into Eq. (9.5), this has not been done.

Since Eq. (9.5) is only valid for dilute suspensions ($\phi < 5\%$), for large particle volume fractions the predictions are unrealistic. Considering the parameters in Table 9–2, volume fractions above 4.7% would give values below Maxwell's equation. The expected behavior would be to have the interaction increase to the point that $(1 + C_2\phi)$ decrease to zero, which indicates that Brownian motion does not influence the system. To incorporate this desired behavior a sigmoid type function was added to Eq. (9.5):

$$h(\phi) = 1 - \frac{1}{1 + e^{-\frac{\phi - A_4}{A_5}}}$$

The new model is

$$\frac{D_{\text{eff}}}{D_{\text{m}}} = 1 + \left[-\frac{3}{2} + C_1 \mathrm{N}_{\mathrm{BM}} \left(1 + \mathrm{C}_2\phi\right) \mathrm{h}(\phi) \right] \phi \qquad (9.7)$$

The sigmoid function added to Eq. (9.5) has no physical meaning, but it has been chosen to mimic the desired behavior of smoothly decreasing the interaction term to zero. This produces a smooth transition between Eq. (9.5) and Maxwell's model. Four parameters are estimated from the experimental data. The value of these parameters are shown in Table 9–3. A visual comparison of the fitted model and the experimental data is shown in Figure 9–12.

Table 9–3: Particle hindering hypothesis. Fitted values for simplified model with sigmoid adjustment.

Parameter	**Value**	**95% CI**
C_1	754.9	599.5, 910.4
C_2	-14.25	-31.00, 2.491
A_4	2.676	2.096, 3.256
A_5	0.4835	0.3538, 0.6132

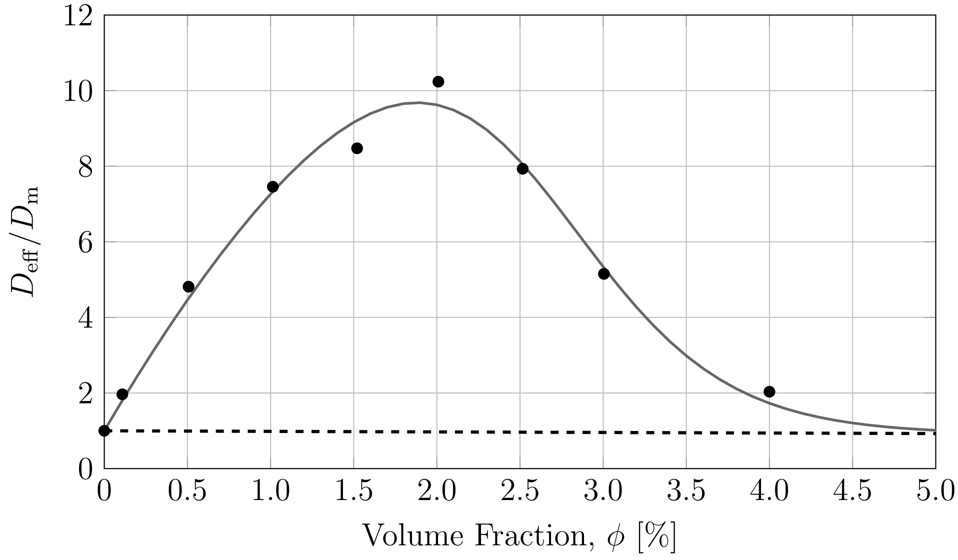

Figure 9–12: Particle interaction hypothesis. Comparison of experimental results from Veilleux and Coulombe (2010b) (symbols) and the simplified model (line). Simplified model with sigmoid function.

The new model with the sigmoid function represents some of the main characteristics of the experimental measurements. A maximum is reached near 2% volume fraction, followed by a long-tail decrease towards Maxwell's equation. However, looking carefully at the confidence intervals in Table 9–3 (C_2 parameter) reveals that an increasing function of ϕ without interaction term, would be a reasonable fit for the available data. This issue and the fact that the sigmoid function used has no known physical meaning limit the analysis. This discussion is presented here with the hope that it will help to focus research efforts in the study of mass transfer in nanofluids. In particular, this analysis reveals the importance of understanding particle interaction for suspensions that are not in the dilute limit.

In summary, two hypotheses for explaining the decrease in the effective mass diffusion coefficient in nanofluids have been presented: particle agglomeration and particle hindering. Both can be used to explain the experimental results of Veilleux and Coulombe (2010b), however further experimentation would be needed to determine which hypothesis is correct.

9.6 Relationship to Dispersion Model

The principles used in developing the numerical model used in this work are very similar to the ones considered in the dispersion model by Veilleux and Coulombe (2011). The idea behind both models is that particle Brownian motion generates micro-convective currents. These currents or perturbations of the velocity field on the fluid contribute to the increase in mass diffusion much similar to what is known as Taylor dispersion (Taylor, 1953).

Most types of Taylor-like dispersion are characterized by the presence of the Péclet number in their relationships between the effective and molecular diffusivities. This is true for many systems, including the initial propositions by Veilleux and Coulombe (2010b), where the effective mass diffusion coefficient was found to be proportional to the square of the Péclet number.

Veilleux and Coulombe (2011) proposed calculating the Péclet number by sampling velocities from the Maxwell-Boltzmann distribution, then averaging. However, to obtain a simple relation between the Péclet number and the important parameters in the analysis, the particle velocity was replaced by the root mean square (RMS) velocity, thus giving the following

$$\mathrm{Pe}^2 = \left(\frac{U_0 a}{D_\mathrm{m}}\right)^2 = \frac{3k_B T}{4\pi a \rho_p}\frac{1}{D_\mathrm{m}^2}(1-1.83\phi) \tag{9.8}$$

To facilitate the comparison with Eq. (9.6), the Péclet number without the interaction term is represented by $\hat{\mathrm{Pe}}$, thus

$$\mathrm{Pe}^2 = \hat{\mathrm{Pe}}^2(1-1.83\phi)$$

Comparing with Eq. (9.6), the following relationship between the N_BM and the Pe numbers can be established

$$\mathrm{N}_\mathrm{BM} = \frac{2}{9}\,\hat{\mathrm{Pe}}^2\,\mathrm{Sc}^{-1}\left(\frac{\rho_\mathrm{p}}{\rho}\right) \tag{9.9}$$

where Sc is the Schmidt number ($\mathrm{Sc} = \nu/D_\mathrm{m}$), which is the ratio between viscous diffusion and molecular mass diffusion rates. The density ratio is needed to eliminate the particle density introduced by the Pe^2 in the equation. This ratio is known as the momentum interaction parameter in the field of particulate flows, and it governs the relative acceleration experienced by the particles (Marble, 1963). Writing Eq. (9.5) in terms of the Péclet number gives

$$\frac{D_{\text{eff}}}{D_{\text{m}}} = 1 + \left[B_2 + \left(\frac{2}{9} \frac{C_1}{\mathrm{Sc}} \frac{\rho_p}{\rho} \right) \hat{\mathrm{Pe}}^2 \left(1 + C_2 \phi\right) \right] \phi \tag{9.10}$$

The Schmidt number of Eq. (9.9) is in the order of 10^4 for the nanofluids in question, and the density ratio is of the order of 10, thus giving a factor of the order of $\mathrm{Sc}^{-1}\rho_p/\rho \approx 10^{-3}$. Considering the values obtained for C_1, the term in parentheses before $\hat{\mathrm{Pe}}$ would be smaller than one, a common value for Taylor dispersion cases.

The form presented in Eq. (9.10) is similar to equations representing Taylor dispersion. In the model presented here dispersion is the only phenomenon affecting mass diffusion. The exercise done in this section only aims at presenting Eq. (9.5) in a more familiar form, where the Péclet number appears explicitly in the equation.

Similar to the conclusion reached by Veilleux and Coulombe (2011), the model presented here indicates that micro-convection currents cannot explain the high enhancement observed for the thermal conductivity measurement on nanofluiuds. The Péclet number for heat transfer is small compared to its mass transfer counterpart ($\mathrm{Pe}_M \approx 1000\ \mathrm{Pe}_H$), thus making the dispersion contribution negligible compared to the other terms in the equation. This is in agreement with the results obtained from the numerical experiments in chapter 8.

9.7 Bidisperse Nanofluids

The issue of polydisperse nanofluids is addressed in this section. The development done up to this point requires the size of the particle to be known. However, for nanofluids it is common to have a distribution of particle sizes instead of a single size. Even though, the LBM-FVM model developed above is capable of simulating polydisperse nanofluids, only the bidiperse nanofluids have been considered, i.e. only two particle sizes.

The main idea behind studying bidisperse cases is to simplify the problem and to determine what kind of mixing rules can be applied in the study of the polydisperse cases.

Simulations using the LBM-FVM and the Gaussian pulse method were performed with different particle volume fractions of two particles sizes. Size A corresponds to 2 nm particles, while size B corresponds to 4 nm particles. The fraction of B particles, x_B, is defined to characterize the ratio of large particles in the domain.

$$x_B = \phi_B/\phi \tag{9.11}$$

where, $\phi = \phi_A + \phi_B$. Also, ϕ_A is the volume fraction of A particles and ϕ_B the fraction of B particles.

$$\phi_A = \frac{V_A}{V_T}; \qquad \phi_B = \frac{V_B}{V_T} \tag{9.12}$$

therefore,

$$x_B = \frac{V_B}{V_A + V_B} \tag{9.13}$$

Graphical representations of different particle volume fractions, ϕ, and B fraction, x_B, are shown in Figure 9–13. The particle volume fractions from top to bottom are 1, 3 and 5%. The domains on the left correspond to B fractions of $x_B = 0.2$, while the ones on the right are at $x_B = 0.7$. Despite having the same particle volume fraction, the domains on the right have less particle, compared to the domains on the left.

Fluid density and viscosity were computed from the equations for water properties in Appendix A at 295 K. Particles are Al_2O_3 with the two sizes indicated above. Simulations for three different particle volume fractions were performed (1, 3 and 5%), with at least eight repeats for each condition. The entire range of x_B fractions was covered, from 0 to 1. The results from these simulations are shown in Figure 9–14. Similarly to previous figures, the symbols indicate the mean values with their respective 95% confidence intervals.

The large confidence intervals shown in Figure 9–14 would justify using a linear model to explain the change. However, the mean value seems to follow a curve systematically above what a linear interpolation between extreme values would give. The solid lines in this figure correspond to a mixing model where the enhancements due to Brownian motion are assumed to be additive. Although mathematically incorrect, this mixing model highlights the importance of the interaction term, and

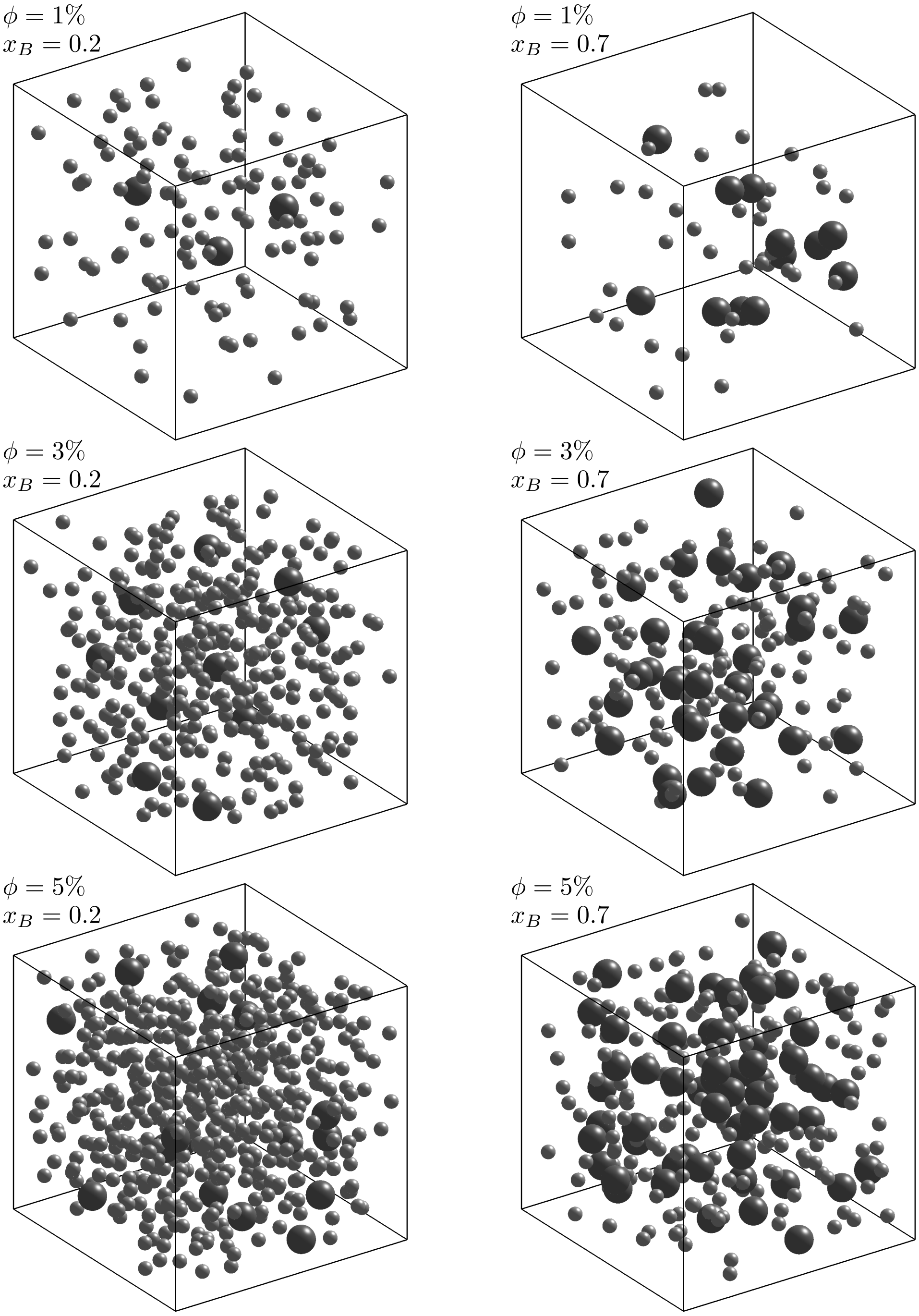

Figure 9–13: Typical computational domains for bidisperse systems. Particle volume fractions of 1, 3 and 5% (top to bottom). Particle B fraction $x_B = 0.2$ (left) and $x_B = 0.7$ (right).

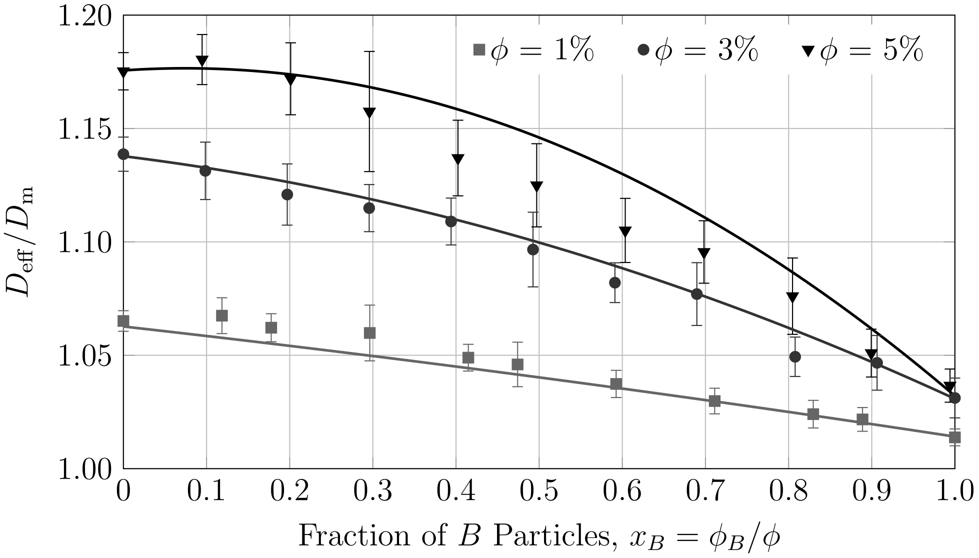

Figure 9–14: Normalized effective mass diffusion coefficient vs. particle fraction (x_B) for nanofliuds at three particle volume fractions. Numerical simulations (symbols), mixing model Eq. (9.14) (lines).

it is presented below in the hope that it will serve as starting point in future studies of polydisperse suspensions.

The mixing model used in Figure 9–14 assumes that the total enhancement due to the motion of the particles can be represented by the sum of the contribution by type A particles plus the contribution by type B particles. From the model in Eq. (9.5) the enhancement due to Brownian motion for type A particles, $E(\phi_A)$, is obtained by removing the parts corresponding to Maxwell's equation.

$$E(\phi_A) = \left[C_1 \mathrm{N}_{\mathrm{BM}} \left(1 + \mathrm{C}_2 \phi_{\mathrm{A}}\right)\right] \phi_A$$

The total enhancement of the bidisperse suspension can be calculated by adding the contributions from both types of particles

$$\frac{D_{\text{eff}}}{D_{\text{m}}} = 1 + B_2\phi + E(\phi_A) + E(\phi_B)$$

This simple approach gives surprisingly good results, considering that no extra parameters were needed. The mixing model gives good estimations of the effective mass diffusivity at low particle volume fractions, $\phi = 1\%$ and $\phi = 3\%$ in Figure 9–14. For higher particles volume fraction the results only capture reasonably well mixtures with high ratios of one type of particle.

If this mixing model was correct, it could be extended to cases of polydisperse suspensions by simply summing the contributions from all particles

$$\frac{D_{\text{eff}}}{D_{\text{m}}} = 1 + B_2\phi + \sum_i E(\phi\ g_i) \tag{9.14}$$

where g_i can be obtained from the particle-size distribution function. It represents the volume fraction of particles of type i in the system. This model is mathematically incorrect, as demonstrated below.

One extreme case that can be used to test the model is the case of a bidisperse suspension with two identical particles, technically monodisperse. The model should reduce to the case of a single type of particle given by Eq. (9.5). Using the definition of $E(\phi_i)$ into Eq. (9.14) gives

$$\frac{D_{\text{eff}}}{D_{\text{m}}} = 1 + B_2\phi + \sum_i \left[C_1 \mathrm{N_{BM}} \left(1 + \mathrm{C_2}\phi\, \mathrm{g_i}\right)\right] \phi\, g_i$$

since $\sum g_i = 1$, this equation can be expressed as

$$\frac{D_{\mathrm{eff}}}{D_{\mathrm{m}}} = 1 + \left[B_2 + C_1\,\mathrm{N_{BM}}\left(1 + \mathrm{C_2}\phi\sum_{\mathrm{i}}\mathrm{g_i^2}\right)\right]\phi$$

For the equation above to be the same as Eq. (9.5) the term $\sum g_i^2$ must be equal to 1, which can only be satisfied if $g_i = 1$ (monodisperse case). Note that $\sum g_i^2$ is always smaller than one for distributions with more than one type of particles. Since this ill-posed mixing model gave satisfactory results when comparing with the results from numerical simulations, it indicates that the magnitude of the interaction term decreases when considering the bidisperse suspensions shown in Figure 9–14.

If the assumption of additive enhancements is correct, then the interaction coefficient C_2 would need to be a function of particle type fraction, such that the following constraint is satisfied for the case of two particles of equal size

$$C_2 = \sum_i C_2^* g_i^2$$

The decrease in the interaction term for bidisperse suspensions was expected, because the smaller and faster moving particles (A) would encounter less often the larger and slower moving ones (B), compared to the cases of particles A interacting with other A particles. This decrease in the interaction term can be visualized in Figure 9–13, where the domains with higher x_B have a smaller number of particles, thus reducing the interaction term. Note that the C_2 coefficient is negative, therefore a decrease in the interaction term implies an increase in the effective mass diffusivity. Therefore, giving values above the interpolation line between the extreme cases, as shown in Figure 9–14. For the case of $\phi = 5\%$ and near $x_B = 0.1$ the numerical results and the mixing model give values larger than the $x_B = 0$ case. The large error bars in the numerical results prevent from drawing strong conclusions about this possible phenomena. Therefore, experimental validation of the existence of this phenomena may be a more viable route at this point.

At the moment, the numerical results available are limited to the ones presented above. A concise study of bidisperse nanofluids and the extension to polydisperse suspensions cannot be continued. These partial results and thoughts are presented here in the hope that they will serve as inspiration for future research, both numerical and experimental.

Part IV

Conclusion

Chapter 10
Conclusions

10.1 Summary

The controversial subject of anomalous increase in thermal conductivity and mass diffusion coefficient in nanofluids was studied using numerical experiments. The main objective was to determine the contribution of Brownian motion-induced micro-convection currents in the enhancement of heat and mass diffusivities in nanoparticle suspensions.

A four-steps numerical model was developed. First, the fluctuating lattice Boltzmann method (fLBM) was used to simulate particle Brownian motion. This is achieved by introducing thermal fluctuations in the fluid collision term. Particles move because of the imbalanced random stresses on the particle surface. These stresses were summarized by storing forces and torques at the center of mass of each particle.

In the second step the multiple relaxation time (MRT) lattice Boltzmann method (LBM) was used to calculate the fluid field, thus providing a field description of Brownian motion-induced micro-convection currents. This was done by moving the particles using the forces and torques from the previous step.

The third step uses the finite volume method (FVM) to describe the evolution of a scalar field (temperature or concentration) over time, given the fluid flow field representing the micro-convection currents. The mismatch of the velocity grids between LBM and FVM led to the proposition of the hybrid LBM-FVM, which satisfies mass conservation in both LBM and FVM grids.

Finally, the overwhelming amount of information obtained from these simulations was summarized by averaging the scalar fields to obtain a macroscopic view of the problem, where the fluid-particle system can be viewed as an homogeneous system at rest. Two averaging methods were proposed and used in the analysis. First, the fixed gradient method was based on Fourier's law for heat transfer or Fick's law for mass transfer as the macroscopic views of the system. This method was used in the study of heat transfer, but was found to be impractical for the study of mass transfer.

The second averaging method developed was the Gaussian pulse method. In this method the evolution of a Gaussian pulse is tracked over time. The increase in the pulse variance was then used to estimate the effective thermal conductivity or effective mass diffusion coefficient. This method was found to be practical for studying heat and mass transfer phenomena in nanofluids, thus overcoming some of the drawbacks of the fixed gradient method. One important limitation of this method is that the macroscopic view of the system is obtained by sampling the domain with different Gaussian pulses, thus increasing the computational effort compared to the fixed gradient method.

Some interesting applications were studied using the numerical methodology developed. First, heat and mass transfer in composite materials were studied. This was done as a part of model validation. Both methods (fixed gradient and Gaussian pulse) reproduce Maxwell's equation for composite materials. Some limitations of the Gaussian pulse method were discussed. In particular, short mass transfer simulations would give the proper tendency but the effective mass diffusion coefficient would be biased towards the value of molecular mass diffusivity.

Heat diffusion phenomena was studied using both averaging methods. The same conclusions were reached with both methods, indicating that micro-convection currents generated by particle Brownian motion are not significant enough to justify any anomalous increases in thermal conductivity with particle volume fraction.

The case of mass transfer in nanofluids was studied in more detail. Only the Gaussian pulse method was used in these studies. The results indicate that the abnormal increase in the mass diffusivity observed experimentally can be explained by the presence of Brownian motion-induced micro-convection currents. However, the numerical model cannot explain the 10 fold increased or the location of the maximum observed experimentally (Veilleux and Coulombe, 2010b). The numerical model, however, predicts the nonlinear increase with particle volume fraction.

A parametric study was performed to determine the dependency of the effective mass diffusivity on different variables. A simplified model was then constructed to summarize the findings. A new dimensionless number was proposed, N_{BM}, defined as the ratio of the Brownian diffusion coefficient over the molecular diffusion coefficient. The simplified model is composed of three terms: 1) Maxwell's equation simplified for the case of zero diffusivity inside the particles, 2) the contribution by Brownian motion describe by the $\mathrm{N_{BM}}$ number, and 3) the nanoparticle interaction term, which is a decreasing function with particle volume fraction. The $\mathrm{N_{BM}}$ number captures the dependencies of the effective diffusion coefficient with fluid and particle properties: inversely proportional to particle size, viscosity, fluid density, and proportional to temperature. One interesting finding is that the effective mass diffusivity is independent of particle density.

The simplified model was used to explain the experimental results from (Veilleux and Coulombe, 2010b). It was assumed that the simplified model gives the proper form but the coefficients could be different. These were then determined by curve fitting the experimental data available. Two hypothesis were considered to explain the sharp decrease after $\phi = 2\%$ observed experimentally. First, agglomeration can increase the effective particle diameter thus decreasing $\mathrm{N_{BM}}$ and the effective mass diffusivity. The second hypothesis highlights the need for a better understanding of particle interaction. In this case the interaction term would decrease to a point where the Brownian contribution is negligible (particle hindering), thus decreasing the effective mass diffusivity. Confirmation of either hypothesis requires experimentation, for which the simplified model proposed can provide guidelines for the experiments to be perform.

The simplified model was then rewritten in terms of the Péclet number to highlight the relationship with Taylor dispersion. This led to the relationship between the $\mathrm{N_{BM}}$ and Pe numbers, which also includes the the Sc number and the momentum interaction parameter (density ratio). Extending the simplified model to the case of heat transfer suggests that the dispersion contribution to the effective thermal conductivity would be negligible compared to the other terms of the equation. Therefore, the abnormal enhancements reported in the literature cannot be explained by Brownian motion-induced micro-convection currents.

The final application studied using the numerical methodology introduced in this work was the case of bidisperse nanofluids. The objective was to attempt to extend the analysis to polydisperse suspensions. The relationship between the effective mass diffusivity and the fraction of particles of a given size was found to be nonlinear. Due to the limited data available, this study was left open as an incentive for future studies towards understanding the effective properties of polydisperse nanofluids.

In summary, the study of the bidisperse system highlights the importance of the interaction term. For polydisperse suspensions, this term needs to account for all interactions between particles, both for equal and different sizes. In general, the interaction term is expected to decrease for polydisperse suspensions, compared to monodisperse suspensions. This decrease explains the deviation from a linear mixing rule and also introduces the possibility of encountering effective mass diffusion coefficients for polydisperse suspensions that are larger than the monodisperse case with the smaller particle; though, strong evidence of this phenomenon has not been confirmed.

10.2 Original Contributions

The following original contributions to the field of heat and mass transport phenomena in nanofluids were done as part of this project.

1. A new model capable of resolving fluid flow at the microscale was proposed and developed. The model is based on the LBM and can be used to calculate micro-convection currents around nanoparticles.
2. A variation of the hybrid LBM-FVM was proposed. In this new approach the staggered velocity field in the FVM is calculated directly from the distributions from the LBM. The main advantage of this method is that the continuity equation is satisfied in both grids, LBM and FVM.
3. Two methods for estimating macroscopic or effective heat and mass diffusivities for composite materials were proposed and validated: a) fixed gradient method and b) Gaussian pulse method. Important limitations for each of these methods were discussed.
4. The three previous contributions together constitute the main work of this project, a numerical model to study the contribution of Brownian motion-induced micro-convection currents on the effective heat and mass diffusivities in nanofluids.
5. In the field of heat transfer in nanofluids, the results from this study supports the theory that Brownian motion-induced micro-convection currents are not

significant enough to justify any abnormal enhancement. This conclusion confirms the generally accepted view that the heat diffusivity of nanofluids is not abnormal and in fact, it is well-predicted by Maxwell's model.

6. A simplified model was proposed to explain the abnormal enhancement of the mass transfer coefficient in nanofluids. In this case, the presence of micro-convection currents could explain the values higher than the Maxwell's model prediction reported by other researchers. The simplified model also introduced a new dimensionless quantity, $\mathrm{N_{BM}}$, believed to play an important role when studying mass transfer in nanofluids. It indicates that dispersion plays an important role in the enhancement, while particle density does influence mass diffusivity.
7. The methodology developed in this work was also applied to study bidisperse system. The development and discussion on this subject are only preliminary. Partial results were presented in this work with the objective of highlighting the importance of the particle interaction term when studying effective diffusion coefficients of polydisperes suspensions.

10.3 Recommendations for Future Work

The studies performed as part of this project were done based on a very specific numerical model where many phenomena are ignored. As it is usual with numerical studies, they require to be validated by extensive experimental measurements. Validation of the current model requires work in two fronts: parameters dependency (particle size, particle density, fluid viscosity and temperature) and particle interaction. The relationships identified in Eq. (9.5) could be used as a guide for designing experiments to study the dependency of mass diffusivity on the parameters listed above.

Besides the need for extensive experimental measurements, the following suggestions are made to extend and improve the work started in this project:

1. Proper validation of the LBM for estimation of micro-convection currents is needed. Some of the assumptions that need to be verified are: the no-slip condition used at the particle surface and the use of a slightly compressible model to describe the fluid field. The current model should be extended by using the incompressible LBM and by considering different slip factors. The incentive for performing this validation is that the numerical model used may suffer of numerical viscosity, thus the simulation may behave as if the viscosity was higher than the value set. This would affect the micro-convection currents calculated by the LBM, thus potentially explaining why the effective mass diffusivity calculated from the numerical model were smaller than the experimental observations.
2. The fLBM can be improved by implementing periodic boundaries for the particles. This should reduce the variability observed throughout the simulations, because the gap near the boundaries would no longer be needed. This would in turn produce a more homogeneous view of the computational domain.

3. Implementation of the lubrication approximation (Dünweg and Ladd, 2009) for cases when particles are close to each other is highly recommended. Besides allowing the current methodology to be used for higher particle volume fractions, it may also explain the experimentally-observed decrease of the effective mass diffusivity with particle volume fraction (Veilleux and Coulombe, 2010b). A better description of the interaction term could be obtained if the lubrication approximation was implemented.
4. One of the main limitations in the numerical method presented in this work is the FVM. In some cases the central-difference scheme used for discretizing the diffusion-convection equation was unstable, giving oscillations in the concentration field. The suggestion here is to use a different discretization scheme such as the Flux-corrected transport (Kuzmin et al., 2005). This improvement should help to extend the analysis to higher temperatures and oddly enough, this may allow for studying suspensions of particles with larger densities than the ones considered in this work.
5. The preliminary study of bidisperse suspensions presented in this dissertation is only a small fraction of the work needed in this subject. A vast number of simulations with different conditions would be the first step, followed by an analysis focussed on the interaction term. Ideally, the results from this analysis should be extendable to describe polydisperse suspensions. The direct simulation of polydisperse suspensions with the current model should also be considered.

Bibliography

Ahuja, A. S. (1975). Augmentation of heat transport in laminar-flow of polystyrene suspensions .2. analysis of data. *Journal of Applied Physics*, 46(8):3417–3425.

Ahuja, A. S. (1976). Augmentation of heat and mass-transport in flowing particle suspensions - dimensional analysis. *Journal of Applied Physics*, 47(2):775–777.

Ahuja, A. S. (1980). Augmentation of heat and mass-transfer in laminar-flow of suspensions - correlation of data. *Journal of Applied Physics*, 51(1):791–795.

Akoh, H., Tsukasaki, Y., Yatsuya, S., and Tasaki, A. (1978). Magnetic properties of ferromagnetic ultrafine particles prepared by vacuum evaporation on running oil substrate. *Journal of Crystal Growth*, 45:495–500.

Ali, A., Vafai, K., and Khaled, A. R. A. (2004). Analysis of heat and mass transfer between air and falling film in a cross flow configuration. *International Journal of Heat and Mass Transfer*, 47(4):743–755.

Ashrafmansouri, S.-S. and Nasr Esfahany, M. (2014). Mass transfer in nanofluids: A review. *International Journal of Thermal Sciences*, 82(0):84–99.

Babaei, H., Keblinski, P., and Khodadadi, J. M. (2013). A proof for insignificant effect of brownian motion-induced micro-convection on thermal conductivity of nanofluids by utilizing molecular dynamics simulations. *Journal of Applied Physics*, 113(8).

Banerjee, A. and Kihm, K. D. (2005). Experimental verification of near-wall hindered diffusion for the brownian motion of nanoparticles using evanescent wave microscopy. *Physical Review E*, 72(4).

Barbes, B., Paramo, R., Blanco, E., and Casanova, C. (2014). Thermal conductivity and specific heat capacity measurements of cuo nanofluids. *Journal of Thermal Analysis and Calorimetry*, 115(2):1883–1891.

Batchelor, G. K. (1972). Sedimentation in a dilute dispersion of spheres. *Journal of Fluid Mechanics*, 52:245–68.

Batchelor, G. K. (1976). Brownian diffusion of particles with hydrodynamic interaction. *Journal of Fluid Mechanics*, 74:1–29.

Benzi, R., Succi, S., and Vergassola, M. (1992). The lattice boltzmann-equation - theory and applications. *Physics Reports-Review Section of Physics Letters*, 222(3):145–197.

Bhattacharya, P., Nara, S., Vijayan, P., Tang, T., Lai, W., Phelan, P. E., Prasher, R. S., Song, D. W., and Wang, J. (2006). Characterization of the temperature oscillation technique to measure the thermal conductivity of fluids. *International Journal of Heat and Mass Transfer*, 49(17-18):2950–2956.

Bhattacharya, P., Saha, S. K., Yadav, A., Phelan, P. E., and Prasher, R. S. (2004). Brownian dynamics simulation to determine the effective thermal conductivity of nanofluids. *Journal of Applied Physics*, 95(11 I):6492–6494.

Bonnecaze, R. T. and Brady, J. F. (1990). A method for determining the effective conductivity of dispersions of particles. *Proceedings of the Royal Society of London, Series A (Mathematical and Physical Sciences)*, 430(1879):285–313.

Bonnecaze, R. T. and Brady, J. F. (1991). The effective conductivity of random suspensions of spherical particles. *Proceedings of the Royal Society of London, Series A (Mathematical and Physical Sciences)*, 432(1886):445–65.

Boris, J. P. (2013). Flux-corrected transport looks at forty. *Computers & Fluids*, 84:113–126.

Branson, B. T., Beauchamp, P. S., Beam, J. C., Lukehart, C. M., and Davidson, J. L. (2013). Nanodiamond nanofluids for enhanced thermal conductivity. *ACS Nano*, 7(4):3183–9.

Buongiorno, J., Venerus, D. C., Prabhat, N., McKrell, T., Townsend, J., Christianson, R., Tolmachev, Y. V., Keblinski, P., Hu, L. W., Alvarado, J. L., Bang, I. C., Bishnoi, S. W., Bonetti, M., Botz, F., Cecere, A., Chang, Y., Chen, G., Chen, H. S., Chung, S. J., Chyu, M. K., Das, S. K., Di Paola, R., Ding, Y. L., Dubois, F., Dzido, G., Eapen, J., Escher, W., Funfschilling, D., Galand, Q., Gao, J. W., Gharagozloo, P. E., Goodson, K. E., Gutierrez, J. G., Hong, H. P., Horton, M., Hwang, K. S., Iorio, C. S., Jang, S. P., Jarzebski, A. B., Jiang, Y. R., Jin, L. W., Kabelac, S., Kamath, A., Kedzierski, M. A., Kieng, L. G., Kim, C., Kim, J. H., Kim, S., Lee, S. H., Leong, K. C., Manna, I., Michel, B., Ni, R., Patel, H. E., Philip, J., Poulikakos, D., Reynaud, C., Savino, R., Singh, P. K., Song, P. X., Sundararajan, T., Timofeeva, E., Tritcak, T., Turanov, A. N., Van Vaerenbergh, S., Wen, D. S., Witharana, S., Yang, C., Yeh, W. H., Zhao, X. Z., and Zhou, S. Q. (2009). A benchmark study on the thermal conductivity of nanofluids. *Journal of Applied Physics*, 106(9):–.

Chen, H. D. (1998). Volumetric formulation of the lattice boltzmann method for fluid dynamics: Basic concept. *Physical Review E*, 58(3):3955–3963.

Choi, S. U. S. (1995). Enhancing thermal conductivity of fluids with nanoparticles. In *1995 International Mechanical Engineering Congress and Exhibition*, volume 231 of *American Society of Mechanical Engineers, Fluids Engineering Division (Publication) FED*, pages 99–105, San Francisco, CA, USA.

Choi, S. U. S., Zhang, Z. G., Yu, W., Lockwood, F. E., and Grulke, E. A. (2001). Anomalous thermal conductivity enhancement in nanotube suspensions. *Applied Physics Letters*, 79(14):2252–4.

Chon, C. H., Kihm, K. D., Lee, S. P., and Choi, S. U. S. (2005). Empirical correlation finding the role of temperature and particle size for nanofluid (al2o3) thermal conductivity enhancement. *Applied Physics Letters*, 87(15):153107.

Coulombe, S. and Tavares, J. (2007). Organic nanofluids, method and reactor for synthesis and thereof.

Cui, T., Xuan, Y., and Li, Q. (2012). Simulation of enhancement of mass transfer in nano-fluids by lattice boltzmann method. *CIESC Journal*, 63(S1):41–46.

Culbertson, C. T., Jacobson, S. C., and Ramsey, J. M. (2002). Diffusion coefficient measurements in microfluidic devices. *Talanta*, 56(2):365–373.

Das, S. K., Choi, S. U. S., and Patel, H. E. (2006). Heat transfer in nanofluids - a review. *Heat Transfer Engineering*, 27(10):3–19.

Das, S. K., Putra, N., and Roetzel, W. (2003a). Pool boiling characteristics of nano-fluids. *International Journal of Heat and Mass Transfer*, 46(5):851–62.

Das, S. K., Putra, N., Thiesen, P., and Roetzel, W. (2003b). Temperature dependence of thermal conductivity enhancement for nanofluids. *Journal of Heat Transfer-Transactions of the Asme*, 125(4):567–574.

Daungthongsuk, W. and Wongwises, S. (2007). A critical review of convective heat transfer of nanofluids. *Renewable and Sustainable Energy Reviews*, 11(5):797–817.

Davis, R. H. (1986). The effective thermal conductivity of a composite material with spherical inclusions. *International Journal of Thermophysics*, 7(3):609–620.

d'Humieres, D., Ginzburg, I., Krafczyk, M., Lallemand, P., and Luo, L.-S. (2002). Multiple-relaxation-time lattice boltzmann models in three dimensions. *Philosophical Transactions: Mathematical, Physical and Engineering Sciences*, 360(1792):437–451.

Ding, Y. L., Alias, H., Wen, D. S., and Williams, R. A. (2006). Heat transfer of aqueous suspensions of carbon nanotubes (cnt nanofluids). *International Journal of Heat and Mass Transfer*, 49(1-2):240–250.

Dünweg, B. and Ladd, A. (2009). Lattice boltzmann simulations of soft matter systems. In *Advanced Computer Simulation Approaches for Soft Matter Sciences III*, Advances in Polymer Science, pages 89–166. Springer-Verlag, Berlin.

Dünweg, B., Schiller, U. D., and Ladd, A. J. C. (2007). Statistical mechanics of the fluctuating lattice boltzmann equation. *Physical Review E*, 76(3):036704.

Eapen, J., Williams, W. C., Buongiorno, J., Hu, L.-W., Yip, S., Rusconi, R., and Piazza, R. (2007). Mean-field versus microconvection effects in nanofluid thermal conduction. *Physical Review Letters*, 99(9):095901.

Eastman, J. A., Choi, S. U. S., Li, S., Yu, W., and Thompson, L. J. (2001). Anomalously increased effective thermal conductivities of ethylene glycol-based nanofluids containing copper nanoparticles. *Applied Physics Letters*, 78(6):718–720.

Eastman, J. A., Choi, U. S., Li, S., Thompson, L. J., and Lee, S. (1997). Enhanced thermal conductivity through the development of nanofluids. In *1996 MRS Fall Meeting*, volume 457 of *Materials Research Society Symposium - Proceedings*, pages 3–11, Boston, MA, USA.

Einstein, A. (1905). The motion of elements suspended in static liquids as claimed in the molecular kinetic theory of heat. *Annalen Der Physik*, 17(8):549–560.

Fan, L. S., Hemminger, O., Yu, Z., and Wang, F. (2007). Bubbles in nanofluids. *Industrial and Engineering Chemistry Research*, 46(12):4341–4346.

Fang, X. P., Xuan, Y. M., and Li, Q. (2009). Experimental investigation on enhanced mass transfer in nanofluids. *Applied Physics Letters*, 95(20).

Feichtinger, C. (2012). *Design and Performance Evaluation of a Software Framework for Multi-Physics Simulations on Heterogeneous Supercomputers*. Ph.d. thesis, University of Erlangen-Nuremberg.

Fricke, H. (1924). A mathematical treatment of the electrical conductivity of colloids and cell suspensions. *Journal of General Physiology*, 6(4):375–384.

Gerardi, C., Cory, D., Buongiorno, J., Hu, L. W., and McKrell, T. (2009). Nuclear magnetic resonance-based study of ordered layering on the surface of alumina nanoparticles in water. *Applied Physics Letters*, 95(25).

Haarman, J. W. (1971). Contribution to theory of transient hot-wire method. *Physica*, 52(4):605–619.

Hamilton, R. L. and Crosser, O. K. (1962). Thermal conductivity of heterogeneous two-component systems. *Industrial and Engineering Chemistry, Fundamentals*, 1(3):187–191.

Hansen, J.-P. and McDonald, I. R. (2006). *Theory of simple liquids.* Elsevier Academic Press, London ; Burlington, MA, 3rd edition.

He, P. and Qiao, R. (2008). Self-consistent fluctuating hydrodynamics simulations of thermal transport in nanoparticle suspensions. *Journal of Applied Physics*, 103(9):094305–6.

Healy, J. J., Degroot, J. J., and Kestin, J. (1976). Theory of transient hot-wire method for measuring thermal conductivity. *Physica B & C*, 82(2):392–408.

Heris, S. Z., Esfahany, M. N., and Etemad, G. (2007). Numerical investigation of nanofluid laminar convective heat transfer through a circular tube. *Numerical Heat Transfer Part a-Applications*, 52(11):1043–1058.

Hong, T.-K., Yang, H.-S., and Choi, C. J. (2005). Study of the enhanced thermal conductivity of fe nanofluids. *Journal of Applied Physics*, 97(6):064311.

Huang, H. B., Lee, T. S., and Shu, C. (2007). Hybrid lattice boltzmann finite-difference simulation of axisymmetric swirling and rotating flows. *International Journal for Numerical Methods in Fluids*, 53(11):1707–1726.

Huang, J. J., Shu, C., Feng, J. J., and Chew, Y. T. (2012). A phase-field-based hybrid lattice-boltzmann finite-volume method and its application to simulate droplet motion under electrowetting control. *Journal of Adhesion Science and Technology*, 26(12-17):1825–1851.

IAPWS (1997). Revised Release on the IAPS Formulation 1985 for the Viscosity of Ordinary Water Substance, 15. Technical report, International Association for the Properties of Water and Steam.

IAPWS (1998). Revised Release on the IAPS Formulation 1985 for the Thermal Conductivity of Ordinary Water Substance, 23. Technical report, International Association for the Properties of Water and Steam.

Iglberger, K., Thurey, N., and Rude, U. (2008). Simulation of moving particles in 3d with the lattice boltzmann method. *Computers & Mathematics with Applications*, 55(7):1461–1468.

Jang, S. P. and Choi, S. U. S. (2007). Effects of various parameters on nanofluid thermal conductivity. *Transactions of the ASME. Journal of Heat Transfer*, 129(5):617–23.

Jeffrey, D. J. (1973). Conduction through a random suspension of spheres. *Proceedings of the Royal Society of London. Series A, Mathematical and Physical Sciences*, 335(1602):355–367.

Joshi, H., Agarwal, A., Puranik, B., Shu, C., and Agrawal, A. (2010). A hybrid fvm-lbm method for single and multi-fluid compressible flow problems. *International Journal for Numerical Methods in Fluids*, 62(4):403–427.

Keblinski, P., Eastman, J. A., and Cahill, D. G. (2005). Nanofluids for thermal transport. *Materials Today*, 8(6):36–44.

Keblinski, P., Phillpot, S. R., Choi, S. U. S., and Eastman, J. A. (2002). Mechanisms of heat flow in suspensions of nano-sized particles (nanofluids). *International Journal of Heat and Mass Transfer*, 45(4):855–863.

Keblinski, P. and Thomin, J. (2006). Hydrodynamic field around a brownian particle. *Physical Review E - Statistical, Nonlinear, and Soft Matter Physics*, 73(1):010502.

Kestin, J., Sengers, J. V., KamgarParsi, B., and Sengers, J. M. H. L. (1984). Thermophysical properties of fluid h2o. *Journal of Physical and Chemical Reference Data*, 13(1):175–183.

Khiabani, R. H., Joshi, Y., and Aidun, C. K. (2010). Heat transfer in microchannels with suspended solid particles: Lattice-boltzmann based computations. *Journal of Heat Transfer-Transactions of the Asme*, 132(4).

Koo, J. and Kleinstreuer, C. (2004). A new thermal conductivity model for nanofluids. *Journal of Nanoparticle Research*, 6(6):577–88.

Köstler, H. (2011). A robust geometric multigrid solver within the walberla framework. In *15th Copper Mountain Conference on Multigrid Methods*, Copper Mountain, Colorado, USA.

Krishnamurthy, S., Bhattacharya, P., Phelan, P. E., and Prasher, R. S. (2006). Enhanced mass transport in nanofluids. *Nano Letters*, 6(3):419–23.

Kumar, D. H., Patel, H. E., Kumar, V. R. R., Sundararajan, T., Pradeep, T., and Das, S. K. (2004). Model for heat conduction in nanofluids. *Physical Review Letters*, 93(14):144301.

Kuzmin, D., Löhner, R., and Turek, S. (2005). Flux-corrected transport principles, algorithms, and applications.

Kwak, K. and Kim, C. (2005). Viscosity and thermal conductivity of copper oxide nanofluid dispersed in ethylene glycol. *Korea-Australia Rheology Journal*, 17(2):35–40.

Ladd, A. J. C. (1993). Short-time motion of colloidal particles - numerical-simulation via a fluctuating lattice-boltzmann equation. *Physical Review Letters*, 70(9):1339–1342.

Ladd, A. J. C. (1994a). Numerical simulations of particulate suspensions via a discretized boltzmann-equation .1. theoretical foundation. *Journal of Fluid Mechanics*, 271:285–309.

Ladd, A. J. C. (1994b). Numerical simulations of particulate suspensions via a discretized boltzmann-equation .2. numerical results. *Journal of Fluid Mechanics*, 271:311–339.

Lallemand, P. and Luo, L.-S. (2003). Theory of the lattice boltzmann method: Acoustic and thermal properties in two and three dimensions. *Physical Review E*, 68(3):036706.

Landau, L. D. and Lifshitz, E. M. (1959). *Fluid mechanics*. Course of theoretical physics. Pergamon Press, Oxford.

Lee, K. J., Yoon, S.-H., and Jang, J. (2007). Carbon nanofibers: A novel nanofiller for nanofluid applications. *Small*, 3(7):1209–1213.

Leong, K. C., Yang, C., and Murshed, S. M. S. (2006). A model for the thermal conductivity of nanofluids - the effect of interfacial layer. *Journal of Nanoparticle Research*, 8(2):245–254.

Li, F. C., Yang, J. C., Zhou, W. W., He, Y. R., Huang, Y. M., and Jiang, B. C. (2013). Experimental study on the characteristics of thermal conductivity and shear viscosity of viscoelastic-fluid-based nanofluids containing multiwalled carbon nanotubes. *Thermochimica Acta*, 556:47–53.

Li, J., Li, Z., and Wang, B. (2002). Experimental viscosity measurements for copper oxide nanoparticle suspensions. *Tsinghua Science and Technology*, 7(2):198–201.

Li, Z., Yang, M., and Zhang, Y. (2014). Hybrid lattice boltzmann and finite volume method for natural convection. *Journal of Thermophysics and Heat Transfer*, 28(1):68–77.

Liu, K. V., Choi, U. S., and Kasza, K. E. (1988). Measurements of pressure drop and heat transfer in turbulent pipe flows of particulate slurries. Technical Report ANL-88-15, Argonne National Lab., IL (USA).

Lo, C.-H., Tsung, T.-T., and Chen, L.-C. (2005). Shape-controlled synthesis of cu-based nanofluid using submerged arc nanoparticle synthesis system (sanss). *Journal of Crystal Growth*, 277(1-4):636–642.

Lowe, C. P. and Frenkel, D. (1996). Short-time dynamics of colloidal suspensions. *Physical Review E*, 54(3):2704–2713.

Luan, H. B., Xu, H., Chen, L., Feng, Y. L., He, Y. L., and Tao, W. Q. (2012). Coupling of finite volume method and thermal lattice boltzmann method and its application to natural convection. *International Journal for Numerical Methods in Fluids*, 70(2):200–221.

Mao, C., Zou, H. F., Zhou, X., Huang, Y., Gan, H. Y., and Zhou, Z. X. (2014). Analysis of suspension stability for nanofluid applied in minimum quantity lubricant grinding. *International Journal of Advanced Manufacturing Technology*, 71(9-12):2073–2081.

Marble, F. E. (1963). Dynamics of a gas containing small solid particles. In *Combustion and Propulsion (5th AGARDograph Colloquium)*, pages 175–213. Pergamon Press, New York.

Marín, E., Bedoya, A., Alvarado, S., Calderón, A., Ivanov, R., and Gordillo-Delgado, F. (2014). An explanation for anomalous thermal conductivity behaviour in nanofluids as measured using the hot-wire technique. *Journal of Physics D: Applied Physics*, 47(8):085501.

Masuda, H., Ebata, A., Teramae, K., and Hishinuma, N. (1993). Alteration of thermal conductivity and viscosity of liquid by dispersion ultra-fine particles (dispersion of gama-al2o3, sio2, and tio2 ultra-fine particles). *Nesu Bussei*, 4(4):227–233.

Maxwell, J. C. (1873). *A treatise on electricity and magnetism.* Oxford University Press, London, 1 edition.

Maxwell, J. C. (1892). *A treatise on electricity and magnetism.* Oxford University Press, London, 3 edition.

Mazo, R. M. (2002). *Brownian motion : fluctuations, dynamics, and applications.* Clarendon ; Oxford University Press, Oxford New York.

Mehra, A. (1988). Intensification of multiphase reactions through the use of a microphase - i. theoretical. *Chemical Engineering Science*, 43(4):899–912.

Michaelides, E. E. (2014). *Nanofluidics.* Thermodynamic and Transport Properties. Springer International Publishing.

Mondal, B. and Mishra, S. C. (2009a). The lattice boltzmann method and the finite volume method applied to conduction-radiation problems with heat flux boundary conditions. *International Journal for Numerical Methods in Engineering*, 78(2):172–195.

Mondal, B. and Mishra, S. C. (2009b). Simulation of natural convection in the presence of volumetric radiation using the lattice boltzmann method. *Numerical Heat Transfer Part a-Applications*, 55(1):18–41.

Mondal, B., Mishra, S. C., Asinari, P., and Borchiellini, R. (2008). Analysis of a localized fire in a 3-d tunnel using a hybrid solver: Lattice boltzmann method, finite-volume method, and fully explicit upwind scheme. *Numerical Heat Transfer Part a-Applications*, 53(4):392–417.

Myers, T. G., MacDevette, M. M., and Ribera, H. (2013). A time-dependent model to determine the thermal conductivity of a nanofluid. *Journal of Nanoparticle Research*, 15(7).

Nagasaka, Y. and Nagashima, A. (1981). Absolute measurement of the thermal-conductivity of electrically conducting liquids by the transient hot-wire method. *Journal of Physics E-Scientific Instruments*, 14(12):1435–1440.

Nan, C. W., Birringer, R., Clarke, D. R., and Gleiter, H. (1997). Effective thermal conductivity of particulate composites with interfacial thermal resistance. *Journal of Applied Physics*, 81(10):6692–6699.

Neumann, P. (2008). *Numerical simulation of nanoparticles in Brownian motion using the lattice Boltzmann method.* Master's thesis, University of Erlangen-Nuremberg.

Nomura, S. and Chou, T.-W. (1986). Heat conduction in composite materials due to oscillating temperature field. *International Journal of Engineering Science*, 24(5):643–647.

Olle, B., Bucak, S., Holmes, T. C., Bromberg, L., Hatton, T. A., and Wang, D. I. C. (2006). Enhancement of oxygen mass transfer using functionalized magnetic nanoparticles. *Industrial and Engineering Chemistry Research*, 45(12):4355–4363.

Ozerinc, S., Kakac, S., and Yazicioglu, A. G. (2010). Enhanced thermal conductivity of nanofluids: a state-of-the-art review. *Microfluidics and Nanofluidics*, 8(2):145–170.

Ozturk, S., Hassan, Y. A., and Ugaz, V. M. (2010). Interfacial complexation explains anomalous diffusion in nanofluids. *Nano Letters*, 10(2):665–671.

Patankar, S. V. (1980). *Numerical heat transfer and fluid flow*. Series in computational methods in mechanics and thermal sciences. Routledge, Taylor & Francis Group, New York.

Peng, G. W., Xi, H. W., Duncan, C., and Chou, S. H. (1998). Lattice boltzmann method on irregular meshes. *Physical Review E*, 58(4):R4124–R4127.

Prasher, R., Bhattacharya, P., and Phelan, P. E. (2005). Thermal conductivity of nanoscale colloidal solutions (nanofluids). *Physical Review Letters*, 94(2):025901.

Prasher, R., Evans, W., Meakin, P., Fish, J., Phelan, P., and Keblinski, P. (2006a). Effect of aggregation on thermal conduction in colloidal nanofluids. *Applied Physics Letters*, 89(14):143119–1.

Prasher, R., Phelan, P. E., and Bhattacharya, P. (2006b). Effect of aggregation kinetics on the thermal conductivity of nanoscale colloidal solutions (nanofluid).

Nano Letters, 6(7):1529–1534.

Prasher, R., Song, D., Jinlin, W., and Phelan, P. (2006c). Measurements of nanofluid viscosity and its implications for thermal applications. *Applied Physics Letters*, 89(13):133108–1.

Putnam, S. A., Cahill, D. G., Braun, P. V., Ge, Z. B., and Shimmin, R. G. (2006). Thermal conductivity of nanoparticle suspensions. *Journal of Applied Physics*, 99(8):–.

Qiao, R. and He, P. (2007). Simulation of heat conduction in nanocomposite using energy-conserving dissipative particle dynamics. *Molecular Simulation*, 33(8):677–683.

Rusconi, R., Rodari, E., and Piazza, R. (2006). Optical measurements of the thermal properties of nanofluids. *Applied Physics Letters*, 89(26):261916.

Santucci, A. and Verdini, L. (1986). Data-acquisition system for measurement of thermal diffusivity and propagation properties of thermal waves by non-steady-state method. *Review of Scientific Instruments*, 57(8):1627–32.

Sarkar, S. and Selvam, R. P. (2007). Molecular dynamics simulation of effective thermal conductivity and study of enhanced thermal transport mechanism in nanofluids. *Journal of Applied Physics*, 102(7):074302–7.

Sohn, C. W. and Chen, M. M. (1981). Microconvective thermal-conductivity in disperse 2-phase mixtures as observed in a low velocity couette-flow experiment. *Journal of Heat Transfer-Transactions of the Asme*, 103(1):47–51.

Subba-Rao, V., Hoffmann, P. M., and Mukhopadhyay, A. (2011). Tracer diffusion in nanofluids measured by fluorescence correlation spectroscopy. *Journal of Nanoparticle Research*, 13(12):6313–6319.

Succi, S. (2001). *The lattice Boltzmann equation for fluid dynamics and beyond*. Numerical mathematics and scientific computation. Clarendon Press ; Oxford University Press, Oxford New York.

Taha-Tijerina, J. J., Narayanan, T. N., Tiwary, C. S., Lozano, K., Chipara, M., and Ajayan, P. M. (2014). Nanodiamond-based thermal fluids. *Acs Applied Materials & Interfaces*, 6(7):4778–4785.

Taylor, G. (1953). Dispersion of soluble matter in solvent flowing slowly through a tube. *Proceedings of the Royal Society of London Series a-Mathematical and Physical Sciences*, 219(1137):186–203.

Taylor, R., Coulombe, S., Otanicar, T., Phelan, P., Gunawan, A., Lv, W., Rosengarten, G., Prasher, R., and Tyagi, H. (2013). Small particles, big impacts: A review of the diverse applications of nanofluids. *Journal of Applied Physics*, 113(1).

Turanov, A. N. and Tolmachev, Y. V. (2009). Heat- and mass-transport in aqueous silica nanofluids. *Heat and Mass Transfer*, 45(12):1583–1588.

Tzou, D. Y. (2008). Instability of nanofluids in natural convection. *Journal of Heat Transfer*, 130(7):072401–9.

Ubertini, S., Bella, G., and Succi, S. (2003). Lattice boltzmann method on unstructured grids: Further developments. *Physical Review E*, 68(1):–.

Veilleux, J. (2010). The hydrodynamics of mass diffusion enhancement in nanofluids.

Veilleux, J. and Coulombe, S. (2010a). Mass diffusion coefficient measurements at the microscale: Imaging a transient concentration profile using tirf microscopy. *International Journal of Heat and Mass Transfer*, 53(23-24):5321–5329.

Veilleux, J. and Coulombe, S. (2010b). A total internal reflection fluorescence microscopy study of mass diffusion enhancement in water-based alumina nanofluids. *Journal of Applied Physics*, 108(10).

Veilleux, J. and Coulombe, S. (2011). A dispersion model of enhanced mass diffusion in nanofluids. *Chemical Engineering Science*, 66(11):2377–2384.

Venerus, D. C., Kabadi, M. S., Lee, S., and Perez-Luna, V. (2006). Study of thermal transport in nanoparticle suspensions using forced rayleigh scattering. *Journal of Applied Physics*, 100(9):094310.

Versteeg, H. K. and Malalasekera, W. (1995). *An introduction to computational fluid dynamics : the finite volume method*. Wiley, New York.

Wagner, W. and Pruss, A. (2002). The iapws formulation 1995 for the thermodynamic properties of ordinary water substance for general and scientific use. *Journal of Physical and Chemical Reference Data*, 31(2):387–535.

Wang, X., Xu, X., and Choi, S. U. S. (1999). Thermal conductivity of nanoparticle-fluid mixture. *Journal of Thermophysics and Heat Transfer*, 13(4):474–480.

Wang, X.-Q. and Mujumdar, A. S. (2007). Heat transfer characteristics of nanofluids: a review. *International Journal of Thermal Sciences*, 46(1):1–19.

Wen, J. P., Jia, X. Q., and Feng, W. (2005). Hydrodynamic and mass transfer of gas-liquid-solid three-phase internal loop airlift reactors with nanometer solid particles. *Chemical Engineering and Technology*, 28(1):53–60.

Wu, X. and Kumar, R. (2005). Investigation of natural convection in nanofluids by lattice boltzmann method. In *ASME 2005 Summer Heat Transfer Conference collocated with the ASME 2005 Pacific Rim Technical Conference and Exhibition on Integration and Packaging of MEMS, NEMS, and Electronic Systems*, pages 2319–2326, San Francisco, CA.

Xi, H. W., Peng, G. W., and Chou, S. H. (1999). Finite-volume lattice boltzmann schemes in two and three dimensions. *Physical Review E*, 60(3):3380–3388.

Xie, H., Wang, J., Xi, T., Liu, Y., Ai, F., and Wu, Q. (2002). Thermal conductivity enhancement of suspensions containing nanosized alumina particles. *Journal of Applied Physics*, 91(7):4568.

Xuan, Y. and Yao, Z. (2005). Lattice boltzmann model for nanofluids. *Heat and Mass Transfer/Waerme- und Stoffuebertragung*, 41(3):199–205.

Xuan, Y. M., Li, Q., and Hu, W. F. (2003). Aggregation structure and thermal conductivity of nanofluids. *Aiche Journal*, 49(4):1038–1043.

Xue, L., Keblinski, P., Phillpot, S. R., Choi, S. U. S., and Eastman, J. A. (2003). Two regimes of thermal resistance at a liquid-solid interface. *Journal of Chemical Physics*, 118(1):337–339.

Xue, L., Keblinski, P., Phillpot, S. R., Choi, S. U. S., and Eastman, J. A. (2004). Effect of liquid layering at the liquid-solid interface on thermal transport. *International Journal of Heat and Mass Transfer*, 47(19-20):4277–84.

Xue, Q.-Z. (2003). Model for effective thermal conductivity of nanofluids. *Physics Letters A*, 307(5-6):313–17.

Yamada, E. and Ota, T. (1980). Effective thermal conductivity of dispersed materials. *Waerme- und Stoffuebertragung*, 13(1-2):27–37.

Yu, C. J., Richter, A. G., Datta, A., Durbin, M. K., and Dutta, P. (1999). Observation of molecular layering in thin liquid films using x-ray reflectivity. *Physical Review Letters*, 82(11):2326–9.

Yu, W. and Choi, S. U. S. (2003). The role of interfacial layers in the enhanced thermal conductivity of nanofluids: A renovated maxwell model. *Journal of Nanoparticle Research*, 5(1-2):167–171.

Yu, W. and Choi, S. U. S. (2004). The role of interfacial layers in the enhanced thermal conductivity of nanofluids: A renovated hamilton-crosser model. *Journal of Nanoparticle Research*, 6(4):355–361.

Zarghami, A., Maghrebi, M. J., Ghasemi, J., and Ubertini, S. (2012). Lattice boltzmann finite volume formulation with improved stability. *Communications in Computational Physics*, 12(1):42–64.

Zarghami, A., Ubertini, S., and Succi, S. (2013). Finite-volume lattice boltzmann modeling of thermal transport in nanofluids. *Computers & Fluids*, 77:56–65.

Zhang, X., Gu, H., and Fujii, M. (2007). Effective thermal conductivity and thermal diffusivity of nanofluids containing spherical and cylindrical nanoparticles. *Experimental Thermal and Fluid Science*, 31(6):593–599.

Zhou, S.-Q., Ni, R., and Funfschilling, D. (2010). Effects of shear rate and temperature on viscosity of alumina polyalphaolefins nanofluids. *Journal of Applied Physics*, 107(5):054317–6.

Zhu, H.-T., Lin, Y.-S., and Yin, Y.-S. (2004). A novel one-step chemical method for preparation of copper nanofluids. *Journal of Colloid and Interface Science*, 277(1):100–103.

Appendix A
Physical Properties

Temperature-dependent water properties are shown in Figure A–1 and Figure A–2. These values were obtained from the National Institute of Standards and Technology (NIST) WebBook: `http://webbook.nist.gov/chemistry/fluid/` (Wagner and Pruss, 2002; Kestin et al., 1984; IAPWS, 1998, 1997). The physical properties for the solid particles shown in Table A–1 were obtained from the literature reviewed in chapter 2.

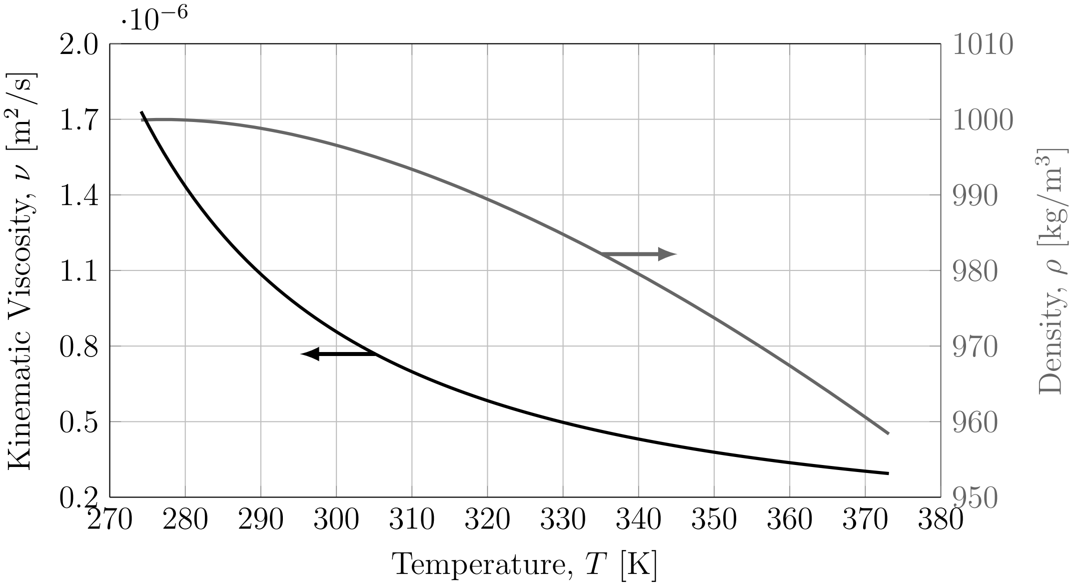

Figure A–1: Physical properties of water: viscosity and density vs. temperature.

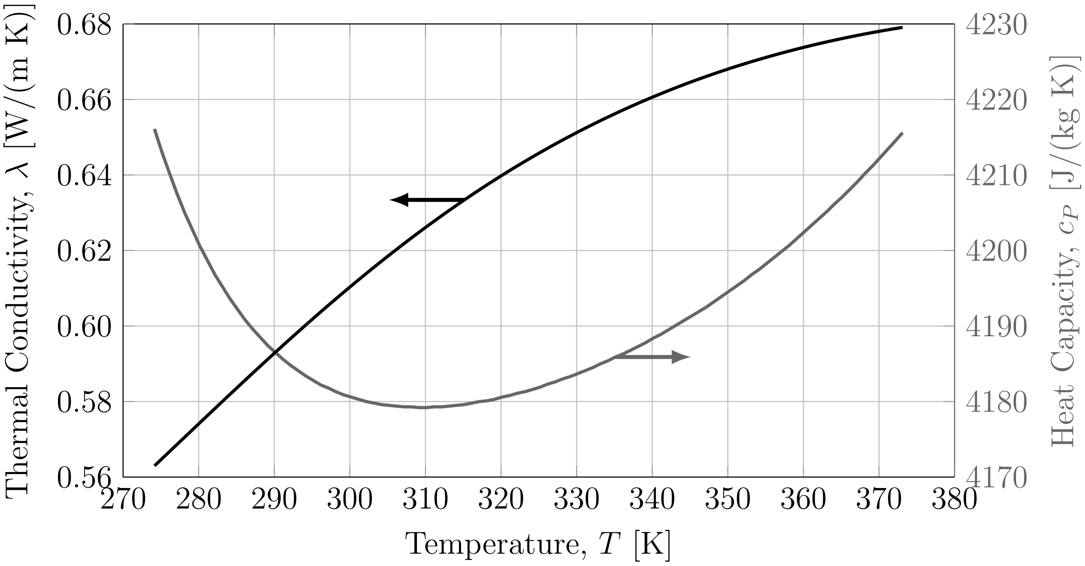

Figure A–2: Physical properties of water: thermal conductivity and heat capacity vs. temperature.

Table A–1: Physical properties for solid particles at 295 K.

Material	α [W/(m K)]	c_P [J/(kg K)]	ρ [kg/m^3]
Al_2O_3	40	775	4000
SiO_2	1.3	703	2648
Cu	400	385	8960
CuO	17	578	6315